Aerodynamic Benefits of Boundary Layer Ingestion for the D8 Double-Bubble Aircraft

by

Cécile J. Casses

B. Eng., Ecole Centrale Paris, 2013

Submitted to the Department of Aeronautics and Astronautics
in partial fulfillment of the requirements for the degree of

Master of Science in Aeronautics and Astronautics

at the

MASSACHUSETTS INSTITUTE OF TECHNOLOGY

September 2015

Author .... Signature redacted ....
Department of Aeronautics and Astronautics
August 19, 2015

Certified by....................... Signature redacted ......
Edward M. Greitzer
H. N. Slater Professor of Aeronautics and Astronautics
Thesis Supervisor

Certified by.......... Signature redacted ....
Alejandra Uranga
Research Engineer, Department of Aeronautics and Astronautics
Thesis Supervisor

Accepted by .... Signature redacted ....
Paulo C. Lozano
Associate Professor of Aeronautics and Astronautics
Chair, Graduate Program Committee

Aerodynamic Benefits of Boundary Layer Ingestion for the D8 Double-Bubble Aircraft

by

Cécile Casses

Submitted to the Department of Aeronautics and Astronautics
on August 19, 2015, in partial fulfillment of the
requirements for the degree of
Master of Science in Aeronautics and Astronautics

Abstract

This thesis describes experimental assessments of the aerodynamic boundary layer ingestion (BLI) benefit of the D8 advanced civil aircraft design. Two independent methods were applied for 1:11 scale (4.1 m wingspan) powered aircraft model experiments in the NASA Langley 14x22-foot Subsonic Wind Tunnel. The metric used as a surrogate for fuel consumption was the input mechanical flow power, and the benefit was quantified by back-to-back comparison of non-BLI (podded) and BLI (integrated) configurations.

The first method (indirect) was the estimate of mechanical flow power based on the measured electrical power to the propulsors, plus supporting experiments to characterize the efficiencies of the fans and the electric motors that drive them, at the MIT Gas Turbine Laboratory. The second method (direct) was the direct integration of flowfield measurements, from five-hole probe surveys at the inlet and exit of the propulsors, which provided flow angles, velocity components, and pressure coefficients. Data were taken at different wind tunnel speeds, and conditions to determine overall performance dependence on non-dimensional power and angle of attack. At the simulated cruise point, the first method gave a measured aerodynamic BLI benefit of 7.9%±1.5% at 70 mph tunnel velocity, and 8.5%±1.5% at 84 mph, and the second method gave a measured benefit of 8.1%±3.3% at 70 mph, and 12.2%±3.4% at 84 mph. For the aircraft models examined, the aerodynamic benefit was found to come primarily from a decrease in the propulsor jet velocity (increase in propulsive efficiency) and thus a decreased jet dissipation, with the contribution from decreased wake and airframe dissipation being roughly an order of magnitude smaller.

Thesis Supervisor: Edward M. Greitzer
Title: H. N. Slater Professor of Aeronautics and Astronautics

Thesis Supervisor: Alejandra Uranga
Title: Research Engineer, Department of Aeronautics and Astronautics

Acknowledgments

This research was supported by NASA's Fundamental Aeronautics program, the NASA Fixed Wing Project under Cooperative Agreement NNX11AB35A.

I would like to start by thanking my advisor, Edward Greitzer, who enabled me to have the MIT Energy Initiative Fellowship as a financial support during my first year at MIT. His infinite technical support and advice in the past two years helped me learn how to solve engineering problems in a rigorous manner. I want to recognize Neil Titchener for his guidance through this project, the ski trip, and the British spirit, Alejandra Uranga for her support and meticulous help with the thesis writing. Last but not least, Professor Drela for sharing his deep knowledge during his amazing courses. I appreciate the assistance of Robin Courchesne-Sato who made everything possible at the Gas Turbine Lab.

I acknowledge the help of all the members of the N+3 team for making all of that come true. A special thanks goes to Michael, and Nina who were always present to explain with patience everything they worked on on the project and to help me move forward. Not to forget Elise, Arthur Huang, David Hall, and Adam Grasch for their irreplaceable contributions. Thank you to those who helped during the Langley tests, to James Jensen and Shishir Pandya at NASA Ames for the CFD, and to Gregory Gatlin at NASA Langley Research Center.

And if you think MIT is not hard enough, it is forgetting Devon that comes to your office and asks you aerodynamics questions that you have no clue about. But, of course, he knows the answer! Thanks for keeping my mind busy, for your optimism, for your patience when I made you repeat the same sentence five times, and for your friendship. The daily tea time with Devon, Elise, Lucie, and Sebastien is above all the main reason for the completion of this thesis and created an atmosphere more joyful, optimistic, and social at the GTL.

These years would have never been the same without my friends, those who stayed in France and those I met in Boston, and the ORCers. Particularly, my roommates Ludo, Virgile, and Mapi with whom I shared meals, joys, sadness, and

more! Thanks to Claire-Marine and Pierre for all our life talks. To the Trapuchette and the 109 Otis for all the social events. Most importantly, I am sincerely grateful to Maximilien for his support through the last month of my master and for my career decision, and his love.

Lastly, all of that would have never been possible without the support, the love, and the trust in me of my family. I will never forget all the efforts that my parents, my brothers, my grandma, and my godfather put into this adventure. Not to mention, FREE, the French carrier, that enabled my little brother to call me from France everyday!

Contents

List of Figures

List of Tables

Nomenclature

Latin Letters

A_{f}	fan area
C_D	drag coefficient
C_{p_0}	stagnation pressure coefficient $(= (p_0 - p_{0\infty})/q_\infty)$
$C_{P_{\mathrm{E}}}$	electric power coefficient $(= P_{\mathrm{E}}/q_\infty V_\infty S_{\mathrm{ref}})$
$C_{P_{\mathrm{S}}}$	shaft power coefficient $(= P_{\mathrm{S}}/q_\infty V_\infty S_{\mathrm{ref}})$
$C_{P_{\mathrm{K}}}$	mechanical flow power coefficient $(= P_{\mathrm{K}}/q_\infty V_\infty S_{\mathrm{ref}})$
c_{tip}	rotor tip chord
C_{X}	net streamwise force coefficient $(= F_{\mathrm{X}}/q_\infty S_{\mathrm{ref}})$
D	drag force
D_{fan}	D8 propulsor fan diameter
f_{BLI}	percentage of fuselage boundary layer ingested by the propulsors
F_{N}	force
F_{X}	net streamwise force $(= D - T)$
i	indexing variable or current
k	motor calibration factor
k_{C}	calibration factor for the wind tunnel dynamic pressure
L	length
$\dot{m}$	mass flow
M	Mach number
$\hat{n}$	unit normal vector
N	number of repeated measurement

N_r	number of radial points in flow surveys
N_θ	number of circumferential points in flow surveys
N_{tot}	number of total points in flow surveys
p	static pressure
p_0	stagnation pressure
P	power
P_{E}	electrical power
P_{S}	shaft power
P_{K}	mechanical flow power
$\widetilde{P}_{\mathrm{K}}$	mechanical flow power integrated in the measurement plane
PSC	BLI benefit $(=(C_{P_{\mathrm{K,non\text{-}BLI}}} - C_{P_{\mathrm{K,BLI}}})/C_{P_{\mathrm{K,non\text{-}BLI}}})$
q	dynamic pressure $(= 0.5\rho V^2)$
q_{C}	kiel probe dynamic pressure in the MIT GTL wind tunnel
Q	torque or volumetric flow rate
r	radial location
Re	Reynolds number
s	standard deviation
S	surface integration variable
S_{ref}	D8 model reference area
t	t-distribution correction factor
T	thrust force
U_{tip}	fan tip speed
v	voltage
$\mathbf{V}$	velocity vector
V	speed
V_x, V_y, V_z	Cartesian velocity components
$\widetilde{V}_0$	reference velocity for the MIT GTL experiments
V_{LC}	load cell voltage value
W	weight
Y, Z	cartesian coordinates of survey points; y is spanwise and z is vertical

Greek Letters

α	D8 model angle of attack or pitch flow angle for flow surveys
β	D8 model side slip angle or yaw flow angle for flow surveys
η	efficiency
γ	heat capacity ratio
μ	air viscosity
Ω	motor wheel speed
π	stagnation pressure ratio
ϕ	flow coefficient
Φ	dissipation quantity
ψ	stagnation pressure rise coefficient
ρ	air density
τ	stagnation temperature ratio
σ	measurement uncertainty

Superscripts

$(\ )'$	non-BLI configuration quantity

Subscripts

$(\ )_{\mathrm{BLI}}$	BLI configuration (or integrated)
$(\ )_{\mathrm{f}}$	fan quantity
$(\ )_{\mathrm{in}}$	propulsor inlet quantity
$(\ )_{\mathrm{jet}}$	propulsor jet quantity
$(\ )_{\mathrm{LC}}$	load cell quantity
$(\ )_{\mathrm{left}}$	left propulsor quantity
$(\ )_{\mathrm{m}}$	electric motor quantity
$(\ )_{\mathrm{non-BLI}}$	non-BLI configuration (or podded)
$(\ )_{\mathrm{o}}$	overall quantity
$(\ )_{\mathrm{out}}$	propulsor exit quantity

$(\ )_{\mathrm{ref}}$	reference quantity
$(\ )_0$	quantity at station 0 in the MIT GTL wind tunnel
$(\ )_{\mathrm{right}}$	right propulsor quantity
$(\ )_{\mathrm{surf}}$	fuselage surface quantity
$(\ )_{\mathrm{vortex}}$	vortex quantity
$(\ )_{\mathrm{wake}}$	fuselage wake quantity
$(\ )_{\mathrm{W}}$	weight quantity
$(\ )_{\infty}$	freestream (wind tunnel) quantity

Other Symbols

$\Delta(\ )$	difference quantity
$(\bar{\ })$	mass-averaged quantity

Abbreviations

APC	advanced precision composites
BLI	boundary layer ingestion
CFD	computational fluid dynamics
CV	control volume
EMF	electromotive force
ESC	electronic speed controller
FHP	five-hole probe
GTL	Gas Turbine Laboratory
LTO	landing, take off
MIT	Massachusetts Institute of Technology
NASA	National Aeronautics and Space Administration
NOx	nitrogen oxyde
N+3	2025-2035 time frame
PS	Pitot-static
TASOPT	transport aircraft system optimization code

Chapter 1

Introduction

In 2008, NASA put forward a solicitation for the development of advanced concepts and enabling technologies to address environmental challenges and performance improvements for commercial transport aircraft entering in service in the 2025-2035 timeframe. Since then, in two separate phases, a team of MIT, Aurora Flight Sciences, and Pratt and Whitney, has been carrying out research to create and assess the conceptual design of the D8 aircraft that meets the NASA requirements of fuel burn reduction, noise reduction, and landing and take-off (LTO) nitrogen oxide (NOx) emissions. Although the goals have changed since 2008, as shown in Table 1.1[1], they are still aggressive enough that meeting them calls for a clean-sheet design.

A product of Phase I (September 2008 to March 2010) was the conceptual design of the D8 subsonic transport to meet the NASA targets [2]. A key technology for aircraft fuel burn reduction was found to be Boundary Layer Ingestion (BLI). It is critical to assess BLI benefit because the technology has not been implemented on civil aircraft.

Table 1.1: NASA goals for N+3 generation of aircraft

	Fuel burn	Noise	LTO NOx emissions
Goals (2008 [2])	-70%	-71 EPNdB below stage 4	-80% below CAEP6
Goals (2013 [3])	-60%	-52 EPNdB below stage 4	-80% below CAEP6

---

[1] EPNdB measures the effective perceived noise in decibels, and CAEP refers to the Committee on Aviation Environmental Protection.

A major focus of Phase II, from November 2010 to May 2015, therefore was assessment of the BLI benefit for the D8. For this purpose, experiments in the NASA Langley 14x22-foot Subsonic Wind Tunnel [4], using a 1:11 scale powered D8 aircraft model, were designed and carried out. Numerical simulations of the model in the wind tunnel have also been conducted. This thesis describes the wind tunnel experiments and conceptual simulations to evaluate the BLI benefit.

1.1 The D8 Aircraft Concept

A three-view of the D8 aircraft concept as designed by Drela [2] is shown in Figure 1-1. Often referred to as the 'double-bubble' in reference to the fuselage cross-section, the aircraft is designed to operate on the same missions as a B737-800 or an A320 (180 passengers, 3000 NM range transport). This twin-engine is predicted to require 66% less fuel burn than the 737-800 baseline if constructed with 2025-2035 level technology, or 33% if constructed with currently available technology [5].

The aircraft design was found by simultaneous optimizations of the airframe, the engines, and the operations for a given mission, to achieve minimum fuel burn[2]. The main features of the aircraft are: two propulsors flush-mounted on the top aft fuselage under a pi-tail permitting 40% of the fuselage boundary layer to be ingested by the propulsors; higher lift generated by the fuselage (18% vs 13% for a B737-800 [6]) allowing the wings to shrink; lift generated by the nose to decrease the size of the horizontal tail; aircraft cruise Mach number of 0.72 to lower the wing sweep; pi-tail to lighten the horizontal tail compared to T-tail and to provide noise shielding for the propulsors; and double-bubble shape for two aisles to reduce passenger loading and unloading times.

---

[2] The multi-disciplinary tool used was TASOPT 2.0, TASOPT stands for Transport Aircraft System OPTimization [2].

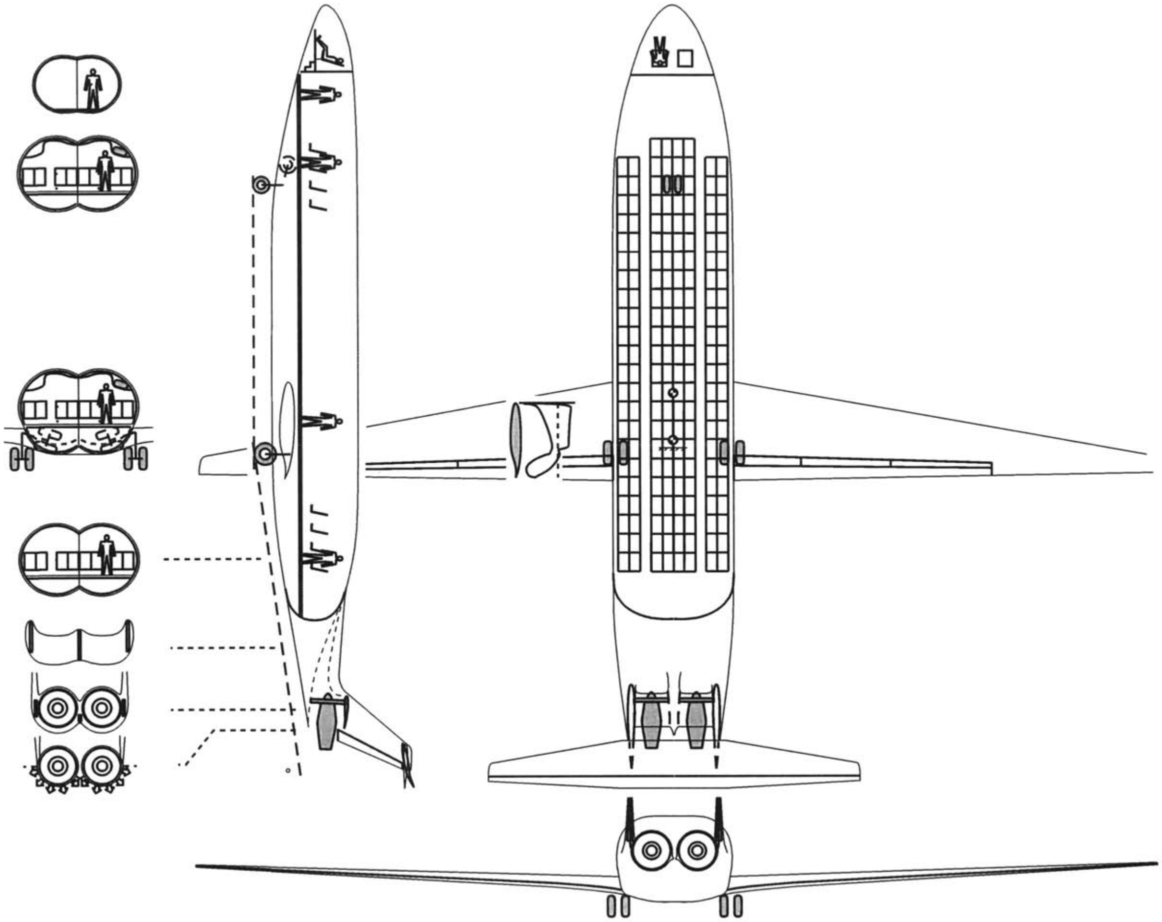

Figure 1-1: Cross-section, side, top, and back views of the D8 aircraft from [5].

1.2 Boundary Layer Ingestion

Boundary Layer Ingestion (BLI) occurs when the propulsors ingest some part of the flow that is decelerated due to the friction with a surface. For the D8, the propulsors ingest roughly 40% of the fuselage boundary layer. Previous studies have estimated that BLI can reduce power requirement between 5 and 10% [7, 8] depending on how much boundary layer is ingested and the boundary layer shape parameters. With BLI, the exhaust jet and the fuselage wake are co-located so there is a reduced kinetic energy defect in the wake, and an increase in propulsive efficiency for the jet, and thus a reduced power consumption. It is difficult, however, to separate the forces due to the propulsor and those due to the airframe, as implied by Figure 1-2. The left-hand side shows a conventional (non-BLI) propulsion system and the right-hand side illustrates that the jet is embedded in the wake so thrust and drag generating flows are intermingled.

To provide a more appropriate framework for analyzing integrated systems, Drela introduced a power balance method [9] rather than working in terms of forces. The mechanical flow power transmitted by the propulsors to the flow results in several different dissipation sources: jet, wake, surface, boundary layers, and trailing vortex. These sources are sketched in Figure 1-3 in which the quantities associated with the non-BLI configuration are primed, and those for the BLI case are unprimed. The jet and wake dissipations are lower for the BLI configuration, while the surface dissipation and vortex dissipations are nearly equal (the estimated difference is less than 1%) for BLI and non-BLI configurations.

A mechanical flow power coefficient, $C_{\mathrm{P_K}}$, can be defined by the ratio of me-

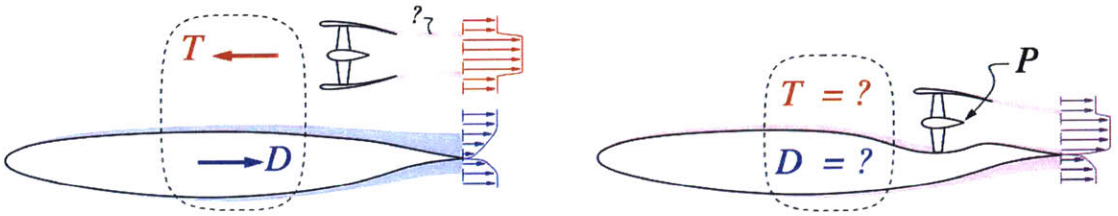

Figure 1-2: Difference of force definitions between non-BLI propulsors (left) and BLI propulsors (right)

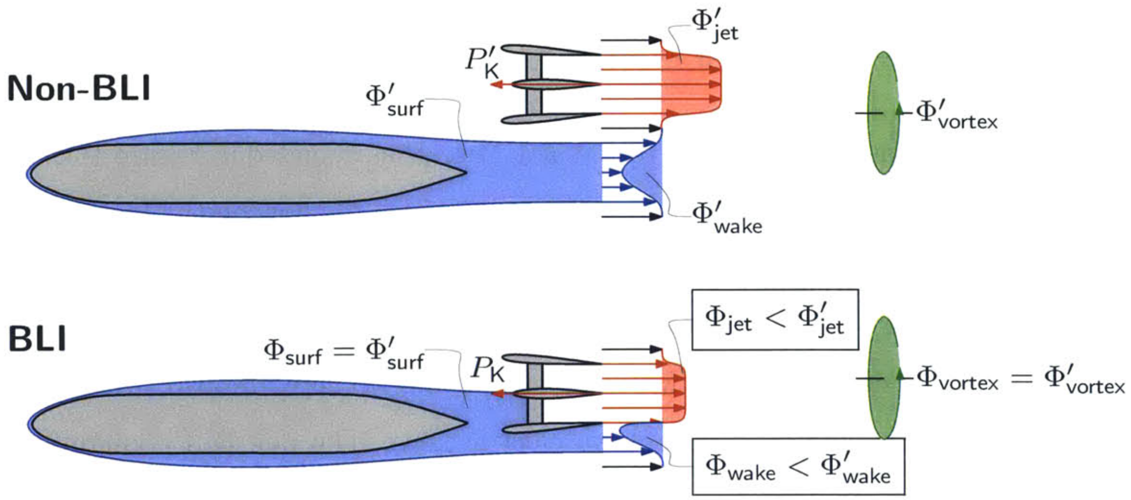

Figure 1-3: Power and dissipation sources for the non-BLI and BLI configurations. Credit: Hall.

chanical flow power, P_{K}, to a reference power, $0.5\rho_\infty V_\infty^3 S_{\text{ref}}$ by

$$C_{P_{\mathrm{K}}} = \frac{P_{\mathrm{K}}}{0.5\rho_\infty V_\infty^3 S_{\text{ref}}}. \tag{1.1}$$

The subscript ∞ represents freestream quantities and the reference area, S_{ref}, corresponds to the area of the exposed wings plus the virtual wing extending through the fuselage. The density of the freestream flow is ρ_∞ and V_∞ is the incoming flow velocity. The aerodynamic BLI benefit[3] is quantified by comparison of non-BLI and BLI configurations, and defined as a power saving coefficient, PSC, as

$$BLI\ Benefit = \frac{C_{P_{\mathrm{K,non\text{-}BLI}}} - C_{P_{\mathrm{K,BLI}}}}{C_{P_{\mathrm{K,non\text{-}BLI}}}}. \tag{1.2}$$

This definition is consistent with Smith's power saving coefficient, *PSC* [7].

Assessing the BLI benefit is possible using data obtained from wind tunnel experiments with a powered scale model, as is described in this thesis and previous MIT N+3 publications ([10], [5], [1], [11], [12]).

---

[3] There are others systems benefits for the BLI configuration, which are described in [6]. This thesis examines the aerodynamic benefit only.

1.3 NASA Langley Experiments

Three configurations of the D8 were tested at 1:11 scale as depicted in Figure 1-4. Figure 1-4(a) shows the *unpowered configuration* with which the flow on the fuselage can be assessed. The horizontal tail and the front fuselage, which are drawn in black lines, are common to the three configurations to facilitate back-to-back comparison. The tail, which can be changed, is drawn with dashed lines. There are also two *powered configurations* with propulsors that have electric fans. The non-BLI configuration (also referred to as 'podded') is shown in Figure 1-4(b) and the BLI configuration (referred to as 'integrated') is shown in Figure 1-4(c).

Each propulsor consists of a nacelle, an Aero-naut TF8000 fan stage (rotor and stator), an electric motor driving the fan, and a nozzle plug. Figure 1-5(a) is a drawing of the BLI propulsor and Figure 1-5(b) a drawing of the non-BLI propulsor. The propulsors were designed to be inserted in either the BLI or non-BLI configurations, again to allow back-to-back comparisons in evaluation of BLI benefit. Table 1.2 summarizes the angles at which the propulsors are titled and pitched.

Three nozzle plugs, shown in Figure 1-6, were manufactured to vary the mass flow through the propulsors. The plugs could be changed on the model without removing any other part. Table 1.3 summarizes the different plugs and the ratio of the nozzle areas to the fan frontal area.

A first-time back-to-back comparison of BLI and non-BLI configurations to obtain an evaluation of BLI was carried out in a series of experiments in the NASA Langley 14x22-foot Subsonic Wind Tunnel. These experiments are referred to as the Langley tests.

There were two series of wind tunnel entries. The first entry, August and

Table 1.2: Propulsor design yaw and pitch angles in the airframe reference frame. Credit: Lieu.

Configuration	Design yaw angle	design pitch angle
BLI	3°	1.5°
Non-BLI	0°	2°

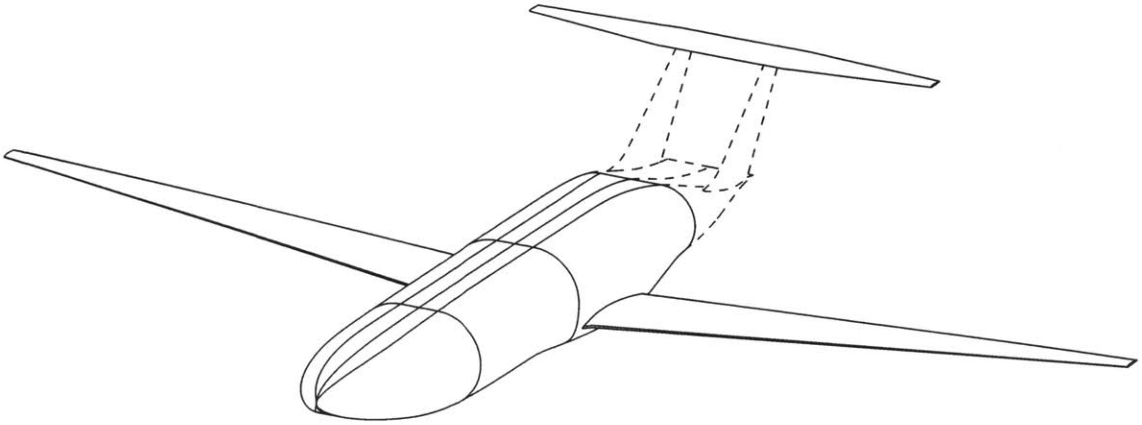

(a) Unpowered configuration: common body in dark and interchangeable tail in dashed lines

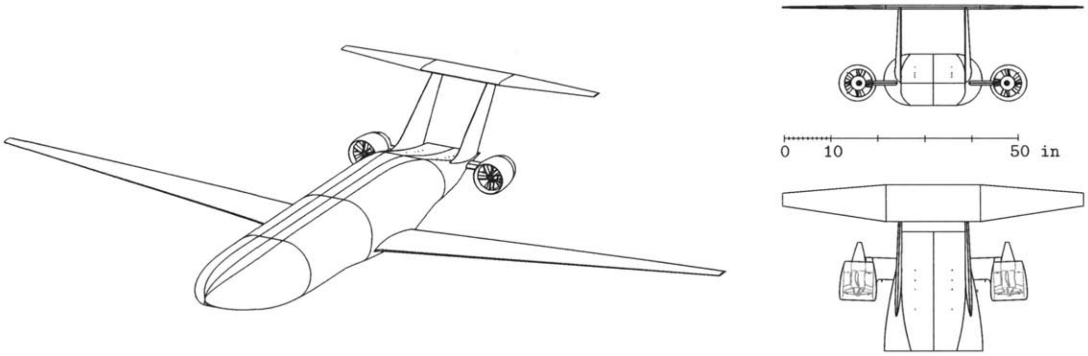

(b) non-BLI configuration

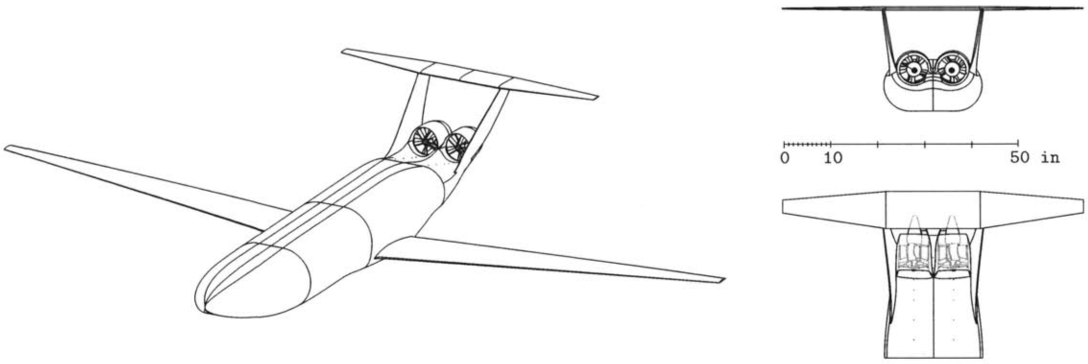

(c) BLI configuration

Figure 1-4: Model configurations of the D8 aircraft tested at NASA Langley. Credit: Lieu.

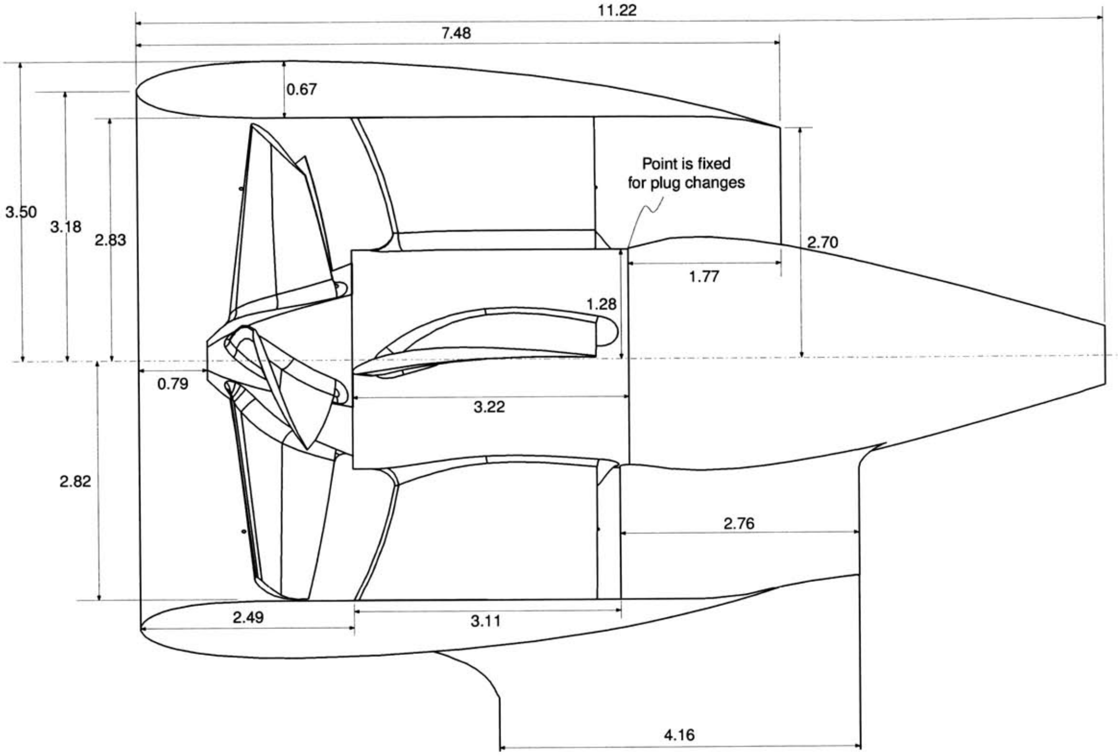

(a) non-BLI propulsor

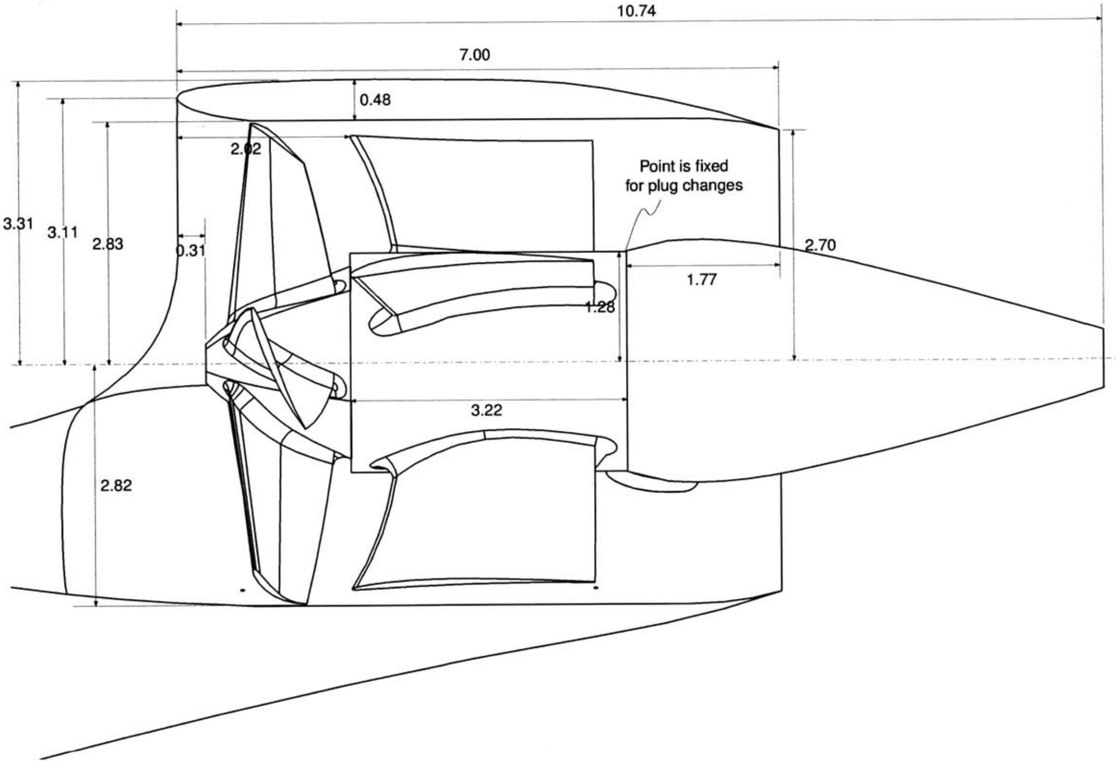

(b) BLI propulsor

Figure 1-5: Dimensions of the D8 propulsor for a) the non-BLI configuration and b) the BLI configuration. Units in inches

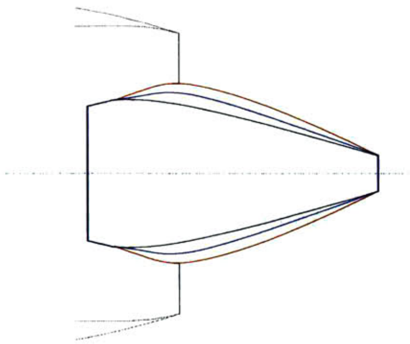

Figure 1-6: Differences between plug 1 (small), 3 (medium), and 5 (big)

Table 1.3: Plug characteristics where fan area, A_f, is 0.0159 m^2

Plug	Color in Figure $1-6$	Ratio of nozzle area to fan area
1	black	0.535
3	blue	0.604
5	red	0.679

September 2013, included *power sweeps* where wind tunnel speed, angle of attack, and sideslip angle were fixed and motor speed was varied to obtain data for different net streamwise force coefficients (C_X). The range of parameters was: 2° – 8° for angle of attack, ± 15° for sideslip angle, 42 – 70 mph for wind tunnel speed, and 0 – 13500 RPM for wheel speed. *Pressure rake surveys*, i.e. pressure measurements with a rake at the inlet and exit of the propulsors, were also done. Integration of those pressure measurements provided an estimate of mechanical flow power and BLI benefit. Evaluation of the BLI benefit from the rake surveys was carried out by Lieu [11].

A second tunnel entry took place in August and September 2014. The maximum wind tunnel speed was increased from 70 mph to 84 mph to reduce the experimental uncertainty. The experimental repeatability was also measured, for the same reason. Power sweeps, five-hole probe (FHP) surveys, and rake surveys were performed. The FHP surveys provide information on the flow ingested by the propulsors, as will be seen, to allow evaluation of the mechanical flow power.

A main interest was the simulated cruise condition, as cruise is where most fuel is burnt. This condition is characterized by zero net streamwise force ($C_X = 0$) or, for a conventional configuration, when drag and thrust are balanced. Off-design conditions were also considered: start-of-climb, top-of-climb, descent, cross-wind, and propulsor-out. The model had turbulence trips so the flow on the wings and the fuselage of the aircraft was turbulent, as would be the full-scale aircraft flow. The ratio of jet to freestream velocities at the design point was the same as the ratio for the full-scale aircraft based on information from TASOPT. Figure 1-7 shows the BLI configuration in the wind tunnel section.

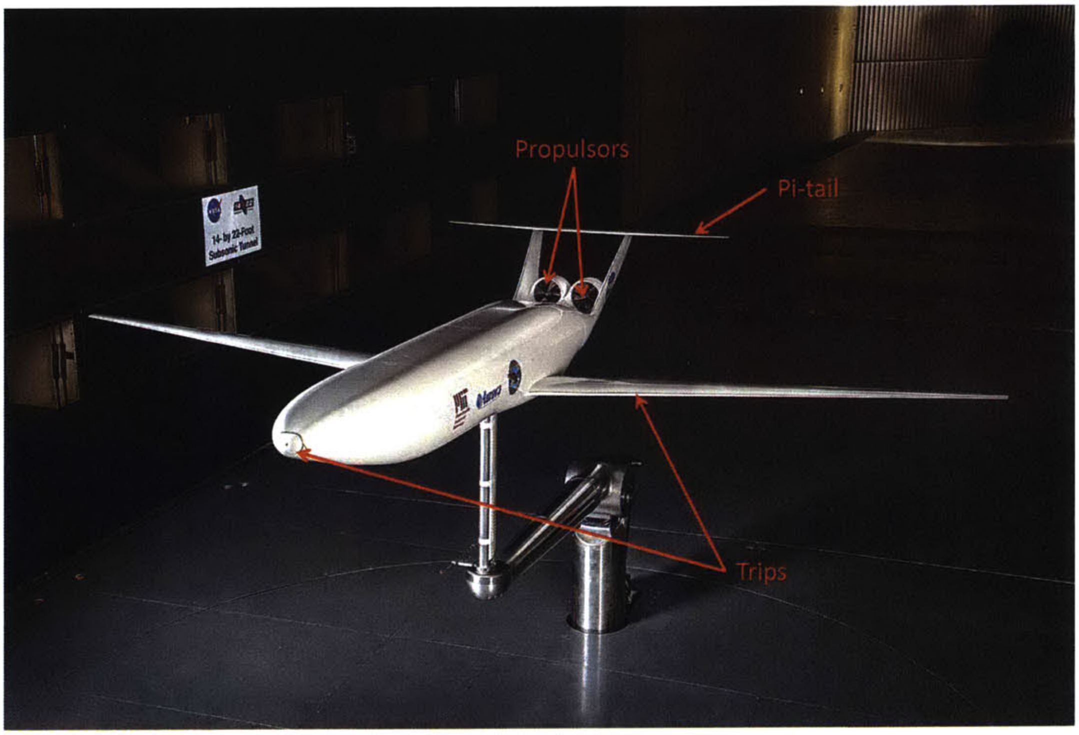

Figure 1-7: D8 in the NASA Langley Wind Tunnel. in September 2014.
Credit: NASA/George Homich.

1.4 Thesis Goals, Contributions, and Outline

In this thesis, the experimental evaluation of the D8 BLI benefit via two methods which are compared with each other and with computations (CFD) is described. The two methods are:

1. Indirect Measurements of BLI benefit:

   The only power measurement directly accessible at Langley was electrical power to the propulsor motors, P_{E}, which needed to be converted into mechanical flow power, P_{K}, the metric of interest. To enable the conversion, experiments were conducted at the MIT GTL 1x1 foot wind tunnel to characterize the electric motor efficiency, η_{m}, defined as the ratio of shaft power, P_{S}, to electric power, P_{E}, and to characterize the propulsor and fan efficiency, η_{f}, defined as the ratio of mechanical flow power, P_{K}, to shaft power, P_{S} [1]. The mechanical flow power and the electrical power are related by

   $$P_{\mathrm{K}} = \eta_{\mathrm{f}} \eta_{\mathrm{m}} P_{\mathrm{E}}. \tag{1.3}$$

2. Direct Measurement of BLI benefit:

   The mechanical flow power is by definition [9] the volume flux of stagnation pressure, i.e. for incompressible flow:

   $$P_{\mathrm{K}} = \oint\!\!\oint (p_{0\infty} - p_0) \mathbf{V} \cdot \hat{n} dS. \tag{1.4}$$

   Stagnation and static pressure fields were obtained from FHP surveys of the inlet and exit of the propulsor. The mechanical flow power, and hence the aerodynamic BLI benefit, was found from integrating these measurements at each plane.

A complimentary effort, led by Pandya at NASA Ames Research Center, focused on numerically simulating the wind tunnel experiments. Chimera Grid Tools was used for the mesh and Overflow 2.2 for the solver. The simulations were run at 70 mph with plug 1 for different net streamwise forces. The CFD results provide a third method of assessing the BLI benefit.

The thesis is organized as follows. Chapter 2 describes the motor calibration experiments. The data obtained from those experiments are used in Chapter 3 to evaluate the BLI benefit via the indirect method. The FHP surveys are described in Chapter 4 including characterization of the inlet flow at different conditions. Integration of these pressure measurements and evaluation of the BLI benefit using the direct method are presented in Chapter 5. Chapter 6 discusses the comparison between BLI benefit measurements, and computational results, as well as the advantages associated with each method. Chapter 7 summarizes the results and the findings, and presents suggestions for future work.

Chapter 2

Motor Calibration Experiments

Evaluation of the BLI benefit implies determination of the mechanical power added to the stream by the propulsors, P_K, in the BLI and non-BLI configuration. The mechanical flow power was evaluated in two different ways as mentioned in Section 1.4. The goal of the first supporting experiments is to find the motor efficiency for the data obtained during the Langley tests, most importantly at the simulated cruise conditions (zero net streamwise force on the aircraft, $C_X = 0$) but also at off-design conditions ($C_X \neq 0$). The supporting experiments for the indirect method are described first.

2.1 Experimental Methodology

2.1.1 Setup

The fans were driven by LMT 3040-27 motors[1]. The motor efficiency, defined as the ratio of shaft power to electrical power, is

$$\eta_m = \frac{P_S}{P_E} = \frac{Q\Omega}{iv}, \tag{2.1}$$

in which shaft power, P_S, is the product of torque, Q, and motor wheel speed, Ω, and electrical power, P_E, is the product of current, i, and voltage, v, across the motor. To

---

[1] Windings: 27, HiAmp, maximum mechanical RPM: 50000 RPM.

evaluate the efficiency, the motor torque, the motor speed, and the electrical power are needed.

The motor speed and power are inputs to the experiments and are measured. Torque is measured using the motor calibration rig shown in Figure 2-1. The rig was constructed by Grasch [13] but has had several improvements. The motor was positioned using clamps on a fixed solid mount composed of half-tube aluminum fixed to an aluminum base plate to reduce vibrations. An aluminum arm, screwed to the tube on one end, presses against the load cell on other end. The arm length is 200 mm so the load at the free end does not exceed 10 Newtons. The load cell is fixed on a support mounted on the base plate, with height such that the arm is horizontal. A 10 Newton single axis OMEGA LCMKD load cell was used because this has an appropriately small range of force at reasonable cost. The power to the motor is supplied by silicon wires. Efforts were made to prevent wire motion or deformation during testing to not disturb the torque measurement, and a metal shield was installed in front of the wires. A propeller is attached to the motor shaft using a collet type propeller adaptor (Grasch [13]). The system collet-propeller was mounted so no torque is exerted [14]. Three different propellers are used to span the range of forces representative of the loads exerted during the Langley tests: 10x07, 10x08, and 10x09 APC[2] propellers. The propellers are defined with two numbers; the first is the diameter of the propeller in inches and the second is the pitch in inches per revolution. The experimental setup allows measurements of the force exerted on the load cell by the arm attached to the motor casing when the motor runs. From the known moment arm, the reaction torque from the motor on the motor casing, as well as the torque provided to the shaft, can be obtained.

2.1.2 Data Acquisition

The motor speed is acquired with a back-EMF signal from the motor and controlled by a future-I-40.100 electronic speed controller (ESC) from Schulze Elektronik. The

---

[2] APC stands for Advanced Precision Composites.

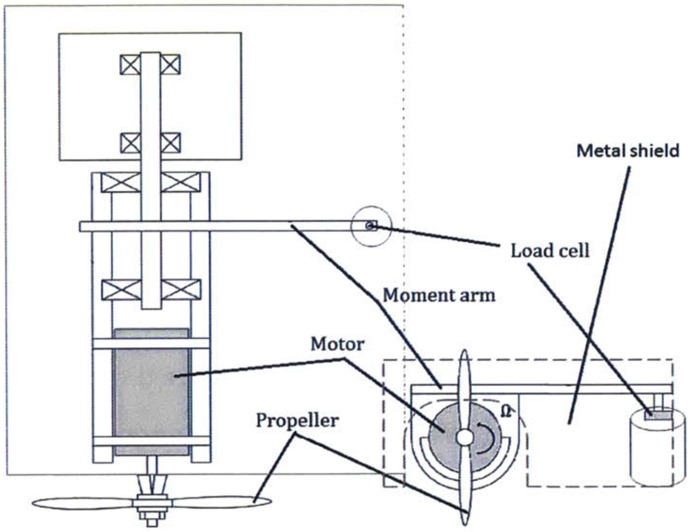

(a) Top and front view

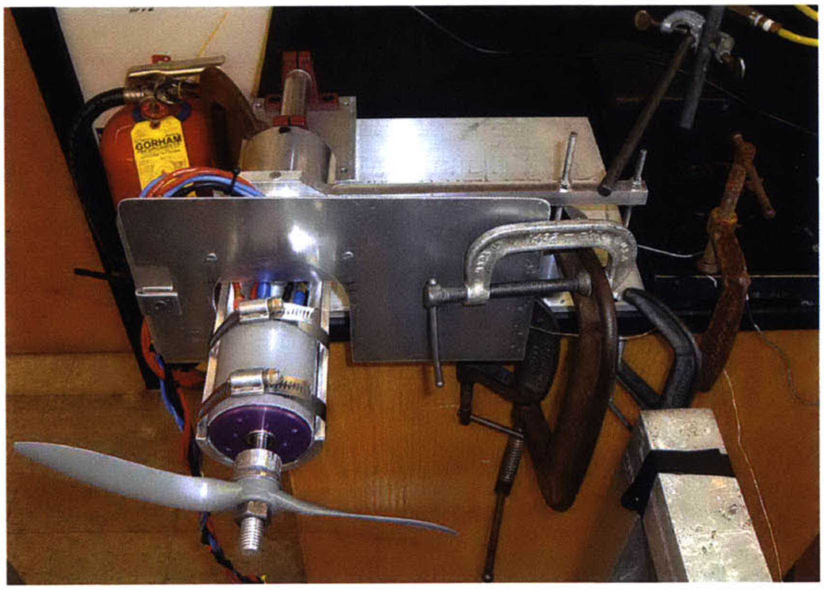

(b) 3D view

Figure 2-1: (a) Top and front view, and (b) 3D view of the dynamometer rig to measure torque current and voltage are obtained from the power supply[3].

An electronic box, powered by the power supply, contains the ESC and outputs voltage and motor speed signals. Estimation of the motor winding temperature is enabled through a thermocouple[4] placed on the skin of the motor. Voltage, current, RPM, temperature, and load cell voltage signals are linked to a National Instruments DAQ-9188 box and processed with Labview.

The data in this report were acquired with electronic box 1 (one of the two used during the Langley tests), power supply 1 and motor 6 unless otherwise specified. Motors 6 (left propulsor) and 7 (right propulsor) were used during Entry 1. To make sure there were no issues during Entry 2, two new motors were used: motors 16 (left propulsor) and 13 (right propulsor). Another set was used and is mentioned in Chapter 3: motors 9 (left propulsor) and 15 (right propulsor).

2.1.3 Data Collection

The load cell was calibrated by hanging different weights (200 g and 500 g) at different positions along the arm (100 mm and 50 mm from the load cell). At each point the voltage measured by the load cell is time-averaged over one and one half minutes. Figure 2-2(a) shows the measured calibration factor, k, against force, F_{N}: the subscript N stands for Newton. Red crosses correspond to the calibration factors obtained using the different weights at different locations and the blue line represents the mean of all the calibration factors. The dashed lines indicate variation of 1%. Figure 2-2(b) gives weight force against measured load cell voltage values, V_{LC} where the subscript LC denotes load cell value. The slope of the blue line is the mean calibration factor computed from data of Figure 2-2(a).

There is hysteresis in the load cell in that imposing a low loading (5250 RPM) after imposing a high loading (14000 RPM) gives a load cell value that differs from

---

[3] 2kW DCS 50-40 M16 power supply from Sorensen provides DC current at constant voltage by converting 240V 3-phase into 53V for the electronic box.

[4] OMEGA SA1 self-adhesive thermocouples.

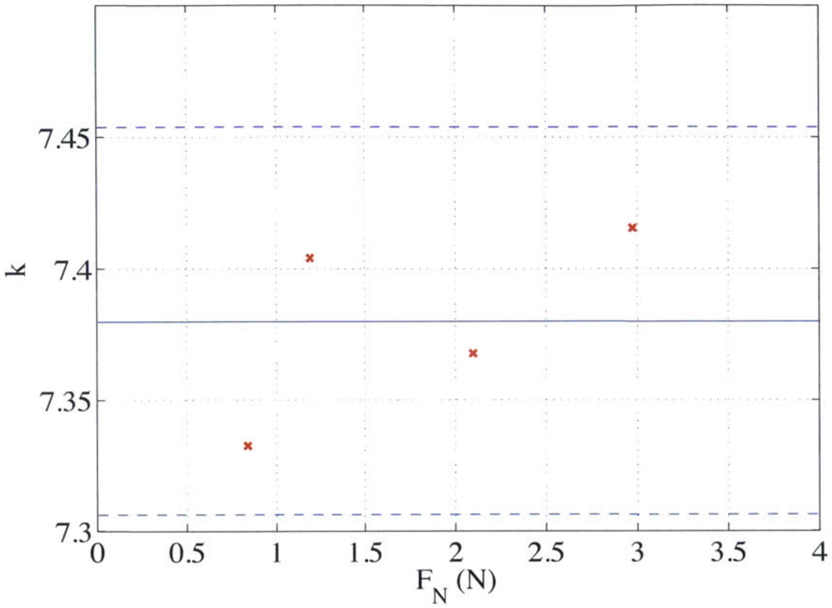

(a) k

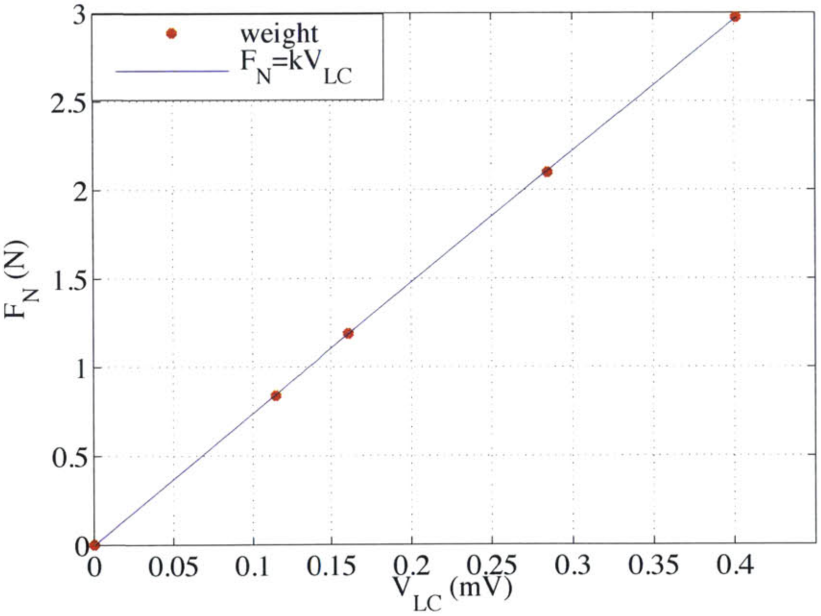

(b) F_N

Figure 2-2: Calibration curves: a) Calibration factor, k, against force in Newtons; b) Applied force in Newtons against measured load cell voltage the previous one. The difference is 3% at 10600 RPM. Consequently, load cell measurements were only recorded under conditions with the load (e.g. motor speed) increasing from zero[5].

A drift also occurs when going back to zero after loading. Imposing a high load (running at 14000 RPM) prior to running the experiments reduced the drift to less than 1% between the first zero of the run and the last one. The drift has been accounted for by assuming linear drift with time and subtracting it from the load cell values.

2.2 Motor Experiments Results

Figure 2-3 shows curves of torque and electrical power versus motor speed for the three propellers. Each propeller was run four times. The crosses represent the points for the four different runs, and the line is a cubic spline curve-fit through the average of these points at each motor speed. Blue dotted line, red dashed line and black solid line correspond to 10x07, 10x08, and 10x09 propellers, respectively. The power and torque increase cubically with speed for each propeller and increase with loading (higher propeller number) for the same motor speed.

Figure 2-4 shows the operating points from the Langley tests at 70 mph superimposed on the spline data interpolation. The operating points correspond to different angles of attack, α, wheel speed (RPM), and nozzle exit areas for the BLI configuration in the upper Figure 2-4(a), and the non-BLI configuration in the lower Figure 2-4(b) [5]. The crosses represent data for the left motor and the circles for the right motor. Cyan data represent off-design conditions, i.e. angle of attack between 4° and 8°. Magenta data represent both cruise and off-design power settings at 2°. Almost all the points lie within the calibration lines as desired: the motor efficiency at those points is obtained by interpolation between the calibration curves. Only a small number of off-design conditions require extrapolation outside the region spanned by

---

[5] The hysteresis of the load cell given in the manufacturer's specification sheet was accounted for in the uncertainty analysis (see Section 2.4.2).

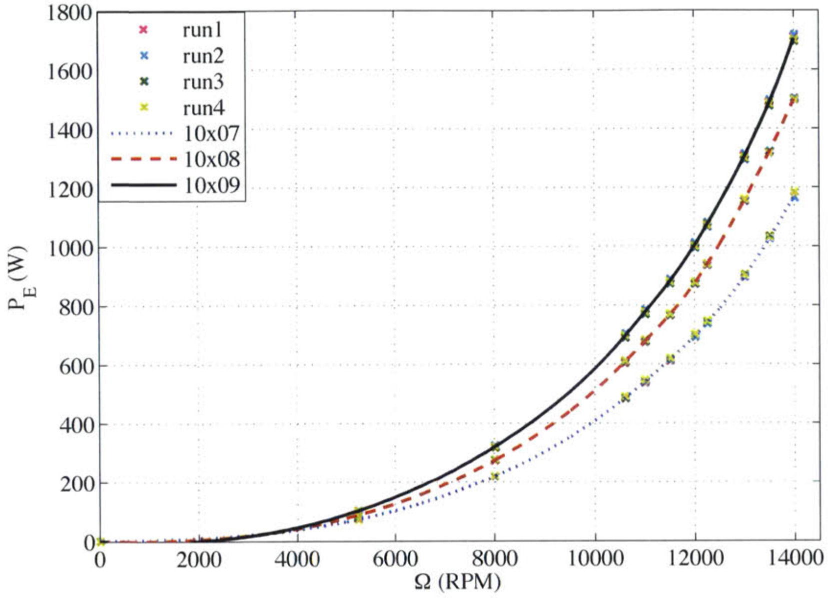

(a) $C_{P_{\mathrm{E}}}$

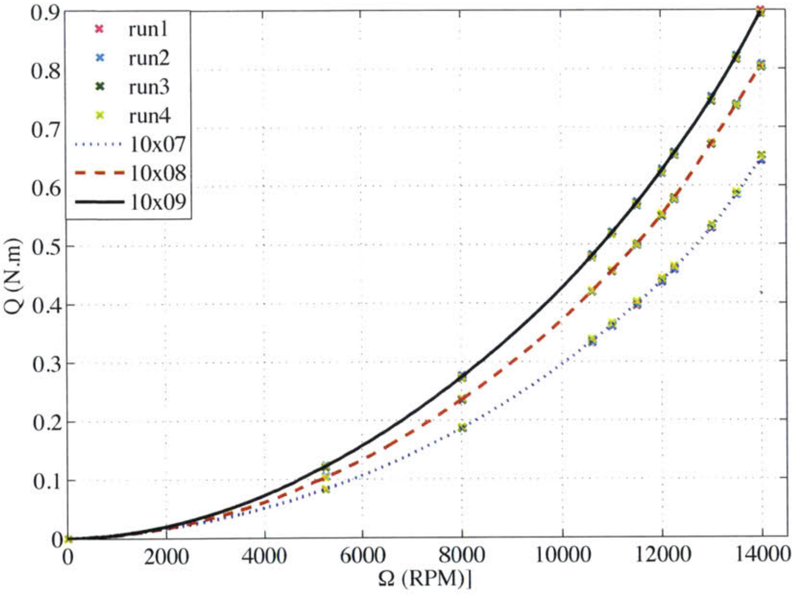

(b) Q

Figure 2-3: a) Electrical power and b) torque versus motor speed for the three propellers

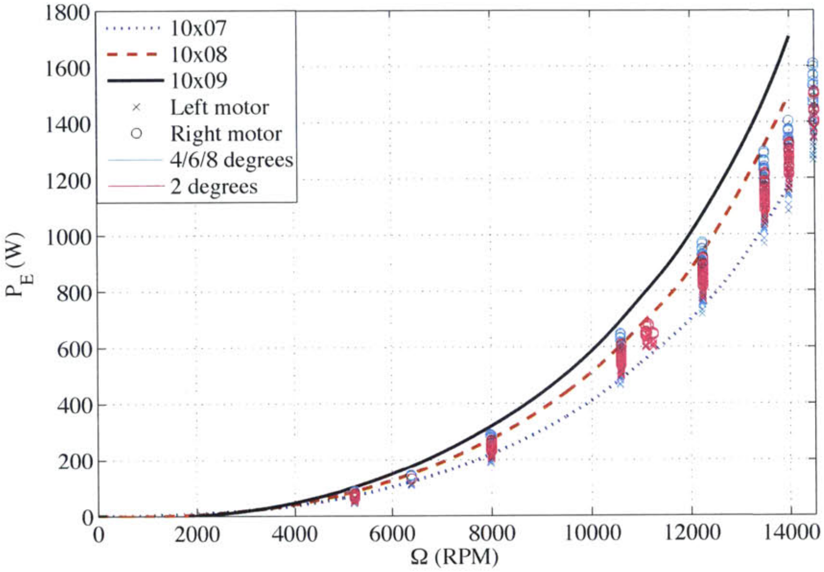

(a) BLI operating points

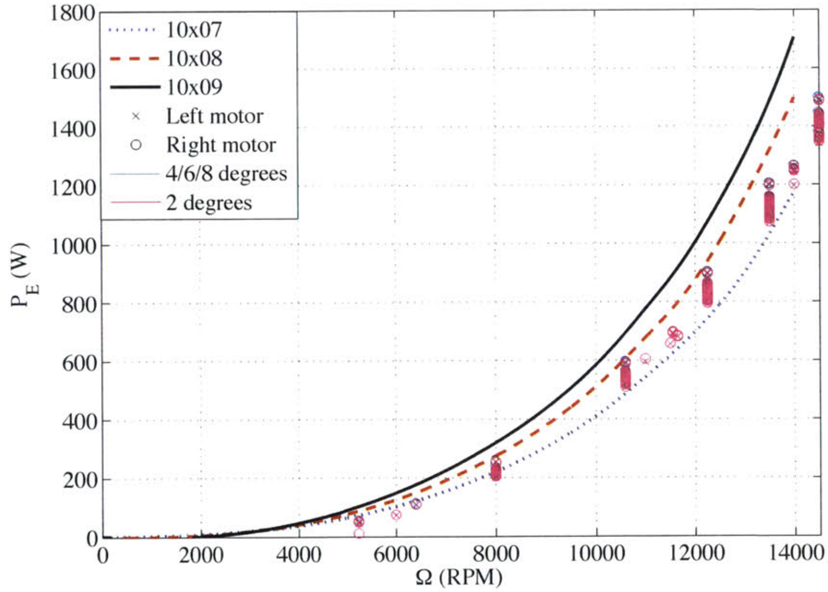

(b) non-BLI operating points

Figure 2-4: Superimposition of propeller operating points from calibration measurements and propulsor operating points from Langley at 70 mph a) for BLI configuration and b) for non-BLI configuration the calibration.

For the BLI configuration, at any conditions, the right propulsor draws more power than the left one to maintain the same wheel speed [5]. For the non-BLI configuration, both motors draw the same power. As example, for the BLI configuration, at $\alpha = 2°, C_X = 0, \frac{U_{tip}}{V_\infty} \approx 2.7$ (84 mph), the right propulsor requires approximately 6% more electrical power than the left propulsor. The difference is due to crossflow upstream of the fan face. Both fans rotate clockwise (from the pilot's view). The geometry of the aircraft, however, is such that the velocity has a symmetric theta component (of opposite sign on the two sides) i.e. the fan rotation and theta component of the velocity are opposite on the right side, giving larger incidence and requiring more power to the right propulsor than the left [5].

Figure 2-5 gives a contour map of motor efficiency (for motor 6). The non-BLI and BLI points at simulated cruise conditions are represented by a black diamond for the left non-BLI configuration, and by the green diamond for the left BLI propulsor. The efficiency values are indicated in increments of 1% change by the different colors in the figure. The motor efficiency data for all the motors used at Langley are given in Chapter 3.

Efficiencies at simulated cruise conditions for motors 6 (left propulsor) and 7 (right propulsor) are given in Table 2.1 as an example. The efficiency difference, at $C_X = 0$, between the non-BLI and the BLI configurations (taking an average value for the left and right motor efficiencies) is 0.8% of fan efficiency at a 95% confidence interval.

Table 2.1: Motor efficiencies at simulated cruise condition for motors 6 and 7 using electronic box 1, and power supply 1

Configuration	Ω (RPM)	P_E (W)	η_m (%)
Non-BLI (left propulsor)	11600	690	78.2
Non-BLI (right propulsor)	11600	690	78.3
BLI (left propulsor)	11200	630	77.7
BLI (right propulsor)	11200	680	77.6

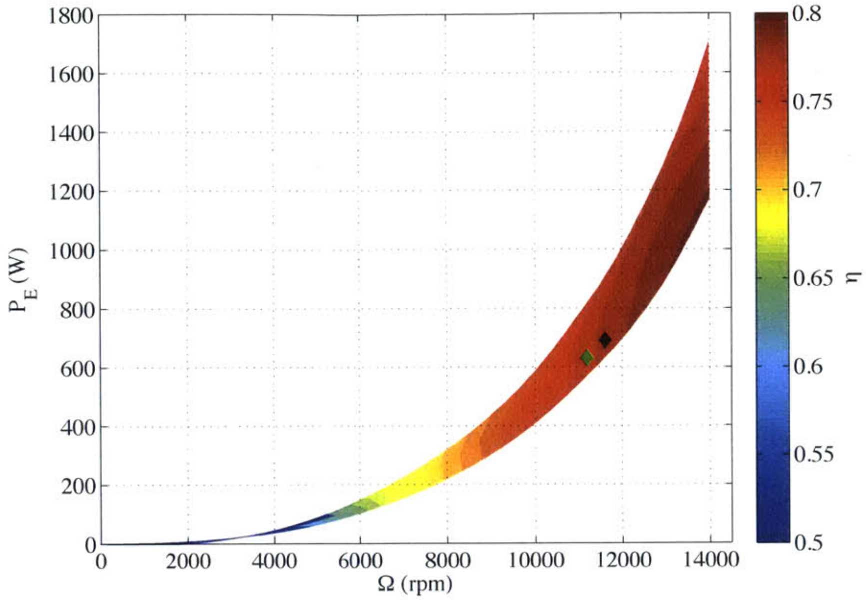

Figure 2-5: Contour of motor efficiency, $\eta_{\rm m}$, for motor 6. Langley test operating points are indicated by symbols, green for BLI and black for non-BLI configuration.

2.3 Sensitivity of Motor Efficiency to Testing Parameters

It is not possible to recreate the conditions as at Langley in the MIT 1x1 wind tunnel because the experiments were not carried out with the same external environment. In particular, motor temperature or, different electronic devices (electronic box and power supply) can influence the motor efficiency. This section looks at the sensitivity of motor efficiency to test parameters.

2.3.1 Temperature Effect

When the motor is started, the skin temperature increases, taking roughly 30 minutes to reach a steady value. It was thus not feasible to wait until the motor temperature reached the steady state at each motor speed, either during the tests carried out for the motor calibration or at Langley. As a result the motor temperature rose from approximately 20°C to 60°C during the runs. Because the temperature of the windings can influence the losses in the conversion of electrical power to shaft power, determining the changes in the motor efficiency due to temperature variations was necessary.

Measurements were carried out at fixed RPM while the temperature increased from 21.7°C to 53.1°C. To assess the influence of temperature only, the load cell reading was taken as the average over the different conditions[6] and the efficiency computed using Equation (2.1). The maximum efficiency difference was 0.5%, and the temperature effect is thus within the measurement uncertainty (see Section 2.4).

2.3.2 Electronics Variability Effect

The measurements of torque described in Section 2.2 were repeated with a different electronic box, power supply, and motor. The results are presented in Table 2.2 with the mean efficiencies and uncertainties expressed in percentages. The rightmost column shows the 95% confidence interval for each efficiency. The initial electronic box, power supply, and motor used were electronic box 1, power supply 1, and motor 6; the second set of experiments were conducted with electronic box 3, power supply 2, and motors 6, 9, and 16. For a given motor and power supply, the efficiency does not depend on the electronic box. However, when the power supply was replaced, the efficiency changed by 2.6% points, about four times the measurement uncertainty of 0.6% points. To avoid changes in efficiency due to the different power supply, each motor used during the Langley tests was calibrated using the same power supply as the one it was connected to at Langley. The effect of electronic box was negligible, and all calibration tests used electronic box 1.

---

[6] The load cell should in theory measures the same value for the same loading: the average force of the four measurements is 2.565 with a standard deviation of 0.005.

Table 2.2: Summary of motor efficiencies at simulated cruise conditions:(p) for non-BLI, (iL) for left BLI propulsor, and (iR) for right BLI propulsor

Electronic box	Power supply	Motor	Efficiency (%)	
1	1	9	78.2	± 0.4 (p)
			77.4	± 0.4 (iL)
			77.5	± 0.4 (iR)
3	1	9	78.2	± 0.4 (p)
			77.4	± 0.4 (iL)
			77.5	± 0.4 (iR)
1	1	16	80.6	± 0.6 (p)
			80.0	± 0.6 (iL)
			80.1	± 0.6 (iR)
1	2	16	78.2	± 0.4 (p)
			77.4	± 0.4 (iL)
			77.5	± 0.4 (iR)
1	1	6	78.2	± 0.4 (p)
			77.6	± 0.6 (iL)
			77.6	± 0.6 (iR)

2.4 Motor Efficiency Uncertainty Analysis

There are two types of uncertainties, or experimental errors, in any measured quantities [15]: (i) random errors, such as electronic noise, and (ii) systematic errors, such as calibration errors or varying flow conditions. While the actual systematic error cannot be known, the experimental repeatability measures the combined uncertainty of the variations in systematic error plus instrumentation uncertainty (this latter is a subset of the random error). Discussion of measurement repeatability is presented in Section 2.4.1 using a statistical approach for the evaluation of uncertainty. Section 2.4.2 gives the instrumentation uncertainties and describes how they are propagated to the quantity of interest: motor efficiency, η_{m}. The instrument uncertainty includes only the random uncertainties of the measurement devices.

2.4.1 Statistical Approach for Motor Efficiency: Measurement Repeatability

One way to estimate measurement uncertainty is through experiment repetition. The standard deviation gives information on the spread of the measurements, repeated N times, at the same experimental conditions. The efficiency uncertainty is based on a 95% confidence interval ($\alpha = 0.05$) for an average quantity using the t-distribution with standard deviation, $s_{\eta_{\mathrm{m}}}$ [16]. The efficiency is thus written as

$$\eta_{\mathrm{m}} = \overline{\eta_{\mathrm{m}}} \pm t_{1-\frac{\alpha}{2}(N-1)} \frac{s_{\eta_{\mathrm{m}}}}{\sqrt{N}}, \tag{2.2}$$

in which $\overline{\eta_{\mathrm{m}}}$ is the mean value, $t_{1-\frac{\alpha}{2}(N-1)}$ is the t-distribution correction factor, and $N = 4$ since four runs were performed at each condition. The Shapiro-Wilk test [17] performed for these four values for each combination of motor speed and propeller indicates that the hypothesis of normally distributed values cannot be rejected and it is appropriate to use the above t-distribution for the confidence interval.

Figure 2-6(a) shows efficiency versus RPM for the 10x08 propeller for motor 6. Black crosses represent the mean efficiencies, and the red line is a polynomial fit of order 5 of the efficiencies (chosen to best fit the data). Each point has an uncertainty error bar associated with it based on Equation (2.2) with magnitudes specified in Figure 2-6. The region of interest is shown with expanded scale in Figure 2-6(b). The error bars are 0.8% maximum of the absolute value with a 95% confidence. The results are summarized in Table 2.3 for the simulated cruise conditions for both motors 6 and 7.

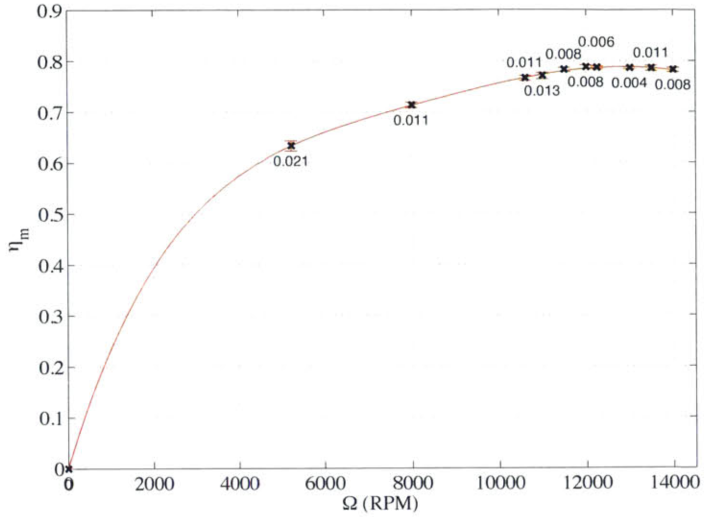

(a) Full range

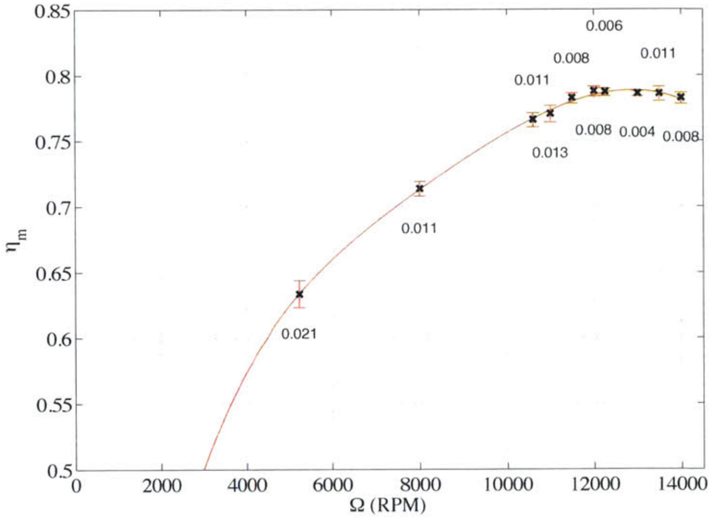

(b) Expanded view of region of interest

Figure 2-6: Polynomial fit of the mean efficiency with uncertainty error bars (electronic box 1, power supply 1, motor 6)

Table 2.3: Efficiency values at simulated cruise conditions for electronic box 1 and motors 6 and 7 with repeatability uncertainty at 95% confidence interval

Configuration	Ω (RPM)	P_E (W)	η_m (%)	Uncertainty (% point)
Non-BLI (left propulsor)	11600	690	78.2	± 0.4
Non-BLI (right propulsor)	11600	690	78.3	± 0.4
BLI (left propulsor)	11200	630	77.7	± 0.6
BLI (right propulsor)	11200	680	77.6	± 0.6

2.4.2 Propagation Approach for Motor Efficiency: Instrument Uncertainty

The measurement uncertainty can also be found through evaluation of the instrumentation uncertainty. The variations in motor speed, electrical power, and voltage measured by the load cell are independent of each other and the uncertainty in the final quantity of interest, motor efficiency, η_{m}, is obtained by propagating the individual uncertainties from these three variables.

The relevant quantities are:

W: weight used for calibration of the load cell
F_{N}: force in Newtons recorded by the load cell due to the weights
V_{LC}: load cell voltage
L_{LC}: moment arm length to load cell
L_{W}: moment arm length to weights
$k = \frac{F_{\mathrm{N}}}{V_{\mathrm{LC}}} = \frac{L_W}{L_{\mathrm{LC}}} \frac{F_W}{V_{\mathrm{LC}}}$: calibration factor
Ω: motor wheel speed for the operating points
P_{E}: motor electric power
Q: torque provided to the shaft
η_{m}: motor efficiency

Table 2.4 shows the uncertainties that correspond to the independent variables, given at a 95% confidence interval (2σ). The uncertainties in length and weight are estimates based on the ruler and the scale used to measure these variables. The uncertainties of the power supply and the load cell are from the instrument manufacturer specifications.

The motor speed is acquired from the back-EMF signal from the motor, with the

Table 2.4: Independent variables uncertainty for motor efficiency

Variables	L	W	V_{LC}	P_{E}	Ω
Uncertainty	0.5 mm	0.5 g	$0.0035V_{\mathrm{LC}}$	$0.012P_{\mathrm{E}}$	10 RPM

uncertainty in motor speed evaluated using a photogate[7]. Direct comparison between values acquired from the back-EMF signal and the photogate allows us to estimate the uncertainty in the motor speed. Figure 2-7 shows an example, at 11500 RPM, of the signal from the photogate in red and from the back-EMF signal in black for a minute and a half time interval. The time averages are also given. The photogate measurements confirm the use of back-EMF signal for the motor speed acquisition and indicate the motor speed uncertainty to be 10 RPM. The biggest uncertainty between all wheel speeds is used and taken as a constant in our estimates because, as demonstrated later in this section, the contribution of motor speed uncertainty is small compared to other uncertainties.

The uncertainties of the independent measurements, denoted by U, are propagated to the calibration factor, k, and torque, Q, as follow:

$$\frac{U_k}{k} = \sqrt{\left(\frac{U_{L_W}}{L_W}\right)^2 + \left(\frac{U_{L_{\mathrm{LC}}}}{L_{\mathrm{LC}}}\right)^2 + \left(\frac{U_{F_W}}{F_W}\right)^2 + \left(\frac{U_{V_{\mathrm{LC}}}}{V_{\mathrm{LC}}}\right)^2} = 0.0049,$$

$$\frac{U_Q}{Q} = \sqrt{\left(\frac{U_k}{k}\right)^2 + \left(\frac{U_{V_{\mathrm{LC}}}}{V_{\mathrm{LC}}}\right)^2 + \left(\frac{U_{L_{\mathrm{LC}}}}{L_{\mathrm{LC}}}\right)^2} = 0.0065. \quad (2.3)$$

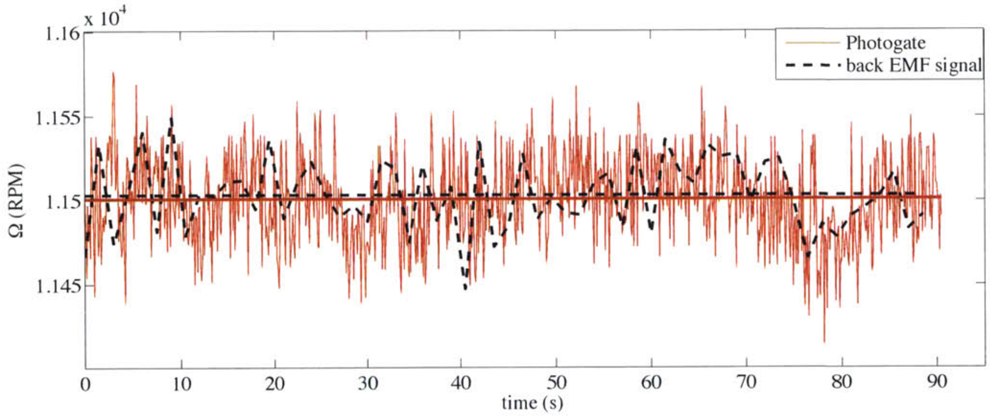

Figure 2-7: RPM measurements from the photogate and the back-EMF signal with their time averages

---

[7] The propeller attached to the motor shaft cuts an infra-red beam created by the photogate and the time is recorded to obtain the wheel speed.

The uncertainty in efficiency,

$$\frac{U_{\eta_{\mathrm{m}}}}{\eta_{\mathrm{m}}} = \sqrt{\left(\frac{U_Q}{Q}\right)^2 + \left(\frac{U_\Omega}{\Omega}\right)^2 + \left(\frac{U_{P_{\mathrm{E}}}}{P_{\mathrm{E}}}\right)^2}, \tag{2.4}$$

varies with the motor speed and is given in Table 2.5. The fractional estimated uncertainty in efficiency over the cruise condition range (between 10600 and 12000 RPM) is constant at $\frac{U_{\eta_{\mathrm{m}}}}{\eta_{\mathrm{m}}} = 0.0129$.

The percentage contributions of the different sources of error to the uncertainties in the calibration factor, torque, and motor efficiency are given in Figure 2-8. The upper plot in the figure illustrates the different contributions to the uncertainty in the calibration factor. The main source of uncertainty is from the load cell. To improve this, a higher quality load cell could be used. However the results do not indicate a need to do this since uncertainty with the present arrangements is below the 1% target. The second plot shows different contributions to torque uncertainty, with the biggest contribution from the calibration factor; again a higher quality load cell could decrease the calibration factor uncertainty. The bottom plot shows the contributions to efficiency uncertainty. The uncertainty in motor speed is much smaller than the uncertainty from the torque or the electrical power, and the electrical power uncertainty contributes the most.

The efficiency uncertainties in Table 2.5 apply to a single set of measurements, i.e. one data point for each RPM for each propeller. This uncertainty can be reduced, as described in Section 2.4.1, by using N multiple data sets, such that the uncertainty on the mean is

$$U_{\bar{\eta_{\mathrm{m}}}} = \frac{U_{\eta_{\mathrm{m}}}}{\sqrt{N}}. \tag{2.5}$$

Two different methods of calculating uncertainty were described, and the results

Table 2.5: Fractional uncertainties in the efficiency

Ω (RPM)	5250	8000	10600	11000	11600	12000	12500	14000	14500
$\frac{U_{\eta_{\mathrm{m}}}}{\eta_{\mathrm{m}}}(10^{-2})$	1.33	1.30	1.29	1.29	1.29	1.29	1.29	1.29	1.29

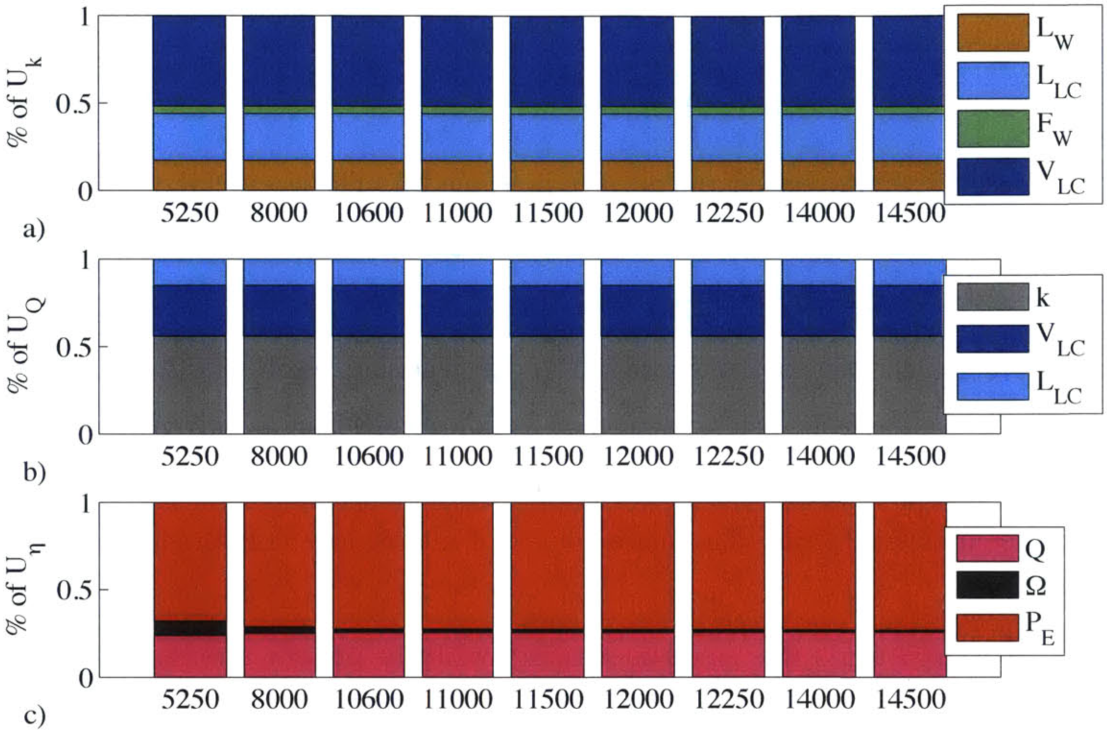

Figure 2-8: Relative contributions of the different sources in percentage on the different uncertainties: a) Calibration factor; b) Torque; c) Efficiency

of the two methods are summarized in Table 2.6. The uncertainties are found to differ by 0.1% points between the two methods. For the BLI propulsor and the right non-BLI propulsor, the propagation method underestimates the uncertainty since it does not account for systematic errors and the influence of other parameters (external conditions, change in setup and so on). Whenever a motor efficiency uncertainty is given, it is the statistical uncertainty that is quoted.

Table 2.6: Comparison between uncertainties from the statistical method and the propagation method on motor efficiency in %

Configuration	Mean efficiency	Statistical uncertainty	Propagation uncertainty
Non-BLI (left propulsor)	78.2	±0.4	±0.5
Non-BLI (right propulsor)	78.3	±0.4	±0.5
BLI (left propulsor)	77.7	±0.6	±0.5
BLI (right propulsor)	77.6	±0.6	±0.5

2.5 Summary

A dynamometer to calibrate the motor used in the D8 model propulsors during the Langley tests was designed, fabricated, tested, and used to quantify motor efficiency at the various propulsor operating points. The results of the experiments with the dynamometer showed that the motor efficiencies at simulated cruise conditions are 78.2% and 78.3%, for the left and right propulsors respectively, at conditions representative of the non-BLI configuration, and 77.6% and 77.7%, for the left and right motors respectively, at conditions representative of the BLI configuration. The uncertainty is ± 0.6% points for both non-BLI and BLI configurations at a 95% confidence level. The motor efficiency for conditions corresponding to the non-BLI configuration is 1% higher than that for conditions corresponding to the BLI configuration because in the latter case the motor operates at lower power level and further away from peak efficiency. The measured efficiencies and the uncertainties can be used to convert the electrical power measurement recorded during the NASA Langley experiments into shaft power, a necessary step in evaluating the BLI aerodynamic benefit.

Chapter 3

Measurement of BLI Benefit I: Indirect Method

The aerodynamic BLI benefit was defined in Equation (1.2) as the percentage of reduction in mechanical flow power coefficient, C_{P_K}, from the non-BLI to the BLI configurations. One way of evaluating the benefit is via the indirect method, namely to use $P_\mathrm{K} = \eta_\mathrm{m}\eta_\mathrm{f}P_\mathrm{E}$. There are thus two steps to evaluate the BLI benefit. One is the conversion of electrical power, measured at Langley, into shaft power via the motor calibration experiments: $P_\mathrm{S} = \eta_\mathrm{m}P_\mathrm{E}$. The second is the conversion of shaft power into the mechanical flow power input to the flow, via the propulsor characterization experiments: $P_\mathrm{K} = \eta_\mathrm{f}P_\mathrm{S}$. This metric takes into account the difference in fan efficiency and power between the different experiments.

The motor calibration experiments was explained in Chapter 2. The propulsor characterization experiments are described in this chapter.

3.1 Propulsor Characterization

The conversion of shaft power into mechanical flow power is achieved by assessing the efficiency of the Aero-naut TF8000 fans[1]. The propulsor characterization experiments were carried out by Siu, and they are detailed in her master's thesis [1]. However, a

---

[1] A commercial, off-the-shelf electric ducted fan, typically used for R/C models.

brief explanation and update is given here.

3.1.1 Setup

The propulsor characterization experiments were performed using the MIT Gas Turbine Laboratory 1x1 foot open test section wind tunnel. A contraction was added at the opening of the wind tunnel followed by a constant area duct and another contraction to match the propulsor inlet diameter (5.7 inches). Distortion screens were designed and constructed to replicate the flow non-uniformity due to the BLI on the 1:11 scale powered D8 model. The screens were installed in the constant area duct. Tests without a screen gave a uniform inlet flow representative of the flow into the propulsors of the non-BLI configuration, while screens replicated the flow seen by the propulsors of the BLI configuration. It was not possible to recreate the inlet swirl distortion as present on the model. Siu [1] evaluated that there is no effect on the BLI benefit because of cancellation effect due to the opposite rotation of the swirl on the propulsors. Figure 3-1 shows a side view of the contraction, the duct, the screen, the propulsor, the different stations, and the pressure taps locations.

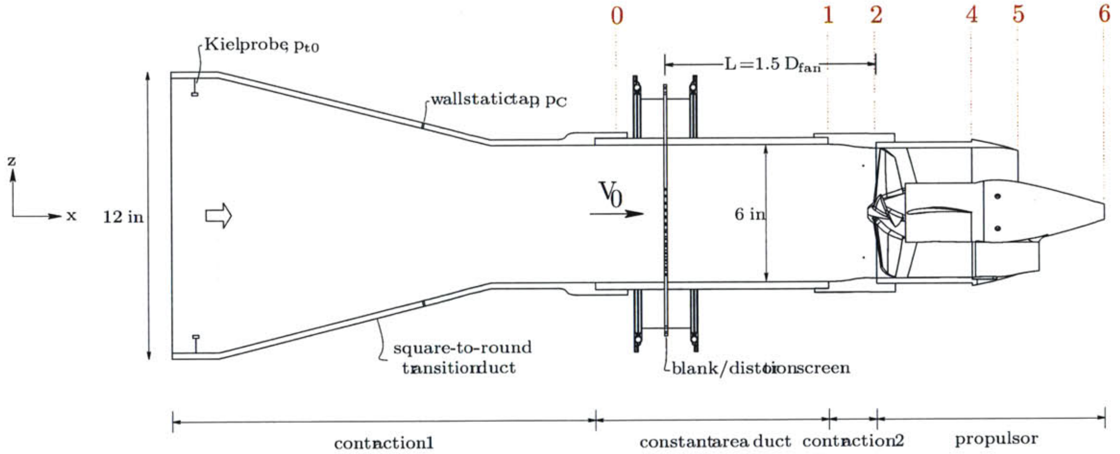

Figure 3-1: Setup for the propulsor characterization experiments. Credit: Siu.

3.1.2 Methodology

The turbomachinery quantities of interest are flow coefficient, ϕ, stagnation pressure rise coefficient, ψ, mechanical flow power, P_{K}, and overall efficiency, η_{o}. The flow coefficient,

$$\phi = \frac{V_{\mathrm{x}}}{U_{\mathrm{tip}}}, \tag{3.1}$$

where $U_{\mathrm{tip}} = \Omega \frac{D_{\mathrm{fan}}}{2}$, is controlled by varying either the freestream tunnel velocity, V_{∞}, or the tip fan velocity, U_{tip}. The rotor tip radius is $\frac{D_{\mathrm{fan}}}{2} = 0.072$ m. The stagnation pressure rise coefficient, ψ, which depends on the operating conditions, the density, and the tip fan velocity, is given by

$$\psi = \frac{\Delta \overline{p_0}}{\rho U_{\mathrm{tip}}^2}, \tag{3.2}$$

in which $\Delta \overline{p_0}$ is the difference in mass-average stagnation pressure between propulsor exit (station 5 in Figure 3-1) and inlet (station 2 in Figure 3-1) planes. A straight five-hole probe[2] (FHP), shown in Figure 3-2, was used to survey the propulsor inlet and exit planes. The probe had four holes around a middle hole to determine the three components of velocity (or flow angles), static pressure, and stagnation pressure. The density, ρ, is obtained by recording the room atmospheric pressure using a mercury manometer and the temperature inside the wind tunnel using a thermocouple.

The mechanical flow power is the volume flux of stagnation pressure [9] or a measure of mechanical flow power added to the flow,

$$P_{\mathrm{K}} = \oiint \left(p_{\mathrm{o},\infty} - p_{\mathrm{o}}\right) \mathbf{V} \cdot \hat{n}\, dS = \widetilde{P}_{\mathrm{K,out}} + \widetilde{P}_{\mathrm{K,in}}, \tag{3.3}$$

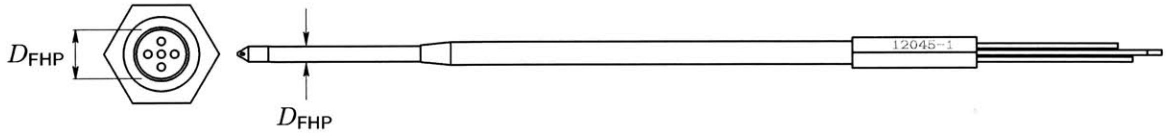

Figure 3-2: Straight five-hole probe

---

[2] Conventional five-hole probe designed by AEROPROBE Corporation.

where $\widetilde{P}_{\mathrm{K}} = \iint (p_{\mathrm{o},\infty} - p_{\mathrm{o}})\,\mathbf{V}\cdot\hat{n}\,dS$ represents the integration of the difference between the freestream stagnation pressure and the stagnation pressure obtained with the FHP in the measurement plane. Equation (3.3) is evaluated along the control volume shown in Figure 3-3. The convention is that the normal vector, $\hat{n}$, points into the propulsor because the control volume is for the flow so $\widetilde{P}_{\mathrm{K,out}} > 0$ and $\widetilde{P}_{\mathrm{K,in}} > 0$. In the stagnation pressure flux, there are only contributions from the inlet and exit surfaces, 1 and 4. The exit contribution includes both the nozzle contribution and the plug exit contribution. This latter is obtained via pressure ports in the plug (the mechanical flow power from the plug is less than 1% of the total mechanical flow power [1]).

The overall efficiency quantifies the loss associated with the conversion of the electrical power, P_{E}, into mechanical flow power, P_{K}, namely

$$\eta_{\mathrm{o}} = \frac{P_{\mathrm{K}}}{P_{\mathrm{E}}} = \frac{\widetilde{P}_{\mathrm{K,out}} + \widetilde{P}_{\mathrm{K,in}}}{P_{\mathrm{E}}} = \eta_{\mathrm{f}}\eta_{\mathrm{m}}. \tag{3.4}$$

The mechanical flow power, P_{K}, is computed from the FHP surveys, and the electrical power, P_{E}, is measured, so the overall efficiency, η_{o}, can be found at different operating points. The fan efficiency, η_f, is separately accessible because the motor efficiency was determined, as in Chapter 2.

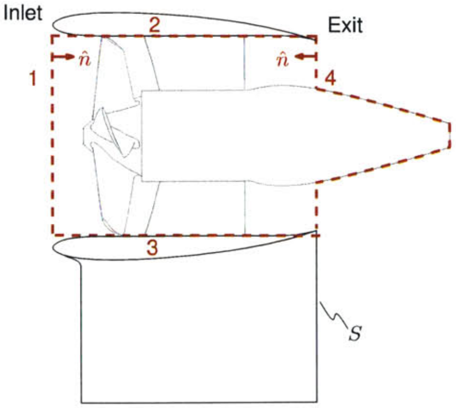

Figure 3-3: Control volume for mechanical flow power integration

3.1.3 Data Analysis

An indicator of the accuracy of the FHP surveys is a comparison of mass flow from inlet and exit of the propulsor, they should be equal. The FHP measurements indicate a difference in mass flow of between 2 and 3%, with the inlet mass flow being larger. The calibration of the FHP is assumed to be adequate in a non-uniform flow, i.e. boundary layer or, shear layer, and the fact that the mass flow is different from inlet to exit put this assumption into question. A detail analysis of the inlet and exit experiments is given in Appendix A. All the analysis carried by Siu [1] or here relied on the assumption of constant density from the inlet to the exit of the propulsor. Estimates of the density changes using mass-average stagnation pressure rise coefficient showed the density difference was within 0.5% (see Appendix B). The evaluation of the uncertainty, however, is on-going. All the data presented in this chapter are thus the data of the fan characterization experiments obtained with a measured 2-3% difference in mass flow from inlet to exit and with constant density.

3.1.4 Propulsor Characterization Results

For a given Langley operating point, wheel speed and electrical power are known, so the rotational Reynolds number, $R_{e,\theta}$, defined as

$$R_{e,\theta} = \frac{\rho U_{\mathrm{tip}} c_{\mathrm{tip}}}{\mu} \tag{3.5}$$

and the electrical power coefficient, $C_{P_{\mathrm{E}}}$, defined as

$$C_{P_{\mathrm{E}}} = \frac{P_{\mathrm{E}}}{0.5 \rho_\infty V_\infty^3 S_{\mathrm{ref}}} \tag{3.6}$$

are both known. Here, c_{tip} is the rotor tip chord (0.04 m), μ is the air viscosity, and A_{f} is the fan face area (0.0159 m^2).

For a fixed propulsor[3] and wheel speed, the stagnation pressure rise coefficient,

---

[3] Experiments were run for the same propulsor, i.e. same fan, motor, and nacelle, at various conditions.

overall efficiency, and fan efficiency depend only on the flow coefficient, which can be controlled through setting the wind tunnel speed. The output of the propulsor calibration experiments is thus a file containing the curve-fits of the quantities of interest $(\psi, \eta_\mathrm{o}, \eta_\mathrm{f})$ as a function of flow coefficient, ϕ, for a given wheel speed, Ω, or rotational Reynold number, $R_{e,\theta}$ in non-dimensional terms.

Curve-fits of $(\eta_\mathrm{m}, \psi, \eta_\mathrm{o}, \eta_\mathrm{f})$ versus ϕ are plotted in Figures 3-4, 3-5, and 3-6. Each color corresponds to a different wheel speed: red for 8000 RPM, green for 10600 RPM, orange for 12250 RPM, blue for 13500 RPM, and black for 14000 RPM. The squares and the circles correspond to the left and right propulsors, respectively, and to the cases with no screen, i.e. no distortion. The triangles and the crosses show the cases with a screen simulating the BLI distortion, again for the left and right propulsor, respectively. These results are different from those of Siu [1] because the motor calibration setup was improved, with changed motor efficiencies.

From Figure 3-4, the motor efficiency depends on the rotational Reynolds number (or wheel speed), but not on the aerodynamic loading (or flow coefficient) since the curves for each wheel speed are flat. The motor behavior depends only on the rotational Reynolds number since the different curves associated with one color (specific wheel speed) superimpose with each other, whether the motor is from the left or right propulsor, or whether or not distortion is introduced.

The stagnation pressure rise coefficient is plotted in Figure 3-5(a) and characteristics show no sharp changes in stagnation pressure rise coefficient which might indicate the absence of blade stall.

The overall efficiency is shown in Figure 3-5(b). There is 4% difference at most in overall efficiency between the left propulsor and the right propulsor, in spite the lack of difference in motor efficiency. Therefore variations in overall efficiency are due to fan efficiency changes, both of which depend on the rotational Reynolds number. There is more manufacturing variability between fans than between motors.

Figure 3-6 shows fan efficiencies for the uniform flow cases in the top plot (a), and the distorted case in the bottom plot (b). There is a fan efficiency loss with distortion, as expected, since the fan handles a non-uniform flow that it was not optimized nor designed for. An important consideration when designing a fan for operation in distorted flow is thus to mitigate the loss in efficiency. While the mechanical flow power, P_{K}, is independent of the specifics of the propulsor, the shaft power, $P_{\mathrm{S}} = \frac{P_{\mathrm{K}}}{\eta_{\mathrm{f}}}$, could increase with BLI if the fan efficiency loss is high (this is one of the reasons why the BLI benefit for the D8 was uncertain and needed to be evaluated).

For the Langley tests, the cruise wheel speed at 70 mph is approximately 10600 RPM and 13500 RPM at 84 mph. The efficiencies for these speeds are plotted in Figure 3-7. Figure (a) is at 10600 RPM and figure (b) is at 13500 RPM. The simulated cruise flow coefficient for the BLI case is between 0.36 and 0.37. For the non-BLI case, the simulated cruise condition is between 0.33 and 0.36. In these regions, the data and the extrapolation show that the fan behaves properly and the effect of distortion is bigger for the right motor (2.0%).

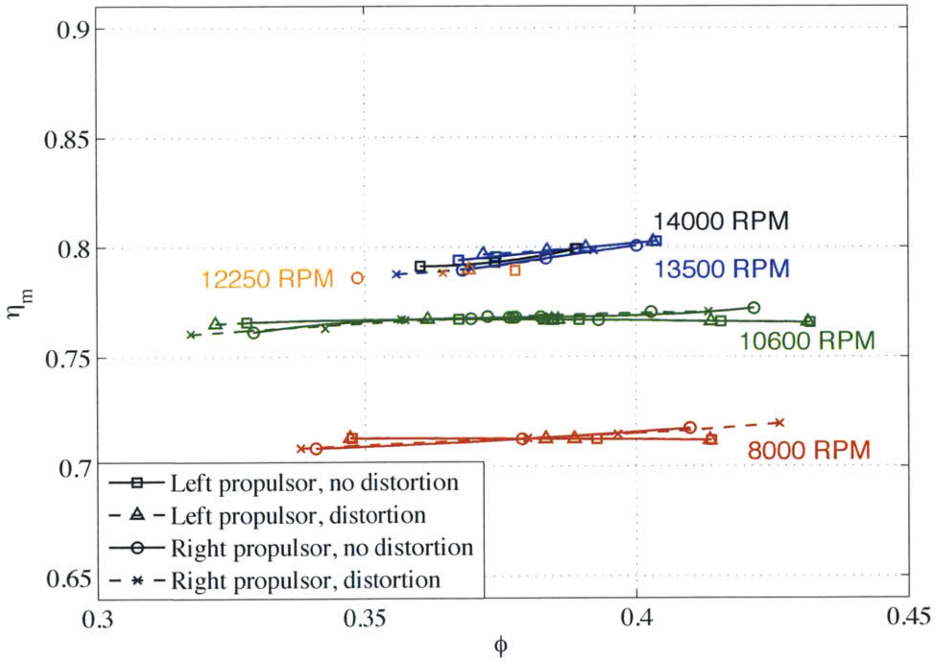

Figure 3-4: Motor efficiency against flow coefficient for both propulsors, different wheel speeds, and distorted or non-distorted flow

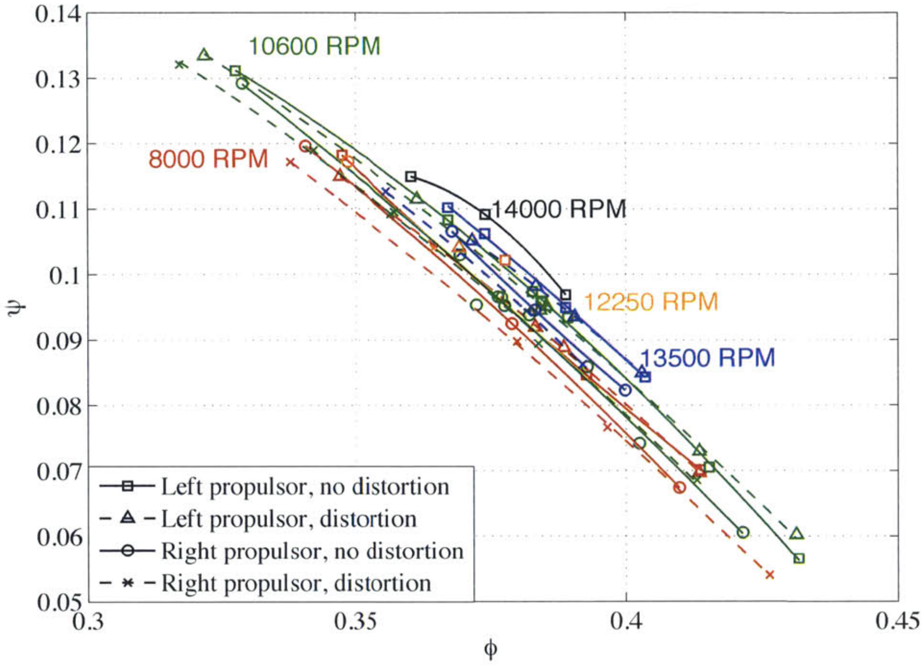

(a) Stagnation pressure rise coefficient

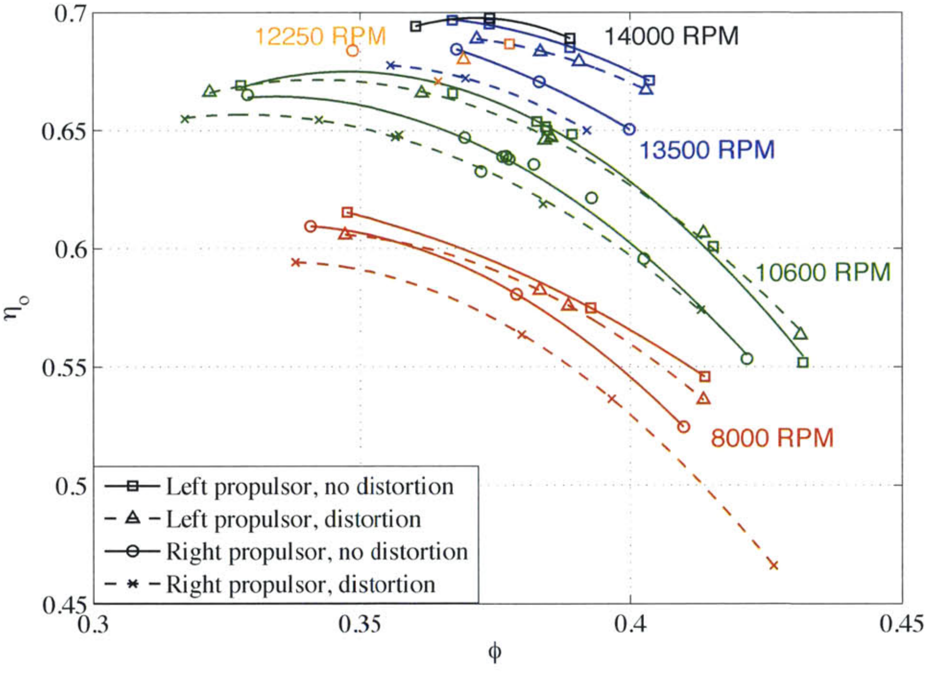

(b) Overall efficiency

Figure 3-5: (a) Stagnation pressure rise coefficient and (b) overall efficiency against flow coefficient for both propulsors, different wheel speeds, and distorted or non-distorted flow

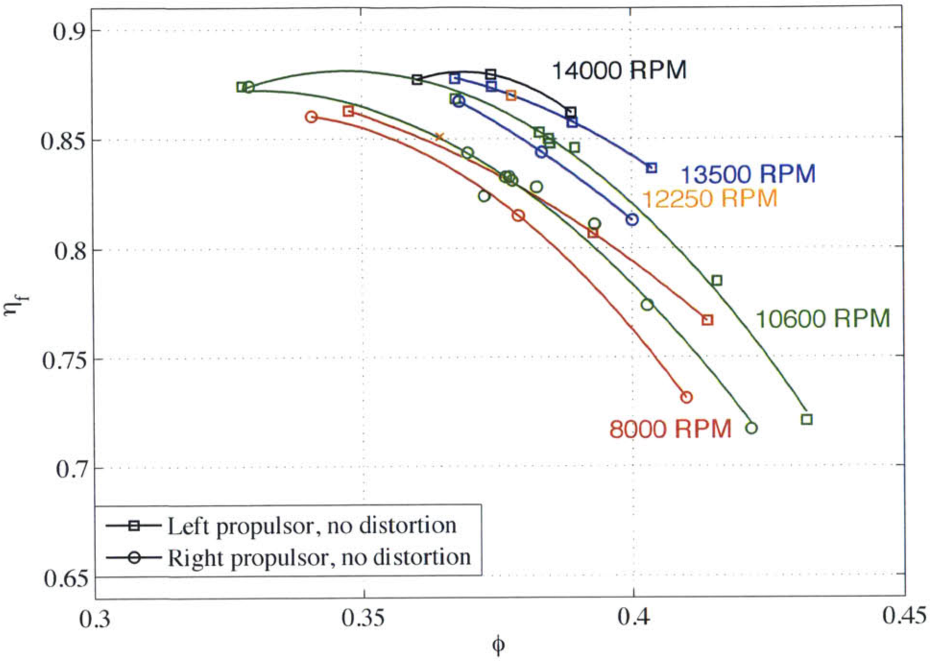

(a) no-distortion

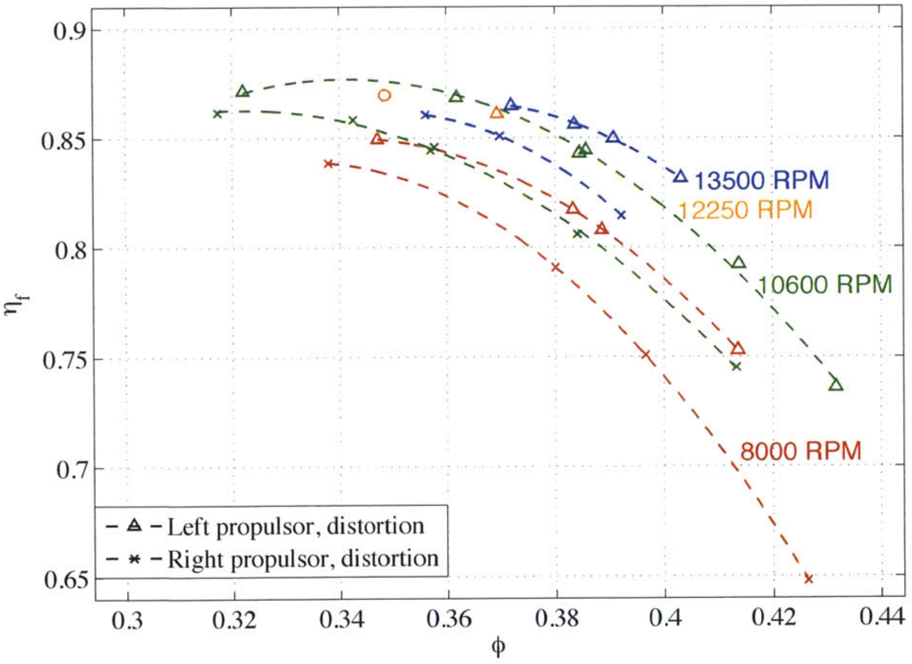

(b) distortion

Figure 3-6: Fan efficiency against flow coefficient for both propulsors, different wheel speeds, and a) non-distorted and b) distorted flow

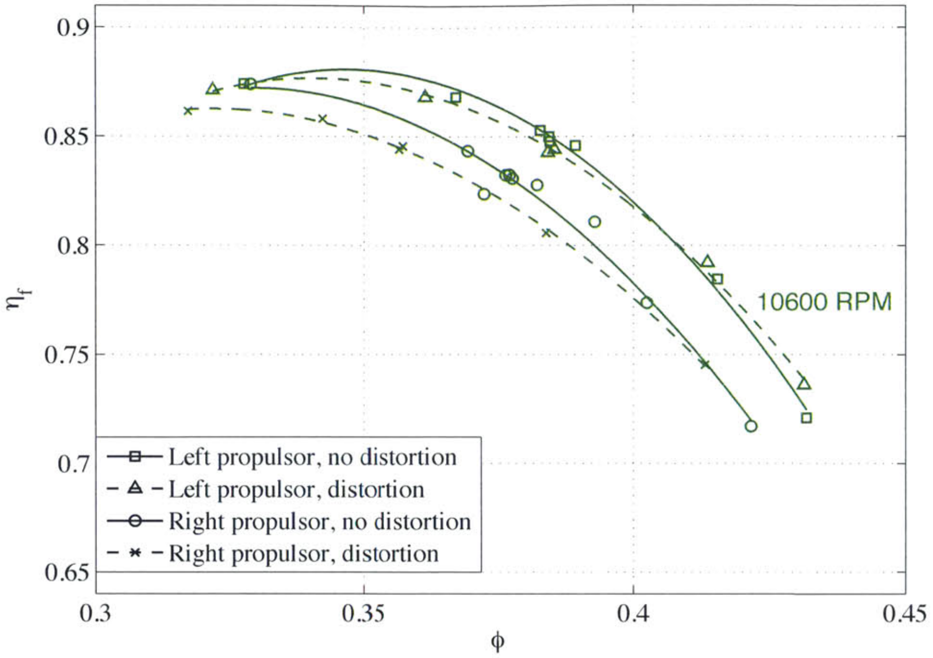

(a) 10600 RPM

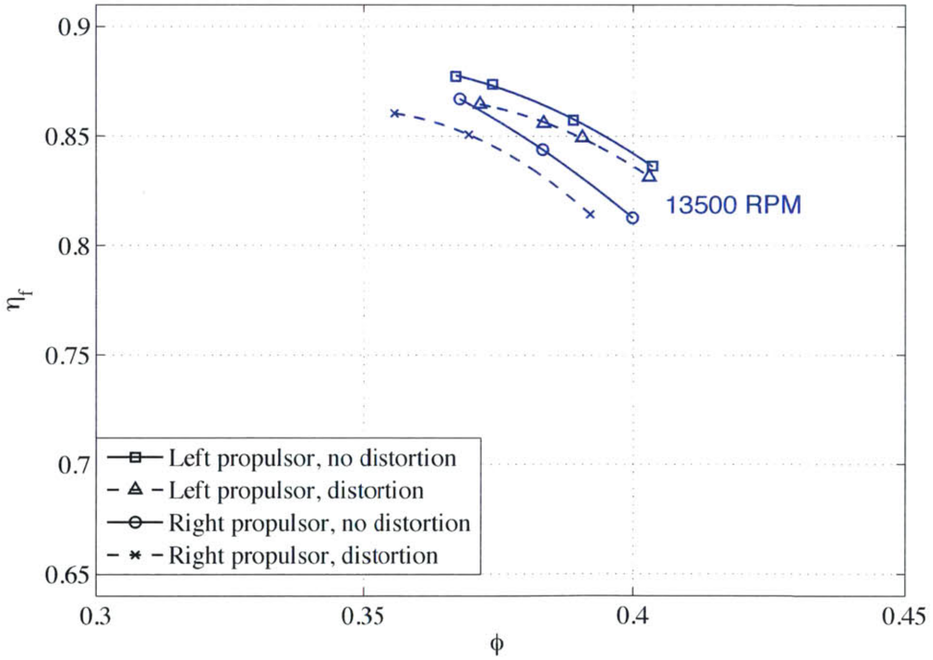

(b) 13500 RPM

Figure 3-7: Fan efficiency against flow coefficient for both propulsors, with distorted and non-distorted flow at a) 10600 RPM (Langley cruise at 70 mph), and b) 13500 RPM (Langley cruise at 84 mph)

3.2 Procedure for Matching Langley and MIT Operating Conditions

As mentioned earlier the goal is to convert the measured electrical power in the Langley experiments into mechanical flow power. The definition of mechanical flow power, mass flow, and stagnation pressure rise coefficient give

$$\psi(\phi)\phi = \frac{\eta_{\mathrm{f}}(\phi)\eta_{\mathrm{m}}(\phi)P_{\mathrm{E}}}{\rho U_{\mathrm{tip}}^3 A_{\mathrm{f}}}. \tag{3.7}$$

In Equation (3.7), the electrical power, the density, and the wheel speed come from the Langley experiments, while the stagnation pressure rise coefficient, fan efficiency, and motor efficiency come from the supporting MIT experiments. For a specific operating point (fixed wheel speed and electrical power), the stagnation pressure rise coefficient and fan efficiency are functions of flow coefficient only, so the flow coefficient corresponding to the Langley experiments can be uniquely determined from Equation (3.7). Fan efficiency is thus known and mechanical flow power is determined through Equation (3.4). Then, for any given condition as set by electrical power, P_{E}, and tip wheel speed, U_{tip}, fan and motor efficiencies can be known, and the mechanical flow power, $P_{\mathrm{K}} = \eta_{\mathrm{m}}\eta_{\mathrm{f}}P_{\mathrm{E}}$, determined.

3.3 BLI Benefit Results for the Indirect Method

3.3.1 Repeatability of the NASA Langley 14x22-Foot Wind Tunnel Data

There were two entries in the NASA Langley 14x22-foot subsonic wind tunnel. The maximum wind tunnel speed for Entry 1 was 70 mph primarily because of concern about motor temperature. The maximum wind tunnel speed was increased to 84 mph for Entry 2, enabling a reduction in statistical uncertainty (data repeatability) of 0.4%. Runs at 70 mph were also performed during Entry 2 to evaluate wind tunnel repeatability.

The results for the BLI configuration from the two entries are shown in Figures 3-8, 3-9, 3-10, and 3-11 for conditions of 70 mph, plug 3, and an angle of attack of 2°. There are approximately ten points per condition so there are eighty points in total. Figure 3-8(a) shows net streamwise force coefficient, C_{X}, against electrical power coefficient, $C_{P_{\mathrm{E}}}$. The red dashed curve corresponds to data from Entry 1 with motors 6 and 7, the magenta solid curve corresponds to data from Entry 2 with motors 16 and 13, and the orange dotted curve corresponds to data from Entry 2 with motors 9 and 15. The measured electrical power is dependent on both fan and motor efficiencies, leading to a scatter of ±0.39% at cruise between the different motor sets.

Figure 3-8(b) shows net streamwise force coefficient, C_{X}, versus shaft power coefficient, $C_{P_{\mathrm{S}}} = P_{\mathrm{S}}/0.5\rho_{\infty}V_{\infty}^{3}S_{\mathrm{ref}}$. Shaft power depends on the fan characteristics, and not on the motors, and all the data from 2013 and 2014 collapse into a single operating curve within a scatter of ± 0.45% at simulated cruise for 70 mph. Note that the same fan stages, and the same propulsors were used for both entries. The fact that shaft power data superimpose for both entries shows that the motor efficiencies calculated in the MIT experiments are correct.

A quadratic curve-fit of the eighty points is presented in Figure 3-9, again at 70 mph, with plug 3, and 2° angle of attack. Figure 3-9(a) shows net streamwise force coefficient versus electrical power and Figure 3-9(b) shows net streamwise force coefficient versus shaft power.

The corresponding curves for 84 mph are plotted in Figure 3-10. The scatter is ± 0.24% at this higher speed due to the reduced uncertainty.

3.3.2 Mechanical Flow Power Results: BLI Benefit

The BLI benefit is given by the difference in mechanical flow power between the BLI and the non-BLI configurations. The net streamwise force coefficient, C_{X}, is plotted as a function of mechanical flow power coefficient, $C_{P_{\mathrm{K}}}$, in Figure 3-11 at 70 (Figure 3-11(a)) and 84 mph (Figure 3-11(b)).

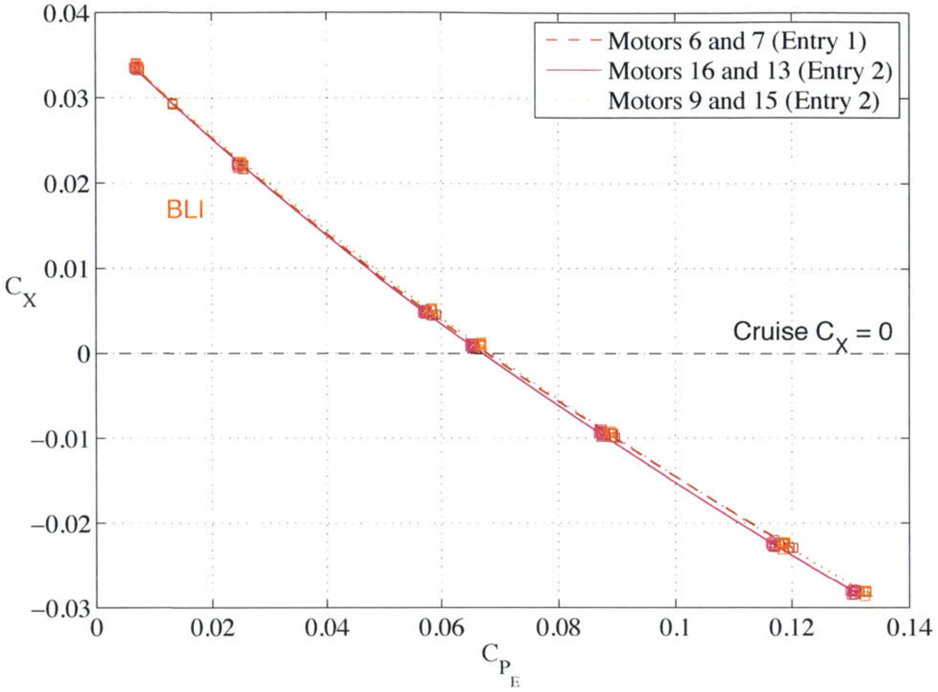

(a) Electrical power coefficient

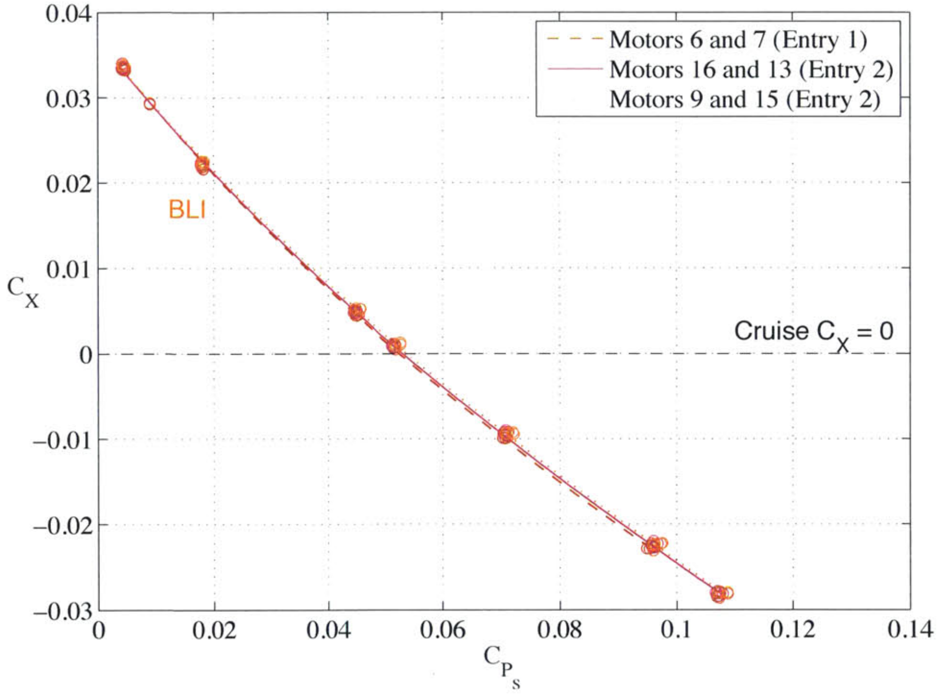

(b) Shaft power coefficient

Figure 3-8: Net streamwise force coefficient against a) electrical power coefficient and b) shaft power coefficient at 70 mph, plug 3, and 2° angle of attack for the BLI configuration. The dashed line at $C_X = 0$ indicates the simulated cruise condition.

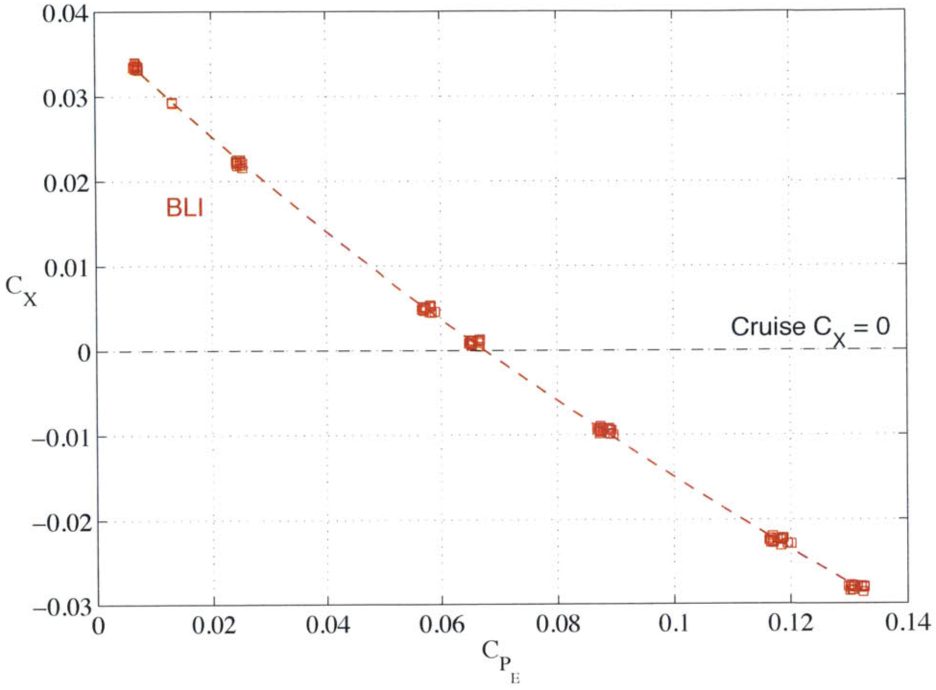

(a) Electrical power coefficient

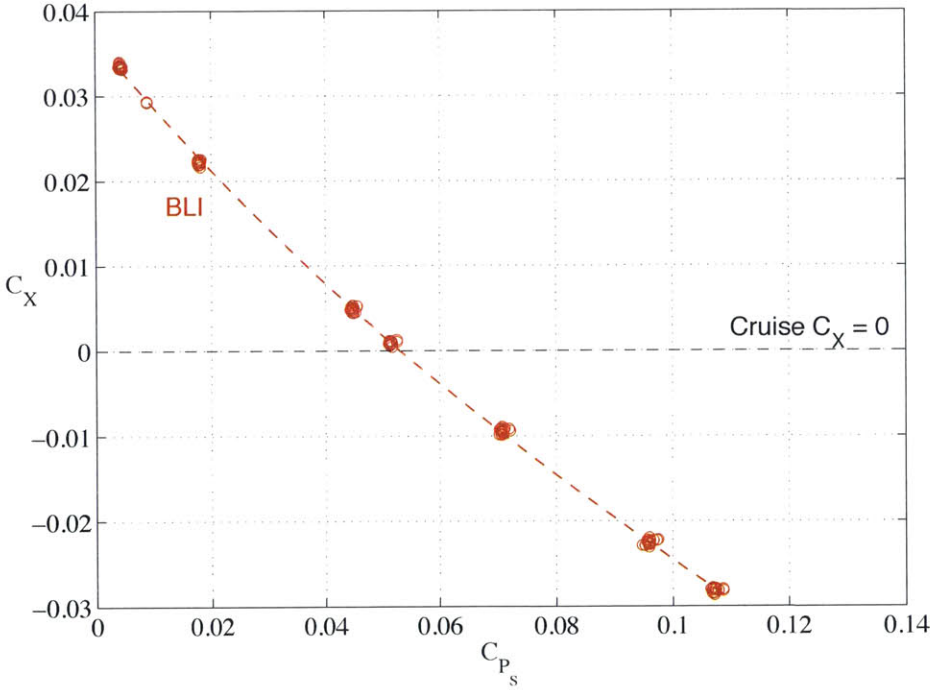

(b) Shaft power coefficient

Figure 3-9: Curvefits of net streamwise force coefficient against a) electrical power coefficient and b) shaft power coefficient at 70 mph, plug 3, and 2° angle of attack for the BLI configuration. The dashed line at $C_X = 0$ indicates the simulated cruise condition.

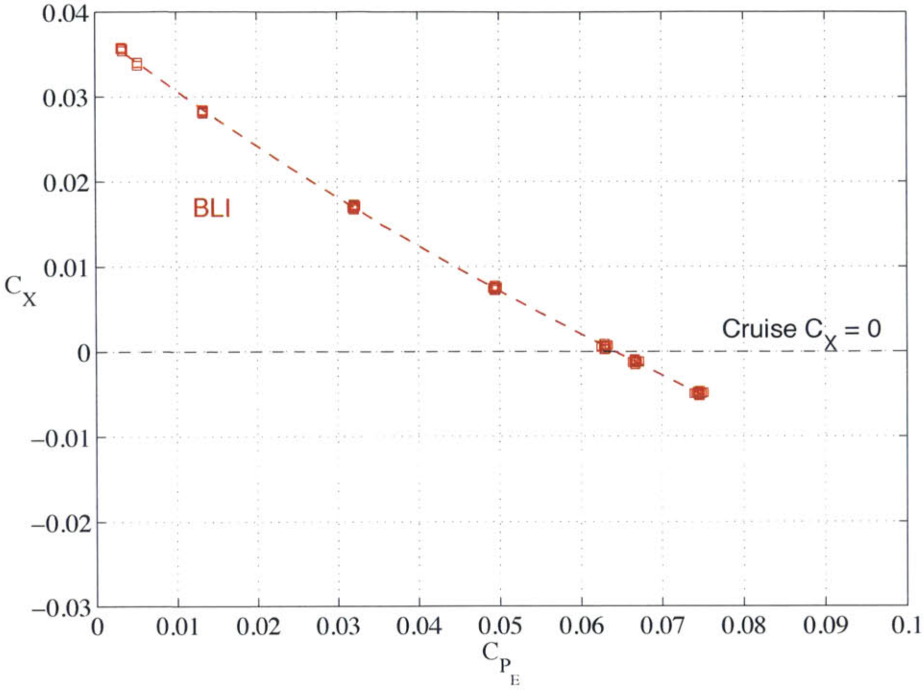

(a) Electrical power coefficient

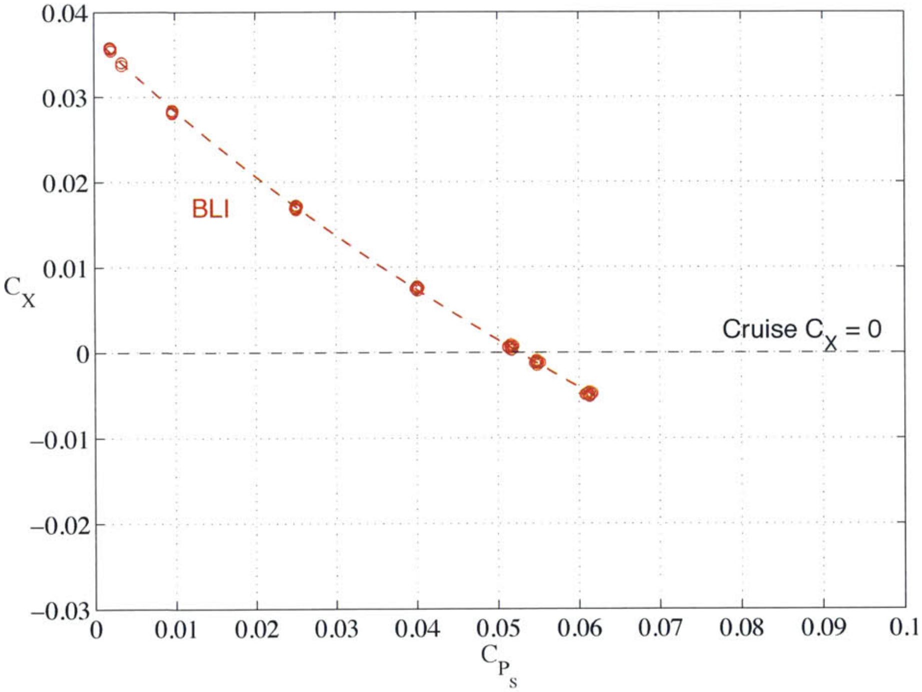

(b) Shaft power coefficient

Figure 3-10: Curvefits of net streamwise force coefficient against a) electrical power coefficient and b) shaft power coefficient at 84 mph, plug 3, and 2° angle of attack for the BLI configuration. The dashed line at $C_X = 0$ indicates the simulated cruise condition.

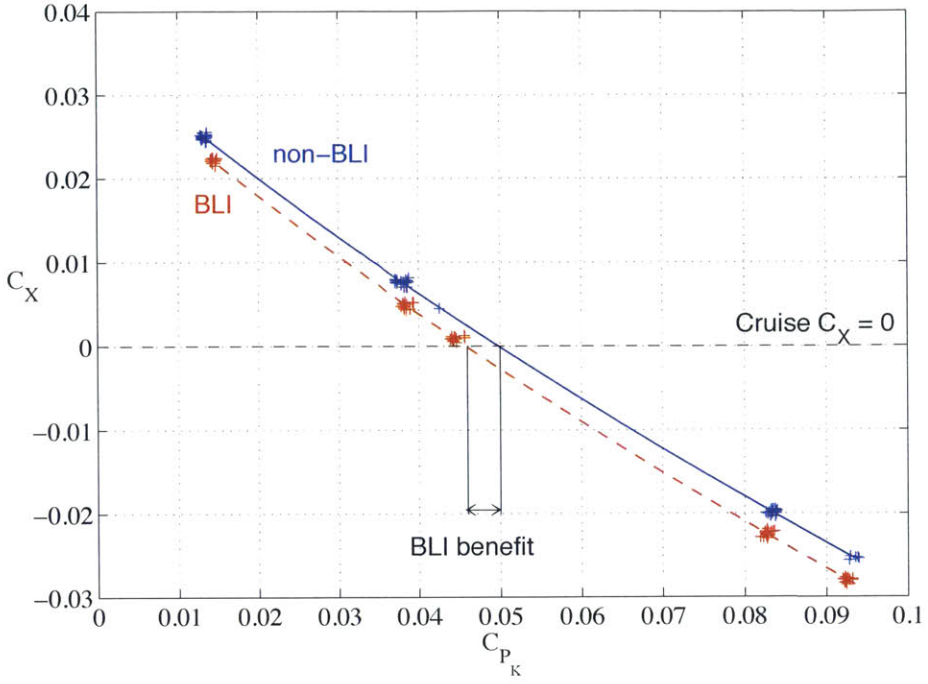

(a) 70 mph

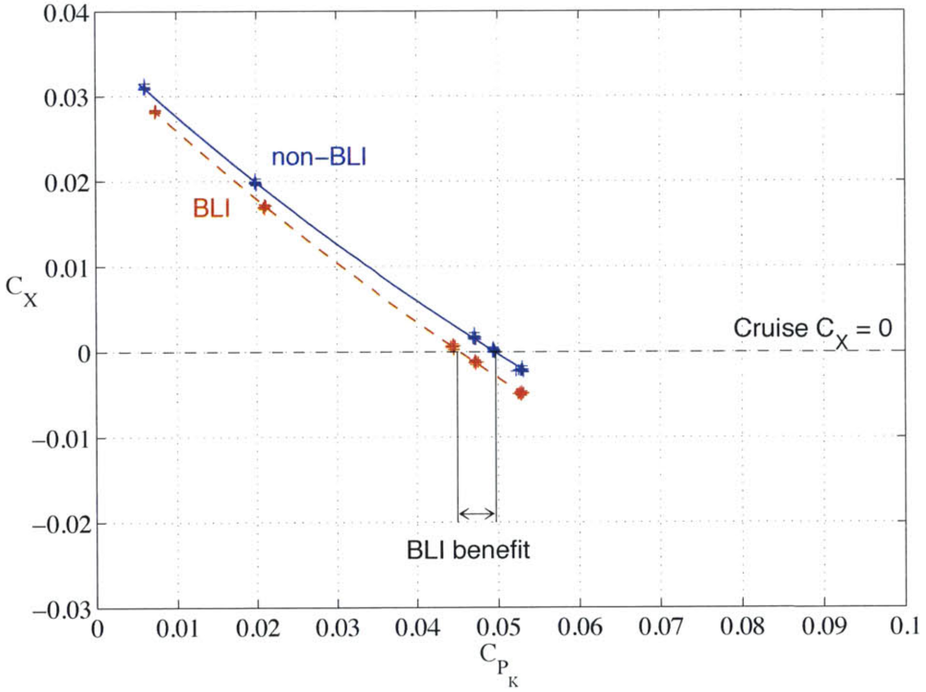

(b) 84 mph

Figure 3-11: Net streamwise force coefficient against flow power coefficient at a) 70 mph and b) 84 mph, plug 3, and 2° angle of attack for both the non-BLI and the BLI configurations. The dashed line at $C_X = 0$ indicates the simulated cruise condition.

The blue solid curve shows the curve-fit for data from the non-BLI configuration, and the red dashed curve is for the BLI configuration. At any net streamwise force, the mechanical flow power required by the BLI configuration is less than the mechanical power for the non-BLI configuration. The dashed black line indicates the simulated cruise condition, $C_{\mathrm{X}} = 0$, at which the BLI benefit is 7.9% at 70 mph and 8.5% at 84 mph for plug 3.

In summary, the goal of decreasing the uncertainty by running at higher wind tunnel speed was achieved. The statistical uncertainty in BLI benefit decreased from 0.8% at 70 mph to 0.4% at 84 mph, reflecting both a reduction in force-balance uncertainty and an increase in the number of repeated points. Also, comparison of the BLI benefit at 70 and 84 mph indicates no statistically significant Reynolds number dependence between the two conditions.

3.3.3 Explanation of the BLI Benefit

One way to understand where the BLI benefit comes from is to consider power versus propulsive efficiency. The propulsive efficiency is defined as the ratio of net propulsive power to mechanical flow power,

$$\eta_{\mathrm{p}} = \frac{\text{power transmitted to the flow}}{\text{power needed}} = \frac{P_K - \phi_{\mathrm{jet}}}{P_{\mathrm{K}}}, \tag{3.8}$$

where ϕ_{jet} is the jet dissipation [9]. This definition of propulsive efficiency reduces to the conventional thrust-drag definition for the non-BLI case; $TV_\infty = P_{\mathrm{K}} - \phi_{\mathrm{jet}}$ [10] where T is the thrust,

$$\eta_{\mathrm{p,non\text{-}BLI}} = \frac{\text{thrust power transmitted to the flow}}{\text{net mechanical power to flow}} = \frac{TV_\infty}{\frac{\dot{m}}{2}.(V_{\mathrm{jet}}^2 - V_\infty^2)}. \tag{3.9}$$

In Equation (3.9), V_{jet} is the jet velocity, and V_∞ is the freestream wind tunnel velocity. Equation (3.8) shows that propulsive efficiency depends on the jet dissipation, ϕ_{jet}, which can be changed by varying the nozzle area. For a given net streamwise force, a propulsor with smaller nozzle area produces a larger jet velocity, hence more dissipation and lower propulsive efficiency. The different plugs used enable us to vary nozzle area and thus propulsive efficiency.

Two sources of benefit can be seen in the data for non-dimensional mechanical flow power versus propulsive efficiency. The mechanical flow power is non-dimensionalized by a reference power, P'_{K}, the power needed for the non-BLI case with plug 3. Figure 3-12 shows non-dimensionalized mechanical flow power, $\frac{P_{\mathrm{K}}}{P_{\mathrm{K}'}}$, versus propulsive efficiency, η_{p}, at 84 mph. The blue squares represent the non-BLI configuration. The data from plug 3 is the left blue square (smaller nozzle area, lower propulsive efficiency) and the data from plug 1 is the right blue square. The red circles represent the BLI configuration with plug 5 corresponding to the left circle, plug 3 the middle circle, and plug 1 the right circle. The error bars are also indicated.

These results can be interpreted using the 1D airframe-propulsion system analysis of Hall [10]. For the non-BLI configuration, this gives

$$\eta'_{\mathrm{p}} C_{P'_{\mathrm{K}}} = C'_{D_{\mathrm{airframe}}}, \tag{3.10}$$

where $C'_{D_{\mathrm{airframe}}}$ is the drag coefficient of the isolated non-BLI airframe. For the BLI configuration,

$$\eta_{\mathrm{p}} C_{P_{\mathrm{K}}} = C'_{D_{\mathrm{airframe}}} - f_{\mathrm{BLI}} C'_{\phi_{\mathrm{wake}}}, \tag{3.11}$$

where f_{BLI} is the percentage of fuselage boundary layer ingested by the propulsors and $f_{\mathrm{BLI}} C'_{\phi_{\mathrm{wake}}}$ represents the dissipation of the ingested wake at the propulsor inlet. Combining Equations (3.10) and (3.11), the ratio of BLI mechanical flow power to non-BLI mechanical flow power can be expressed as:

$$\frac{P_{\mathrm{K}}}{P'_{\mathrm{K}}} = \frac{\eta'_{\mathrm{p}}}{\eta_{\mathrm{p}}} \left(\frac{C'_{D_{\mathrm{airframe}}} - f_{\mathrm{BLI}} C'_{\phi_{\mathrm{wake}}}}{C'_{D_{\mathrm{airframe}}}} \right) \tag{3.12}$$

The blue dotted curve in Figure 3-12 is obtained using the drag coefficient, $C'_{D_{\mathrm{airframe}}}$, of the isolated non-BLI airframe ($f_{\mathrm{BLI}} = 0$), and varying the propulsive efficiency, in Equation (3.12). The same curve is plotted in Figure 3-12 for the BLI configuration as the red dashed curve. The ratio of mechanical flow power is lower for the BLI configuration because of the dissipation of the ingested wake. The vertical difference between the two dashed curves due to the reduced airframe dissipation accounts for 1% of the BLI Benefit. A more important source of the benefit is the propulsive efficiency difference between BLI at $\eta_\mathrm{p} = 0.82$ and non-BLI configuration at $\eta_\mathrm{p} = 0.76$ (plug 3 at 84 mph).

The aerodynamic BLI benefit can be written as $BLI\,Benefit = 1 - \frac{P_\mathrm{K}}{P'_\mathrm{K}}$, and there are two mechanisms that can reduce the mechanical flow power for the BLI configuration. The first is the increase in BLI propulsive efficiency (the term on the first right-hand side of Equation (3.12)), which is approximately 8% for the D8 model with plug 3 at 84 mph. This is the main benefit. The second mechanism is by decreasing the airframe dissipation, represented by the bracketed term in Equation (3.12), which accounts for 1% of the total benefit.

There is no unique way to assess the BLI benefit [5] and to do this in a realistic manner an overall aircraft system analysis must be carried out. One way to compare is at equal nozzle area (same nozzle plug)[4], for both configurations, which gives 7.9% benefit at 70 mph and 8.5% benefit at 84 mph (see Section 3.3.2). Another way is to compare the mechanical flow power at constant mass flow, plug 1 for the BLI configuration and plug 3 for the non-BLI configuration. The BLI benefit at these nozzle areas is 10.1% at 70 mph and 10.5% at 84 mph. Equal mass flow is also obtained with plug 3 for the BLI configuration and plug 5 for the non-BLI configuration with BLI benefit of 9.3% at 70 mph. It is not possible to compare the BLI benefit at equal mass flow at 84 mph because plug 5 was not tested on the non-BLI configuration at 84 mph. Appendix C shows the different conditions for the power sweeps during both entries at Langley.

In Figure 3-12, plugs 1 and 5 are not aligned with the red dashed curve for the BLI configuration although plug 1 is on the plot of non-dimensionalized shaft power, $\frac{P_\mathrm{S}}{P_{\mathrm{S}'}}$, versus propulsive efficiency of Figure 3-13. This is also the case for the non-BLI plug 1 point. The cause can come either from the fact that the operating points for

---

[4] TASOPT analysis shows that equal fan area is an approximate match for the BLI and non-BLI optimum cruise points

each plug is different leading to different fan efficiency or from the fact that there is phenomenon happening in the flow depending on the plug used.

Fan efficiency is the link between shaft power and mechanical flow power as in Equation (1.3) ($P_{\mathrm{K}} = \eta_{\mathrm{f}} P_{\mathrm{S}}$). Figure 3-14 shows fan efficiency versus flow coefficient. The top plot corresponds to the left propulsor and the bottom plot corresponds to the right propulsor. The black solid curve represents the measured cruise fan efficiency at 13500 RPM for the BLI configuration and the black dashed curve corresponds to the non-BLI configuration. The plug 1 flow coefficient is indicated by the green vertical line, the plug 3 flow coefficient is the blue vertical line, and the plug 5 flow coefficient is the red vertical line. Solid vertical lines represent BLI configuration data and dashed vertical lines represent non-BLI configuration data. For the non-BLI configuration, the fan efficiency with plug 1 is lower than the efficiency with plug 3. For the BLI configuration, the trend is different for the left and right propulsors. For the left propulsor, the fan efficiency with plug 1 is lower than with plug 5 which is lower than with plug 3 but for the right propulsor, the fan efficiency with plug 1 is larger than with plug 3 which is much larger than with plug 5. The right propulsor consumes more power so the power related to the right propulsor in the total power ($P_{\mathrm{K}} = P_{\mathrm{K,left}} + P_{\mathrm{K,right}} = \eta_{f,right} P_{\mathrm{S,right}} + \eta_{f,left} P_{\mathrm{S,left}}$) is dominant. This explains why plug 1 is below the blue dashed curve for the non-BLI configuration in Figure 3-12 and why plug 1 is above, and plug 5 below, the red dashed curve for the BLI configuration. In the actual installation, the fan could be designed such that the high efficiency is at the desired operating point. The flow field differences due to different plugs are described in Chapter 4.

The more BLI ingested the more aerodynamic benefit. This may explain why in Figure 3-12 the plug 5 red circle is below the red dashed curve, because the contours of stagnation pressure coefficient, in Section 4.2.2, indicate more severe stratified flow with plug 5 and more complicated flow for plug 1 decreasing the BLI benefit which could explain why plug 1 red circle was above the dashed curve.

A summary of electric, shaft, and mechanical flow power coefficients, flow coefficient, and propulsive efficiency is given in Table 3.1 and 3.2, BLI and non-BLI

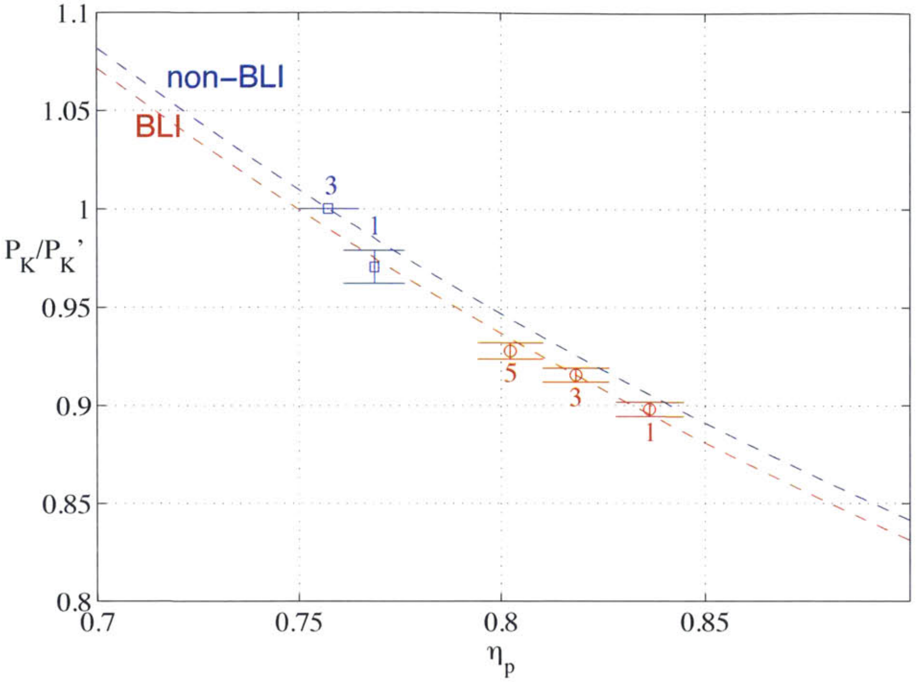

Figure 3-12: Non-dimensionalized mechanical flow power as a function of propulsive efficiency at 84 mph for BLI and non-BLI configurations, numbers refer to different area nozzle plugs

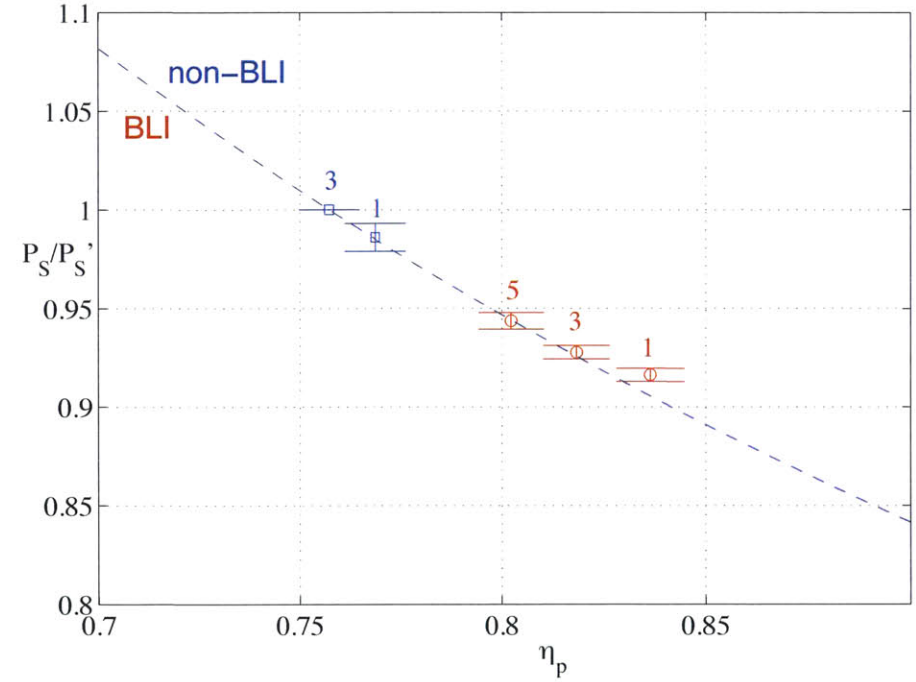

Figure 3-13: Non-dimensionalized shaft power as a function of propulsive efficiency at 84 mph for BLI and non-BLI configurations, numbers refer to different area nozzle plugs

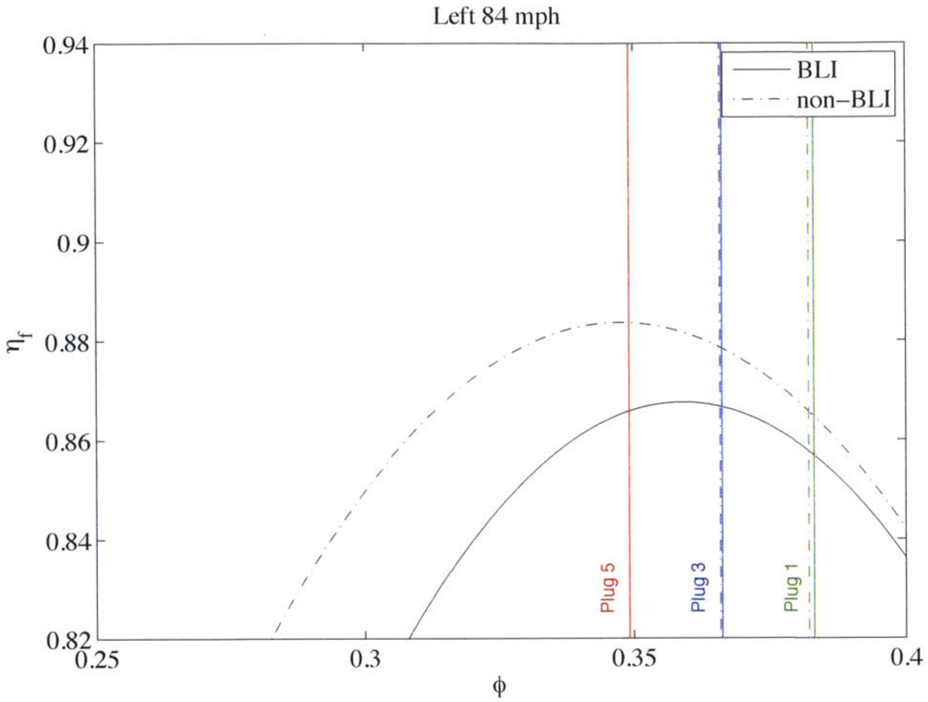

(a) Left motor

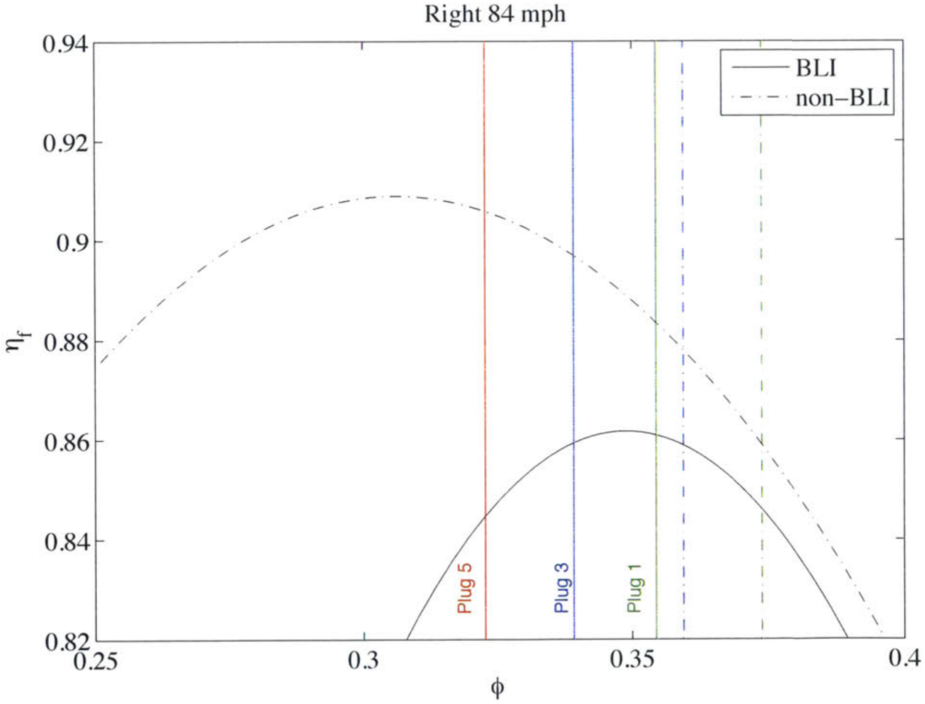

(b) Right motor

Figure 3-14: Fan efficiency against flow coefficient at 84 mph for both configurations and for a) the left propulsor and b) the right propulsor configurations, at simulated cruise conditions at 70 mph and 84 mph.

Table 3.1: Summary of electrical, shaft, and mechanical flow power coefficients and flow coefficient, and propulsive efficiency for BLI and non-BLI configurations at simulated cruise condition, 70 mph

	BLI			non-BLI		
	Plug 1	Plug 3	Plug 5	Plug 1	Plug 3	Plug 5
C_{P_E}	0.0672	0.0676	0.0686	0.0723	0.0730	0.0464
C_{P_S}	0.0529	0.0533	0.0539	0.0568	0.0573	0.0578
C_{P_K}	0.0449	0.0460	0.0464	0.0484	0.0499	0.0506
ϕ_L	0.3838	0.3702	0.3561	0.3784	0.3637	0.3386
ϕ_R	0.3569	0.3356	0.3025	0.3704	0.3541	0.3330
η_P	0.8387	0.8184	0.7969	0.7694	0.7573	0.7439

Table 3.2: Summary of electrical, shaft, and mechanical flow power coefficients and flow coefficient, and propulsive efficiency for BLI and non-BLI configurations at simulated cruise condition, 84 mph

	BLI			non-BLI		
	Plug 1	Plug 3	Plug 5	Plug 1	Plug 3	Plug 5
C_{P_E}	0.0635	0.0645	0.0656	0.0678	0.0690	N/A
C_{P_S}	0.0520	0.0526	0.0535	0.0559	0.0567	N/A
C_{P_K}	0.0446	0.0455	0.0461	0.0482	0.0497	N/A
ϕ_L	0.3842	0.3672	0.3502	0.3828	0.3668	N/A
ϕ_R	0.3555	0.3395	0.3223	0.3742	0.3600	N/A
η_P	0.8364	0.8183	0.8022	0.7686	0.7571	N/A

3.4 Boundary Layer Ingestion Benefit Uncertainty for the Indirect Method

As described in Chapter 2, the uncertainty can be computed by evaluating the repeatability of the data, and by using the experiment instrument uncertainties and propagating them. An uncertainty analysis from the Langley tests was performed by

Titchener and Hannon and a detailed analysis can be found in [18]. Some results are summarized below.

3.4.1 Statistical Approach for BLI benefit: Measurement Repeatability

The repeatability uncertainty in BLI benefit at equal mass flow is 0.8% at 70 mph and 0.4% at 84 mph within the 95% interval confidence, accounting only for the spread in the power coefficient measurement. There is also uncertainty in the definition of the cruise condition ($C_X = 0$). Including the later, the uncertainty in BLI benefit is 1.5% [18] at both 70 and 84 mph.

3.4.2 Propagation Approach for BLI Benefit: Instrument Uncertainty

The propagation chain for the BLI benefit is sketched in Figure 3-15. The items in red are the independent variables for which the uncertainties are known. The uncertainty in the electrical power comes from the manufacturer uncertainty of the power supply. The motor uncertainty was evaluated in Chapter 2, the uncertainty in the stagnation pressure difference is given by Siu [1], the Langley instrument uncertainty was assessed by Titchener and Hannon [18] as well as the uncertainty in qV, needed for the division by $qV_\infty = 0.5\rho_\infty V_\infty^3$ in the coefficient definition.

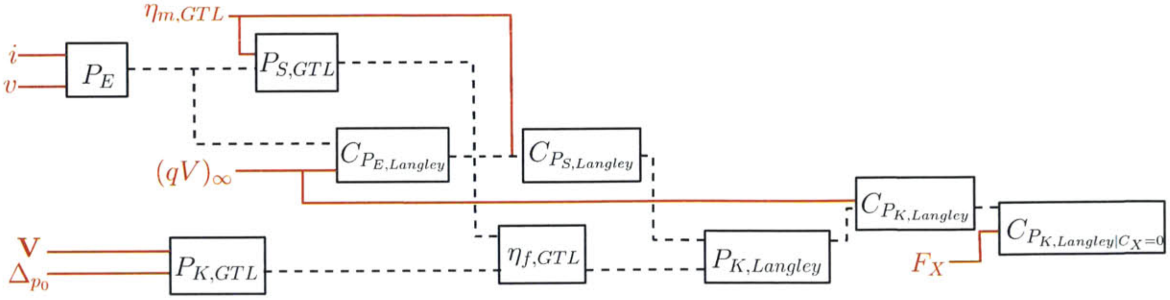

Figure 3-15: Uncertainty propagation for the mechanical flow power coefficient with the indirect measurement method

The independent variable uncertainties are listed in Table 3.3.

The uncertainty in BLI benefit can be found by combining the uncertainty in mechanical flow power coefficient for the non-BLI case and the BLI case. Reference [18] evaluates the uncertainty to be 1.85% at 70 mph and 1.7% at 84 mph. The instrument uncertainty is conservative, and the uncertainty in BLI benefit quoted in this thesis is the statistical uncertainty. Table 3.4 summarizes the results for the two methods of estimating the uncertainty in aerodynamic BLI benefit for the simulated cruise conditions at 70 and 84 mph.

Table 3.3: Independent variable uncertainty for BLI benefit

Variable	Instrument precision		%	
$P_{\mathrm{E}} = iv$	$0.012P_{\mathrm{E}}$		1.20%	
Δ_{p_0}	5 Pa		0.65%	
η_{m}	0.01		1.30%	
	70 mph	84 mph	70 mph	84 mph
$qV_\infty = 0.5\rho_\infty V_\infty^3$	144 kg/s^3	244 kg/s^3	0.81%	0.80%
	70 mph	84 mph	70 mph	84 mph
F_{X}	0.45 N	0.45 N	2.10%	1.50%

Table 3.4: Comparison between uncertainties from the statistical method and the propagation method on BLI benefit at 70 and 84 mph in %

Wind Tunnel speed	Statistical uncertainty	Propagation uncertainty
70 mph	±1.50	±1.85
84 mph	±1.50	±1.70

3.5 Summary

The aerodynamic BLI benefit was estimated to be around 8% at equal nozzle area and 10% at equal mass flow. The increase in propulsive efficiency for the BLI configuration was shown to be the main reason for the BLI benefit, with roughly 1% from the reduced airframe dissipation. The BLI benefit uncertainty is ±1.5% points. This low uncertainty is due to the excellent repeatability of the data from the NASA Langley 14x22-foot Subsonic Wind Tunnel over the two sets of experiments in 2013 and 2014.

Chapter 4

Five-Hole Probe Surveys

In Entry 1 (2013), stagnation and static pressure rakes were used for inflow and exit surveys. These rakes, however, could not be positioned close enough to the nacelle inlet, and exit to capture the ingested and jet streamtubes with the desired accuracy. A five-hole probe (FHP) mounted on a more accurate driver system was thus used for Entry 2 (2014). The FHP driver system is documented in [12]. This chapter describes the survey grids, the analysis of the FHP data, and shows the flowfields obtained through the FHP surveys.

4.1 Survey Methodology

Two FHPs were used for the surveys. The Aeroprobe drilled FHP was used to get data in front of the BLI propulsor. The Aeroprobe straight FHP was used at the rear of both the BLI, and the non-BLI propulsors. The survey grids, developed by van Dam [12], are explained briefly here, but a detailed description can be found in her thesis.

4.1.1 Survey Grids

Three different types of surveys were carried out: non-BLI exit, BLI exit, and BLI inlet. The inlet of the non-BLI configuration is assumed to be at uniform freestream conditions. The grids for each of these surveys, for all configurations with plug 3, are presented in Figure 4-1 as an example. Figure 4-1(a) shows the grid for the non-BLI exit. The surveyed points are denser near the stators and on both sides of the pylon, and the survey region extends radially outward past the trailing edge of the nacelle. Figure 4-1(b) shows the grid for the BLI exit. It is the same grid as for the non-BLI exit except it is rotated by 24.23° clockwise for the left propulsor and 22.85° counter-clockwise for the right propulsor to match the bifurcation location. Figure 4-1(c) shows the grid for the BLI inlet. The survey region for the BLI inlet is wider to capture the whole streamtube entering the propulsors, and the points are denser near the fuselage where the stagnation pressure is non-uniform.

Table 4.1 summarizes the number of points for each configuration with plug 3. The total number of points is different than the one obtained by multiplying the radial number of points, N_r, by the circumferential number of points, N_θ because near the bifurcation, the grid cannot be extended because of possible contact between the FHP and the airframe.

These surveys are taken 1.5 mm ($\approx$2% of the plug exit diameter) behind the nacelle trailing edge for the non-BLI configuration and 6 mm ($\approx$8% of the plug exit diameter) behind the nacelle trailing edge for the BLI exit configuration. For the inlet configuration, the FHP was 11 mm ($\approx$8% of the fan diameter) ahead of the nacelle leading edge. These distances were the closest between the FHP and a surface (plug or the nacelle leading edge and trailing edge) that the system permitted.

Figure 4-2 shows the streamlines through the propulsor of the non-BLI configuration on the top figure, and the BLI configuration on the bottom figure. The orange and yellow surfaces indicate the survey planes.

The probe could not reach all the desired points because of the limits in step

Table 4.1: Number of points for the survey grids for all configurations with plug 3

Configuration	N_r	N_θ	N_{tot}
BLI inlet	N/A	56	910
BLI exit	24	41	943
non-BLI exit	24	41	976

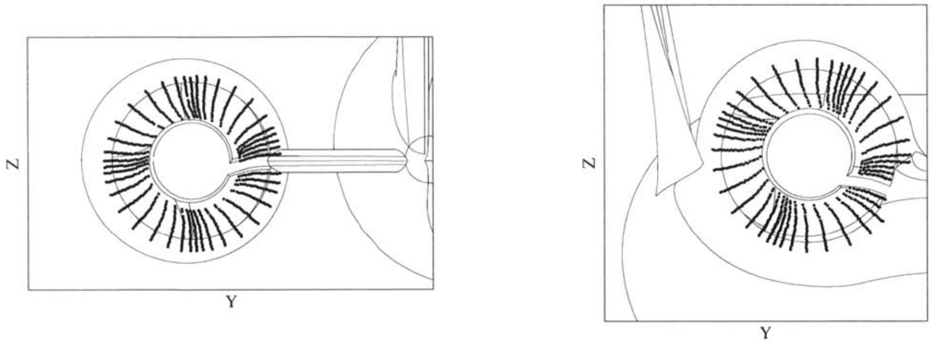

(a) Non-BLI exit

(b) BLI exit

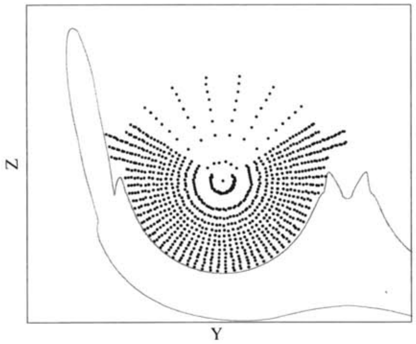

(c) BLI inlet

Figure 4-1: Survey grids for a) the non-BLI exit configuration, b) the BLI exit configuration with plug 3, and c) the BLI inlet configuration

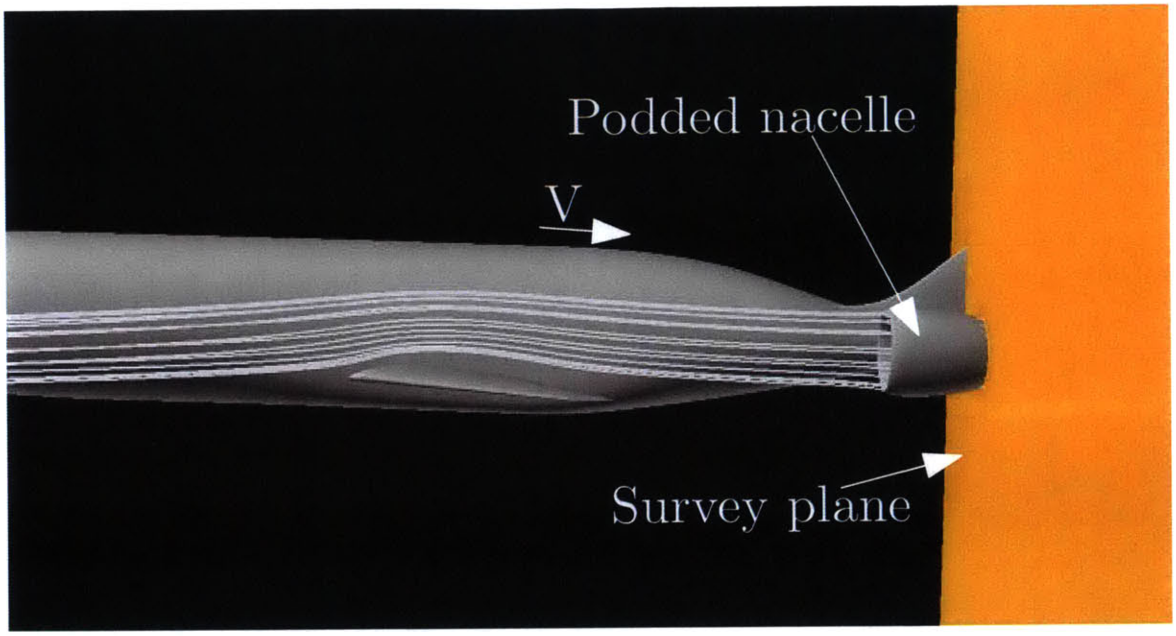

(a) Non-BLI exit

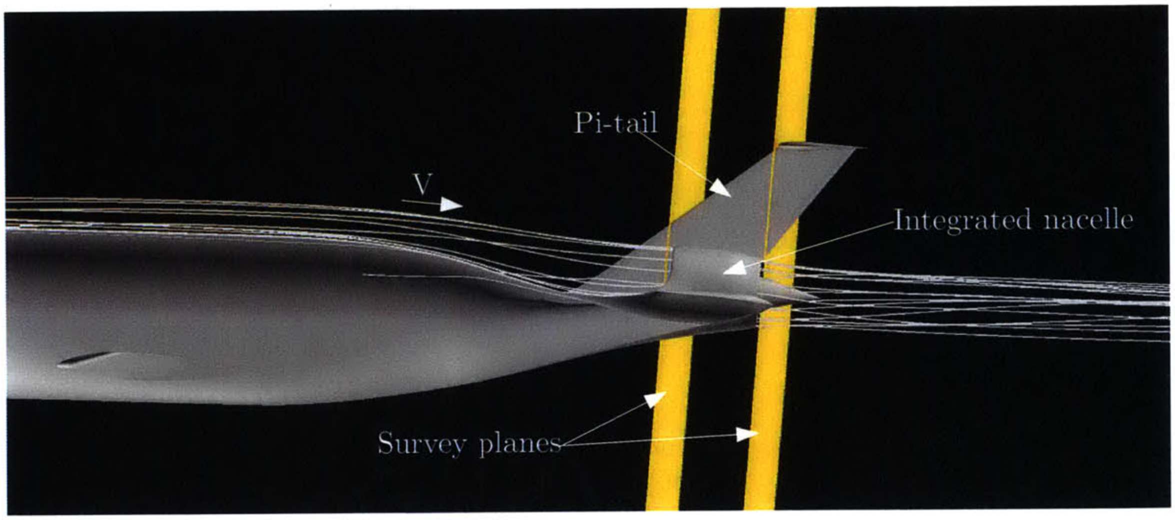

(b) BLI exit

Figure 4-2: Survey planes for a) the non-BLI exit configuration, and b) the BLI inlet and exit configurations. Flow goes to the right.
Credit: Jensen and Pandya, NASA Ames.

motor resolution. This is illustrated in Figure 4-3 where red dots represent the desired points and blue dots represent the points at which the data were taken.

4.1.2 Survey Probes

For the Langley exit surveys, the probe was the one used at MIT and described in Chapter 3. For the inlet survey, to get as close as possible to the propulsor inlet, a drilled FHP probe was used, as in Figure 4-4.

The probes were attached to a traverser system linked to the D8 model support. The traverser setup is detailed by van Dam [12].

4.1.3 FHP Calibration

The calibration of the straight FHP was carried out by Siu in the GTL 1x1 foot wind tunnel and is described in Appendix A of her thesis [1]. The calibration was done by varying pitch and yaw angles from -30° to 30° in increments of 2.5°, at different speeds of 42, 70, 100, and 200 mph. These speeds were chosen to cover the Langley wind tunnel speeds mentioned in Chapter 1. It is assumed that the calibration is adequate in non-uniform flow, and there is still on-going work to define possible correction for the calibration.

The drilled FHP was calibrated by Aeroprobe over angles between ±60° and speeds of 23, 45, and 88 mph. The same assumption is made.

4.1.4 Definition of Flow Angles

The pitch flow angle, α, is defined as the angle between the x-axis and the projection of the velocity vector in the x-z plane. The yaw flow angle, β, is the angle between the x-axis and the projection of the velocity vector in the x-y plane. The angles are indicated in Figure 4-5, which also illustrates the velocity and its components in the wind tunnel reference frame, and the FHP is also shown.

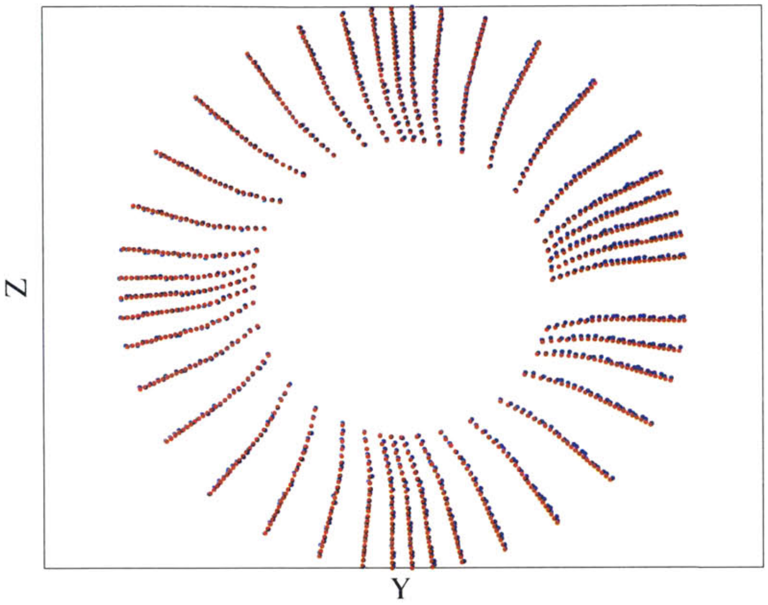

Figure 4-3: Comparison of the actual and desired coordinates for the survey grid

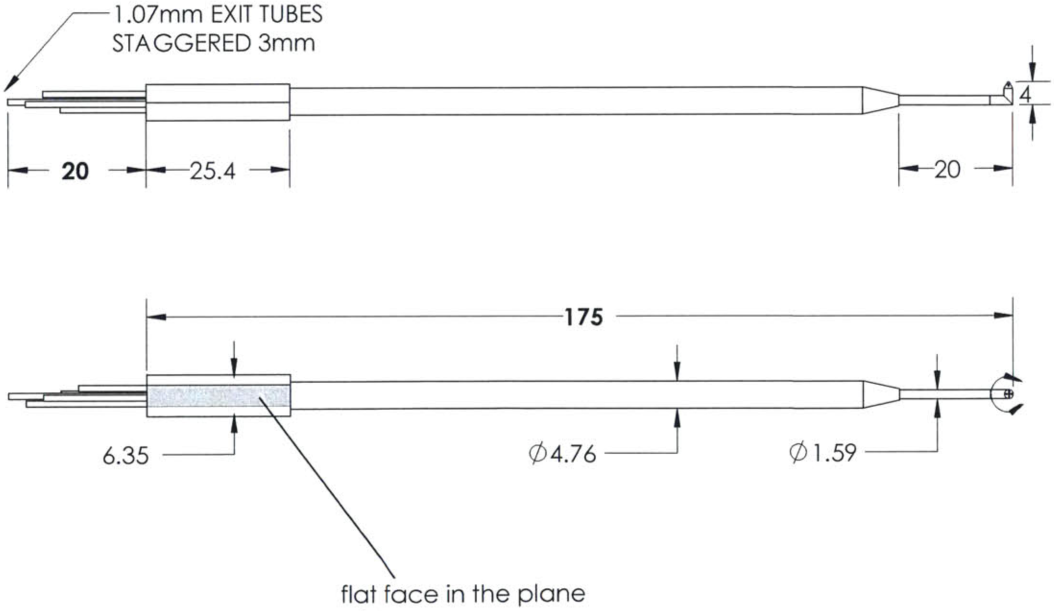

Figure 4-4: Drawings of drilled FHP for BLI inlet surveys. Units: mm.

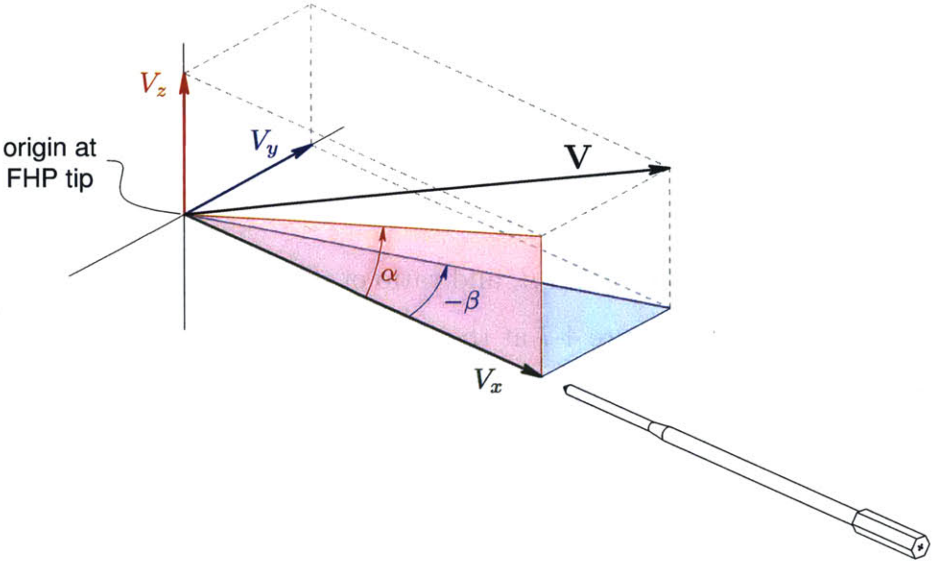

Figure 4-5: Angles and velocity convention.
Credit: Siu [1].

4.1.5 Survey Conditions

The conditions surveyed include both cruise and off-design flight conditions such as top of climb, start of climb, and descent. A number of conditions were surveyed with different nozzle plugs, wind tunnel speeds, angles of attack, and sideslip angles. The matrix of all the conditions surveyed is shown in Appendix D.

4.2 Flowfield Surveys

4.2.1 Cruise

Figure 4-6 shows the contour of stagnation pressure coefficient, $C_{p_0} = (p_0 - p_{0\infty})/q_\infty$, at the inlet and exit of the propulsors at 70 mph and 2° angle of attack at the simulated cruise condition for the BLI configuration with plug 3. It is a view from the back of the propulsors and the y-z projection of the shape of the fuselage in the survey plane is given as the black solid curves. The centers of the propulsors are marked with a black cross. The inlet survey is shown in the top figure where the dashed black circles indicate the fan face. The flow is stratified in stagnation pressure between the wall and the freestream, showing the boundary layer being ingested.

The exit survey is shown in the lower plot of Figure 4-6, where the nacelle and plug contours are given by dashed black circles. The jet is well-distinguished from the freestream, and there are regions of low stagnation pressure near the trailing edges of the four stators.

Contours of flow angles, α and β, and ratio of streamwise velocity to freestream velocity, $\frac{V_X}{V_\infty}$ are plotted in Figure 4-7 at the inlet and the exit of the propulsors of the BLI configuration with plug 3. The slope of the fuselage at the inlet survey location is 12° downwards and the yaw angle follows that direction. The pitch flow angles are asymmetric due to the divergent shape of the fuselage when getting closer to the nacelle trailing edge. The streamwise velocity reflects the velocity deficit of the ingested boundary layer.

The exit surveys show different features. The flow follows the plug local slope of 9°. Spurious angles appear due to the fact that the FHP cannot deal with non-uniform flow and are defined as angles bigger than 30° in absolute values, value considering too big to be present in this flow with this geometry. There are large flow angles in the shear layer; there are plotted with red diamonds in the alpha plot and with black diamonds in the beta plot. Regions of very low stagnation pressure appear behind the bottom stators probably because of the incoming distortion.

Figure 4-8 shows contours for the propulsor exit of the non-BLI configuration with plug 3. The flow follows the plug local slope of 6°[1]. The spurious flow angles appear in the shear layer between the jet and the freestream flow, and near the bifurcation.

---

[1] this slope is different from the one mentioned earlier because the exit surveys for the BLI or non-BLI propulsors were not carried out at the same plane

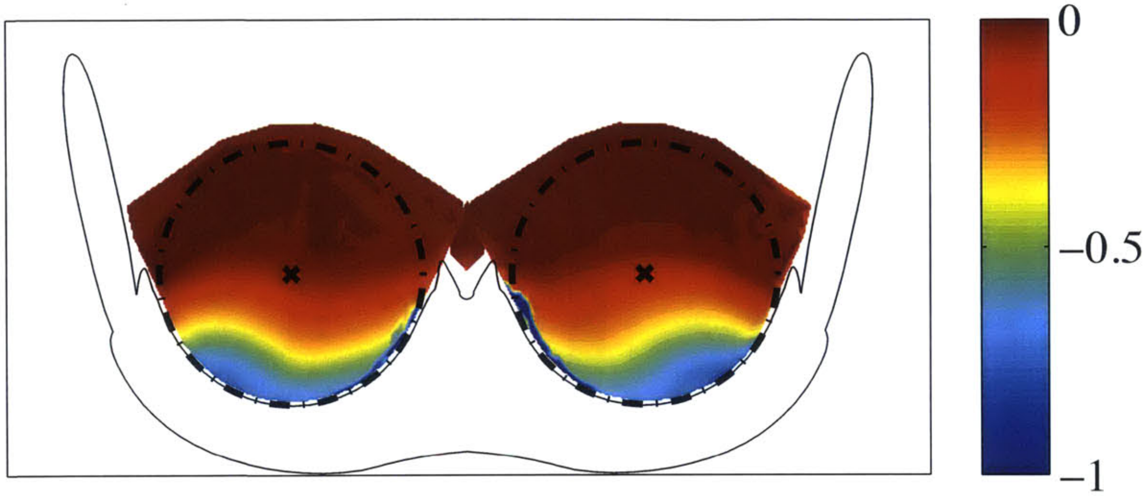

(a) Inlet

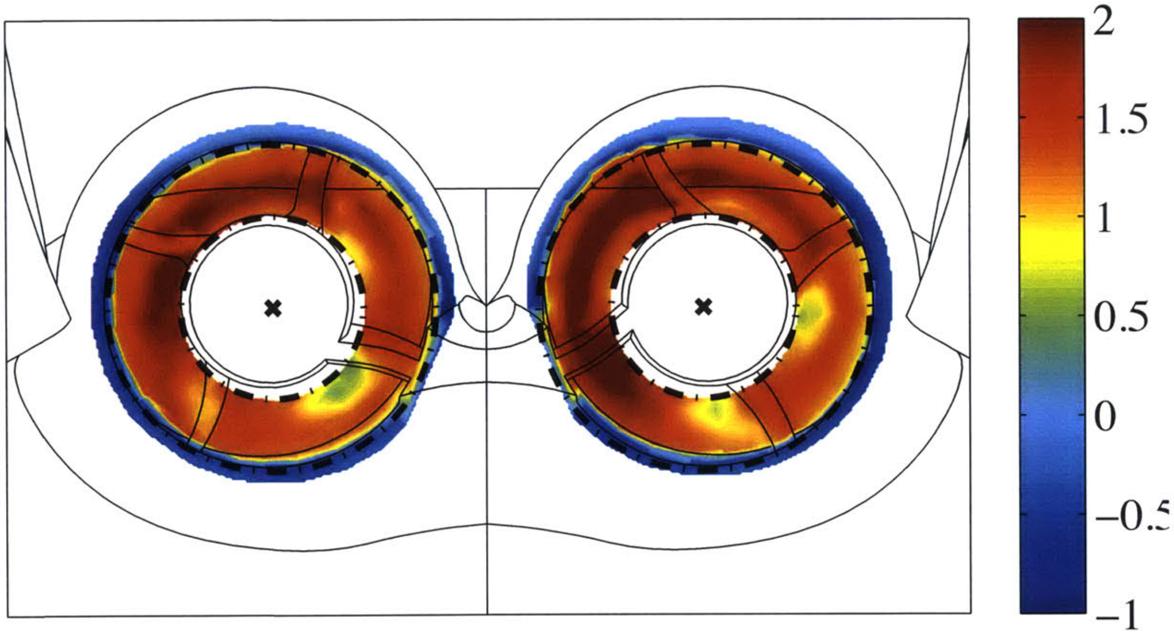

(b) Exit

Figure 4-6: Contours of stagnation pressure coefficient, C_{p_0}, for (a) the inlet and (b) the exit of the propulsor on the BLI configuration with plug 3 at cruise condition at 70 mph

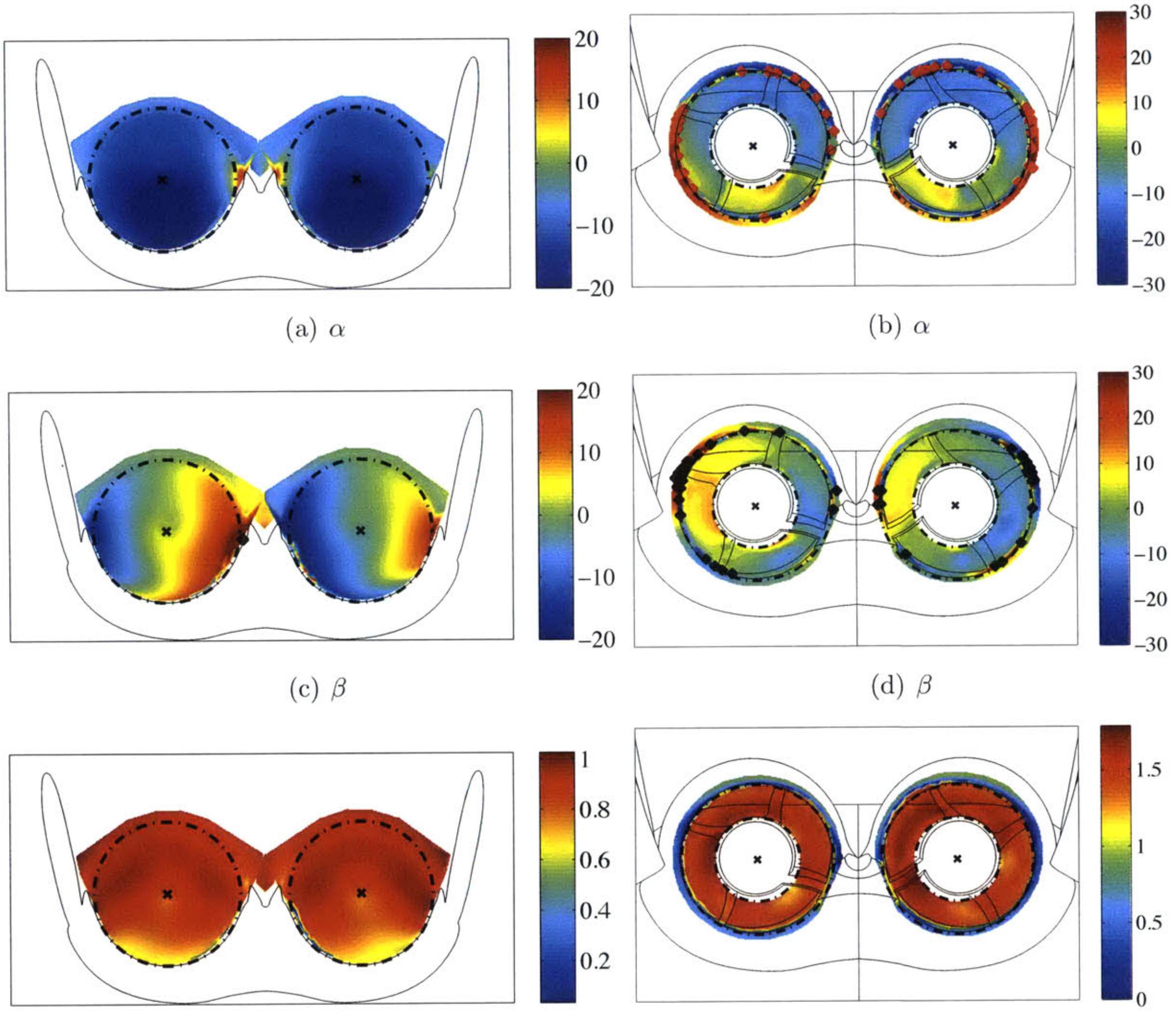

(a) α

(b) α

(c) β

(d) β

(e) $\frac{V_X}{V_\infty}$

(f) $\frac{V_X}{V_\infty}$

Figure 4-7: Contours of (a)-(b) pitch angle, (c)-(d) yaw angle, and (e)-(f) ratio of streamwise velocity to freestream velocity for the inlet (left plots) and exit (right plots) of the propulsors on the BLI configuration with plug 3 at cruise condition at 70 mph

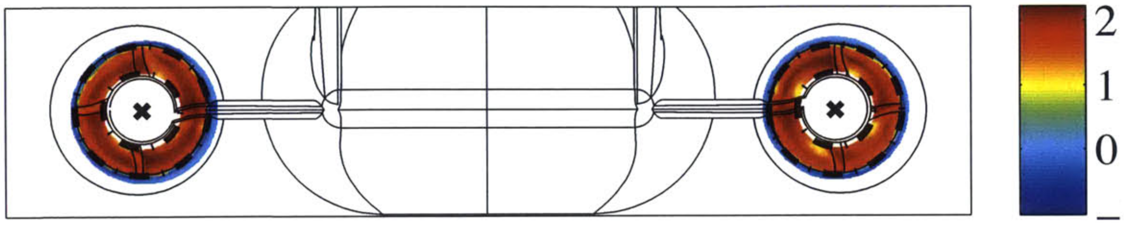

(a) C_{p_0}

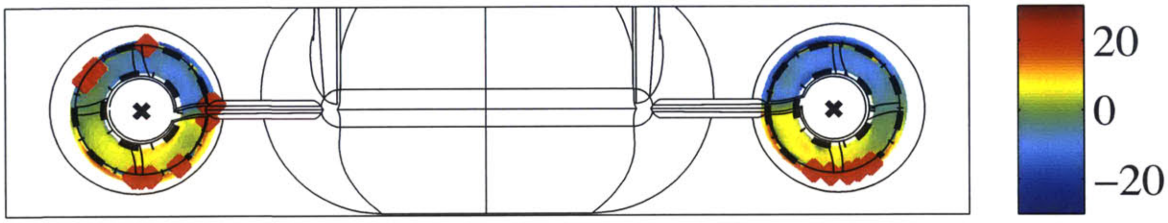

(b) α

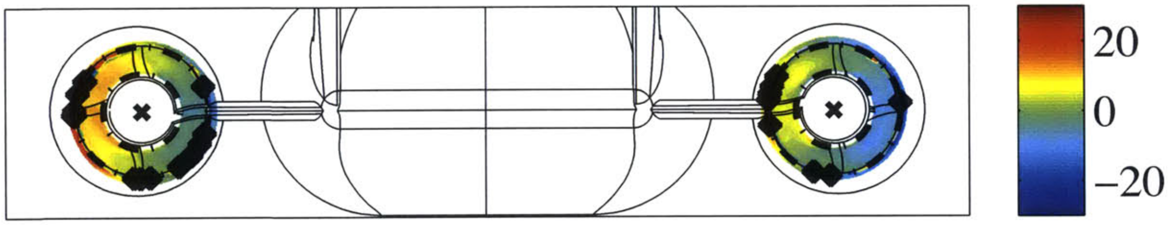

(c) β

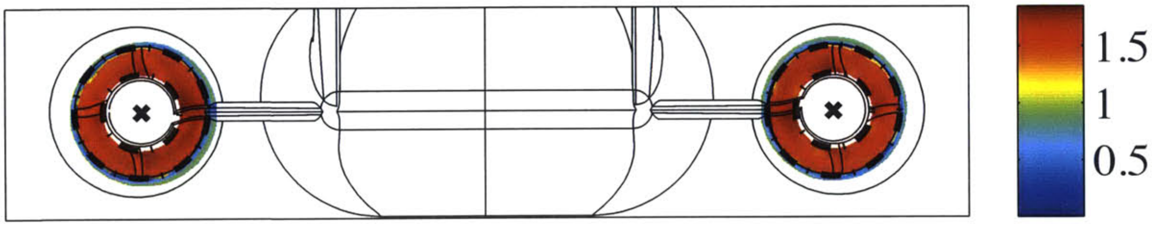

(d) $\frac{V_\text{X}}{V_\infty}$

Figure 4-8: Contours of (a) stagnation pressure coefficient, (b) pitch angle, (c) yaw angle, and (d) ratio of streamwise velocity to freestream velocity at the propulsor exit for the non-BLI configuration with plug 3 at cruise condition at 70 mph

4.2.2 Comparison of Flowfield for Different Plugs at 84 mph

Figure 4-9 shows contours of stagnation pressure coefficient at the propulsor inlet (left figures) and exit (right figures) for the BLI configuration at the cruise conditions at 84 mph and for plug 1, 3, and 5. The pitch angle, yaw angle, and ratio of streamwise velocity to freestream velocity are given in Figure 4-10, 4-11, and 4-12. The stratification of the boundary layer increases with the larger nozzle plug (smaller nozzle area) because of a lower mass flow. The FHP reads more spurious flow angles for plug 1 than plug 3 or plug 5.

Figure 4-13 shows contours of stagnation pressure coefficient, pitch angle, yaw angle, and ratio of streamwise velocity to freestream velocity at the propulsor exit for the non-BLI configuration for the cruise conditions at 84 mph and for plug 3. There is a good behavior overall.

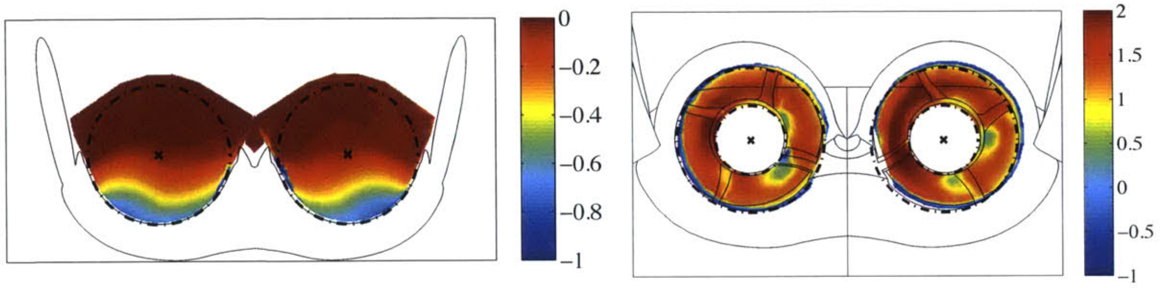

(a) BLI inlet plug 1

(b) BLI exit plug 1

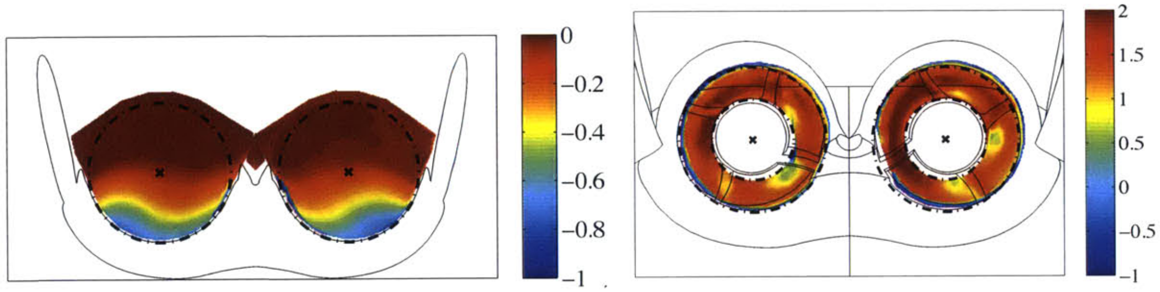

(c) BLI inlet plug 3

(d) BLI exit plug 3

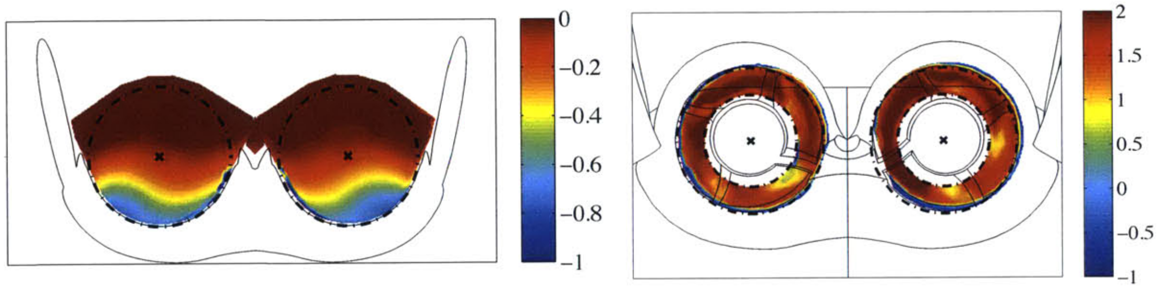

(e) BLI inlet plug 5

(f) BLI exit plug 5

Figure 4-9: Contours of stagnation pressure coefficient for BLI inlet (left figures) and BLI exit (right figures) with (a)-(b) plug 1, (c)-(d) plug 3, and (e)-(f) plug 5 at cruise condition at 84 mph

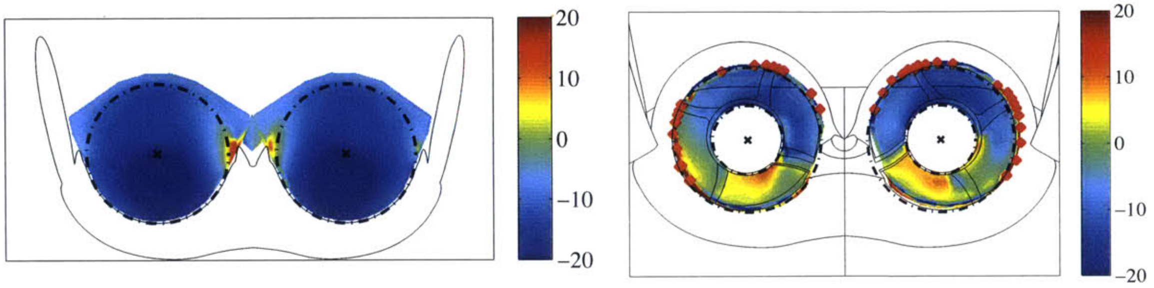

(a) BLI inlet plug 1 (b) BLI exit plug 1

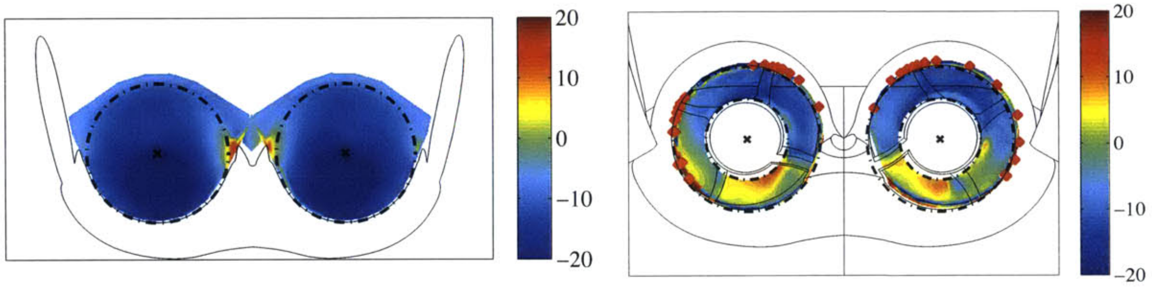

(c) BLI inlet plug 3 (d) BLI exit plug 3

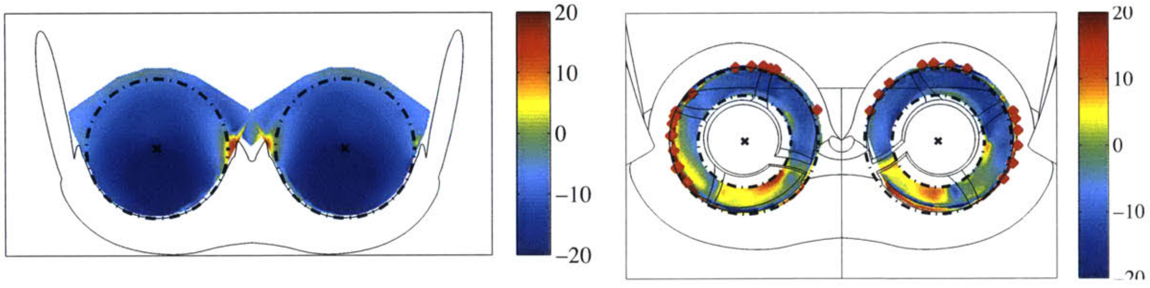

(e) BLI inlet plug 5 (f) BLI exit plug 5

Figure 4-10: Contours of pitch angle for BLI inlet (left figures) and BLI exit (right figures) with (a)-(b) plug 1, (c)-(d) plug 3, and (e)-(f) plug 5 at cruise condition at 84 mph

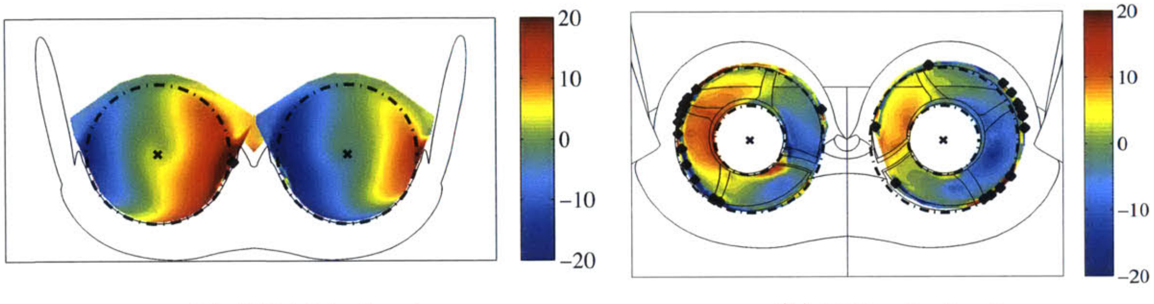

(a) BLI inlet plug 1 (b) BLI exit plug 1

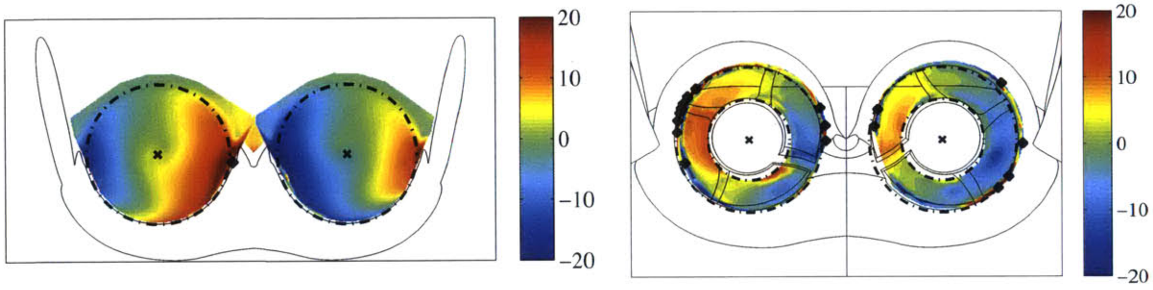

(c) BLI inlet plug 3 (d) BLI exit plug 3

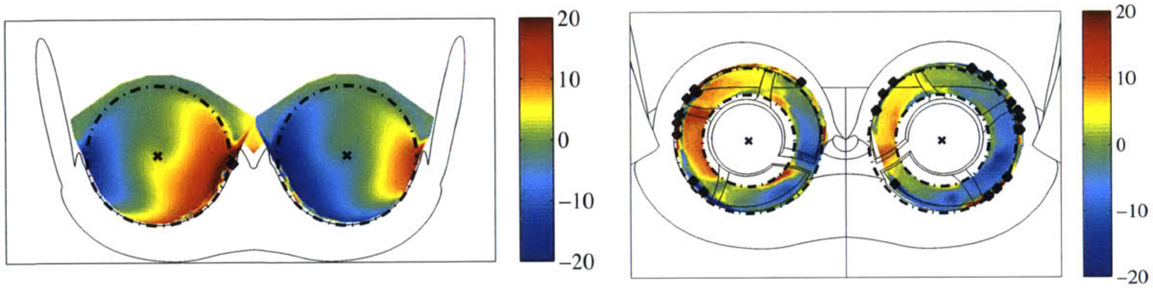

(e) BLI inlet plug 5 (f) BLI exit plug 5

Figure 4-11: Contours of yaw angle coefficient for BLI inlet (left figures) and BLI exit (right figures) with (a)-(b) plug 1, (c)-(d) plug 3, and (e)-(f) plug 5 at cruise condition at 84 mph

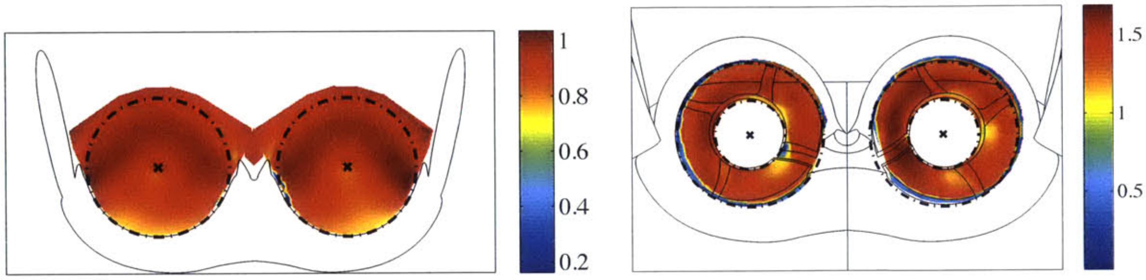

(a) BLI inlet plug 1

(b) BLI exit plug 1

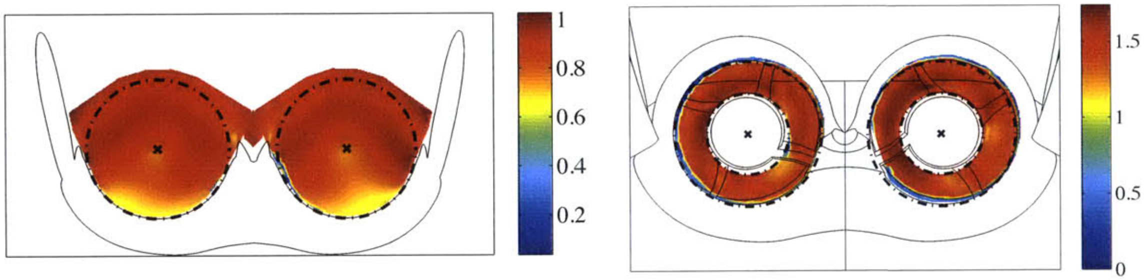

(c) BLI inlet plug 3

(d) BLI exit plug 3

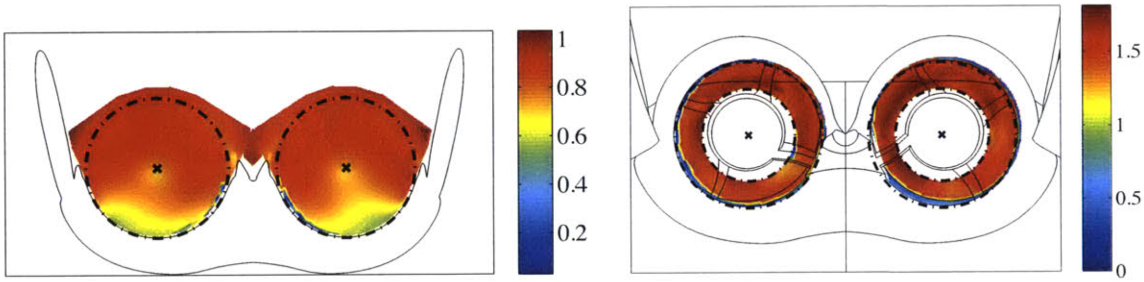

(e) BLI inlet plug 5

(f) BLI exit plug 5

Figure 4-12: Contours of ratio of streamwise velocity to freestream velocity for BLI inlet (left figures) and BLI exit (right figures) with (a)-(b) plug 1, (c)-(d) plug 3, and (e)-(f) plug 5 at cruise condition at 84 mph

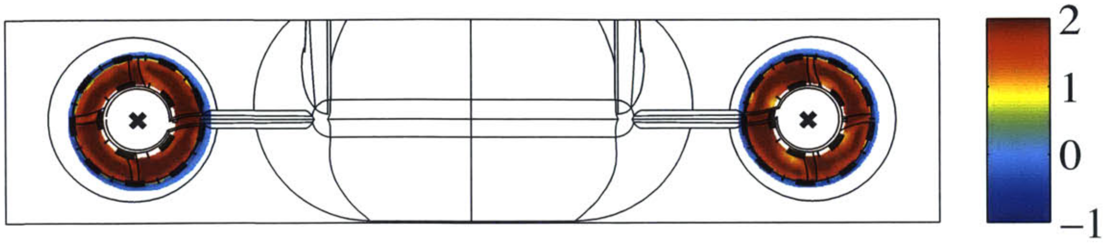

(a) C_{p_0}

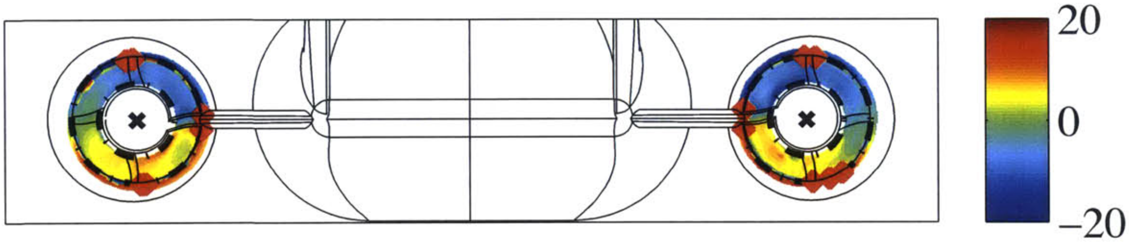

(b) α

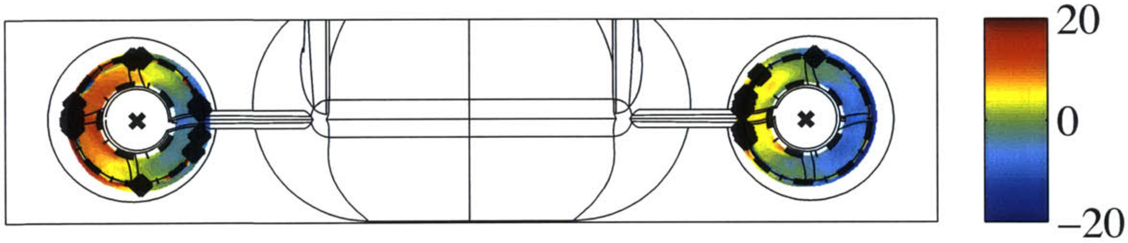

(c) β

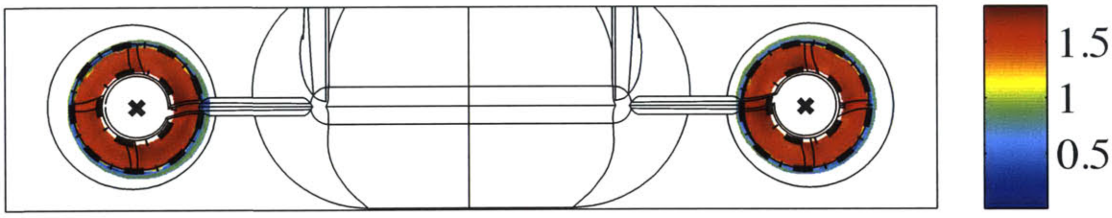

(d) $\frac{V_x}{V_\infty}$

Figure 4-13: Contours of (a) stagnation pressure coefficient, (b) pitch angle, (c) yaw angle, and (d) ratio of streamwise velocity to freestream velocity for the propulsor exit for the non-BLI configuration with plug 3 at cruise condition at 84 mph

4.2.3 Off-Design

Several off-design conditions were performed and are indicated in the pressure survey matrix of Appendix D. The propulsor inlet flowfields for the following conditions are given in Figures 4-14:

- Start-of-climb: 8°, $\frac{U_{\text{tip}}}{V_\infty} = 5.6$ (42 mph, 14 000 RPM)
- Top-of-climb: 2°, $\frac{U_{\text{tip}}}{V_\infty} = 3.4$ (70 mph, 13 500 RPM)
- Descent: 8°, $\frac{U_{\text{tip}}}{V_\infty} = 1.3$ (70 mph, 5250 RPM)

At the start-of-climb condition, shown in Figure 4-14(a), the angle of attack is high and the RPM is high. Vortices appear near the fuselage and the FHP cannot capture the shear layer at the top half (white region). At the top-of-climb condition, shown in Figure 4-14(b), the flow is well-behaved and stratified and is quantitatively similar to the cruise inflow (the only difference is the higher power level at top of climb). The descent condition, shown in Figure 4-14(c), is the most severe since the angle of attack is high and the propulsors are at low power, thus resulting in a thicker boundary layer over the fuselage. Vortices can be seen near the vertical tails and the nacelle.

4.3 Summary

The flowfields obtained via FHP surveys were presented in this Chapter. FHP surveys enable to have information on the ingested distorted flow. All the contour plots show that the flow behaves well for numerous conditions, including off-design conditions. Bigger distortion is introduced with smaller nozzle area. Off-design plots show that vortices appear but there are no showstoppers for the model.

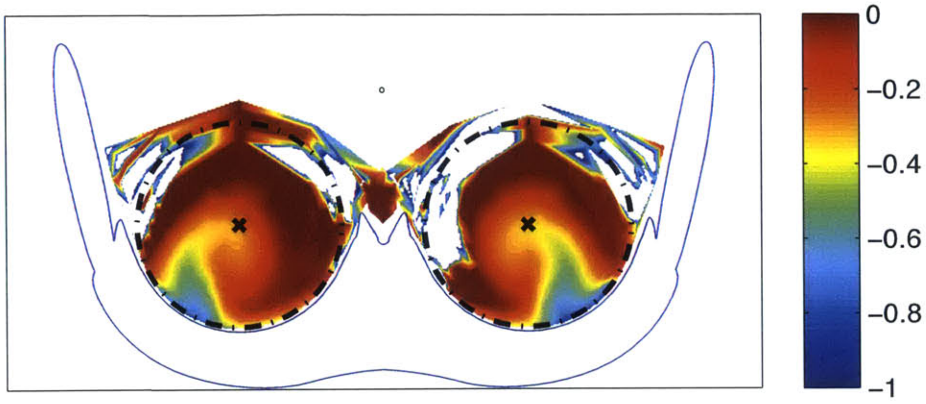

(a) Start-of-climb

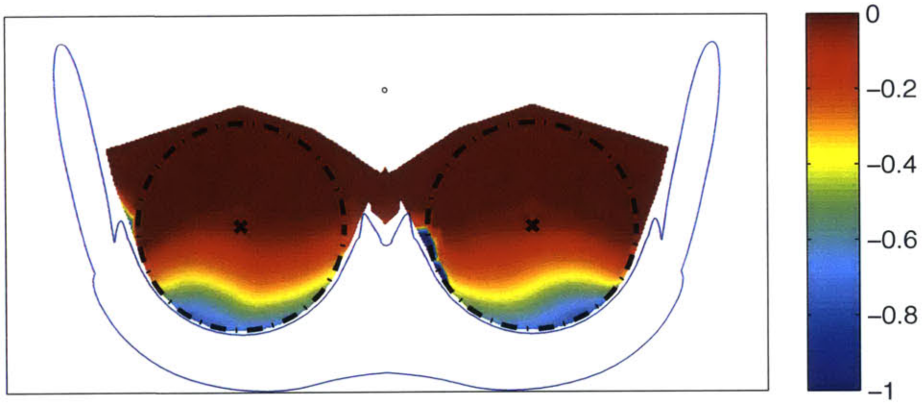

(b) Top-of-climb

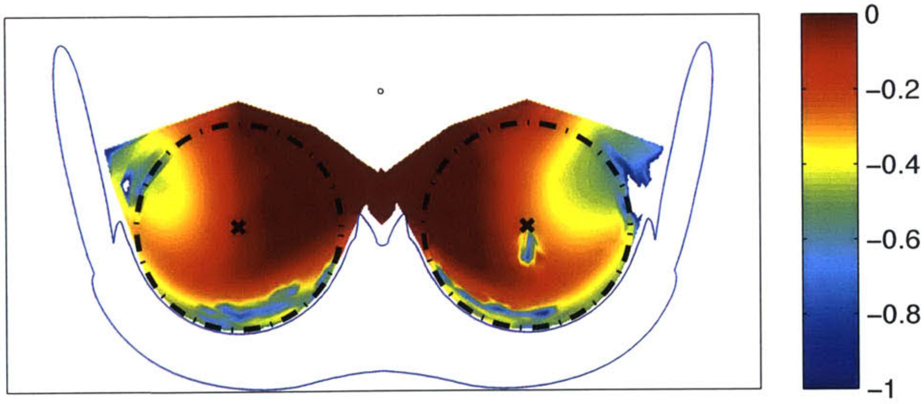

(c) Descent

Figure 4-14: Contous of stagnation pressure coefficient at the propulsor inlet for the BLI configuration at (a) start-of-climb, (b) top-of-climb, and (c) descent with plug 3

Chapter 5

Measurement of BLI Benefit II: Direct Method

In this chapter, the definition of mechanical flow power in Equation (1.4),

$$P_{\mathrm{K}} = \oiint (p_{0\infty} - p_0)\mathbf{V} \cdot \hat{n} dS,$$

and the FHP surveys (Chapter 4) are used to compute the BLI benefit. There are two steps to obtain the mass flow and mechanical flow power integrals over the propulsor. The first is conceptual: to define the integration region. The second is implementation: to perform the numerical integration. A sensitivity analysis on the integration grid was also carried out and is described.

5.1 Area of Integration

The survey grids described in Chapter 4 were designed to cover a larger area than the flow passing through the propulsors. Equation (1.4) indicates the integration is over the propulsor to give the power added to the flow. In this, the determination of the edges of streamtube passing through the propulsors is needed, and a new integration grid is built. For the exit surveys, the boundary of the streamtube is found from the stagnation pressure, as described below. At the inlet, CFD is used to define the entering streamtube.

5.1.1 Inlet Surveys

In Chapter 4, it was stated that the inlet region survey was extended past the nacelle radius to be sure the entering streamtube was captured. The surveys alone are not enough to determine the boundaries of the streamtube that enters the propulsors, and the CFD simulations enable us to track particles and to determine the contour of the streamlines entering the propulsor. The CFD simulations were performed under the lead of Shishir Pandya, NASA Ames, as part of the N+3 Phase 2 work.

Figure 5-1 illustrates the streamlines across the right BLI propulsor with plug 1 at 70 mph. The streamtube's cross-section changes as the propulsor is approached so the location of the survey plane is important. Figure 5-2(a) shows the contour of streamlines at the survey plane obtained from a spline interpolation of the CFD points. As indicated in Chapter 1, the CFD simulations have only been carried out for 70 mph for the right half of the airframe with plug 1, and it is assumed here that the contour of streamlines is the same at 70 and 84 mph, and does not depend on the plug[1]. Because CFD was run only with plug 1 and Langley surveys were made to compute BLI benefit with plug 3, all the CFD data shown is with plug 1 and all the Langley data shown is with plug 3.

Once the contour is determined, an integration grid is defined and the number of radial, N_r, and circumferential points, N_θ, chosen. The only constraint for the BLI inlet integration grid is the outer boundary defined by the streamline contour. A uniform integration grid with approximately the same number of points as the survey grid was used; a sensitivity analysis of the number of points is given in Section 5.3. Figure 5-2(b) compares the survey grid, represented by red crosses, and the integration grid, represented by black circles, for the right BLI inlet. The integration grid is defined with $N_r N_\theta$ cells, and midpoints at the center of the cells. A mirror transformation was applied to obtain the left side.

---

[1] A different plug means a different mass flow but surveys at Langley were done with plug 3.As an approximation, the CFD inlet streamtube with plug 1 is used.

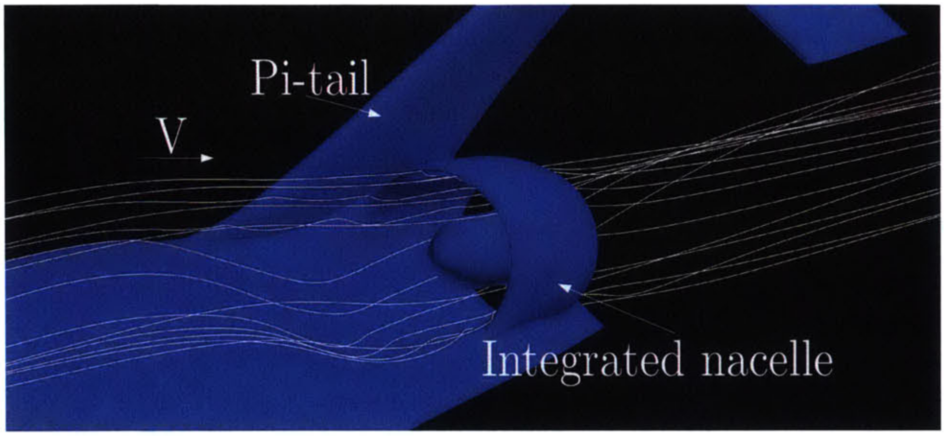

(a) Side view

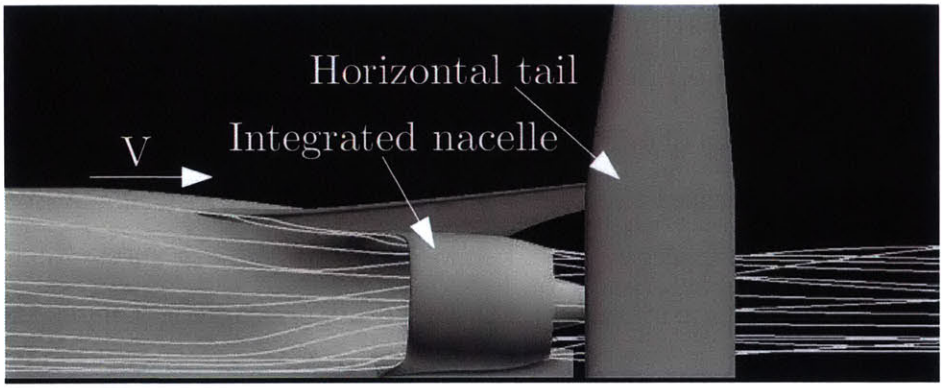

(b) Top view

Figure 5-1: (a) Side view, and (b) top view of streamlines across the right propulsor from numerical simulations, at 70 mph, BLI configuration, plug 1, 2° angle of attack, $C_X = 0$. Credit: Jensen and Pandya, NASA Ames.

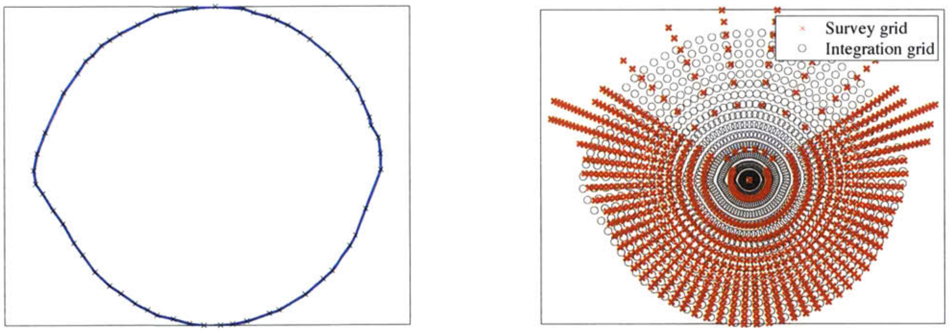

(a) Contour of streamlines

(b) Integration grid

Figure 5-2: (a) Edge of streamtube through the right propulsor, and (b) survey (red crosses) and integration (black circles) grids of the right propulsor at 70 mph for the BLI inlet

5.1.2 Exit Surveys

Figure 5-3 shows streamlines across the right non-BLI propulsor with plug 1, at 70 mph, obtained from the CFD. For the exit surveys, the streamline contour was found from the data with stagnation pressure coefficient larger than a specified value, $C_{p_0} > C_{p_{0,\mathrm{lim}}}$, consistent with the MIT experiments (see Appendix A). For the Langley tests, the specified value was fixed at $C_{p_{0,\mathrm{lim}}} = 0.01$. Analysis of $C_{p_{0,\mathrm{lim}}}$ indicated that 0.01 was the value that excludes all freestream points. A variation of ± 0.005 did not change the results. This method was used rather than obtaining the exit contours from CFD because the FHP traverser mounting had variations from run to run at Langley so it would be difficult to superimpose the CFD contour and the survey grid accurately. Figure 5-4(a) shows the contour of streamlines at the survey plane for the BLI exit (left figure) and the non-BLI exit (right figure) with plug 3 at 70 mph[2]. Figure 5-4(b) shows the integration and survey grids for the exit survey plane for the BLI configuration (left figure) and the non-BLI configuration (right figure) with plug 3 at 70 mph.

The outer boundary is given by the stagnation pressure coefficient specified value of 0.01. The inner boundary is set by the plug diameter at the survey plane. The integration grid used is the desired grid shown in Chapter 4 modified with the above constraints. The sensitivity analysis (Section 5.3) shows that the integration grid is suitable.

5.2 Integration

Raw quantities are interpolated from the survey grid to the integration grid using a linear interpolation. The integration is carried out in the survey plane, located in the propulsor reference frame. At each cell, cell mass flow, $\dot{m}_{\mathrm{i}}$, cell mechanical flow power coefficient, $C_{\tilde{P}_{\mathrm{K,i}}}$, cell stagnation and static pressure coefficients, $C_{p_{\mathrm{t,i}}}$ and $C_{p_{\mathrm{s,i}}}$, can be found. Mass flow and mechanical flow power coefficient are evaluated by

---

[2] All the Langley results are shown with plug 3: it is the only plug with which surveys were taken for the direct evaluation of the BLI benefit (See Appendix C). Comparison of the flow field with different plugs was given in Section 4.2.2.

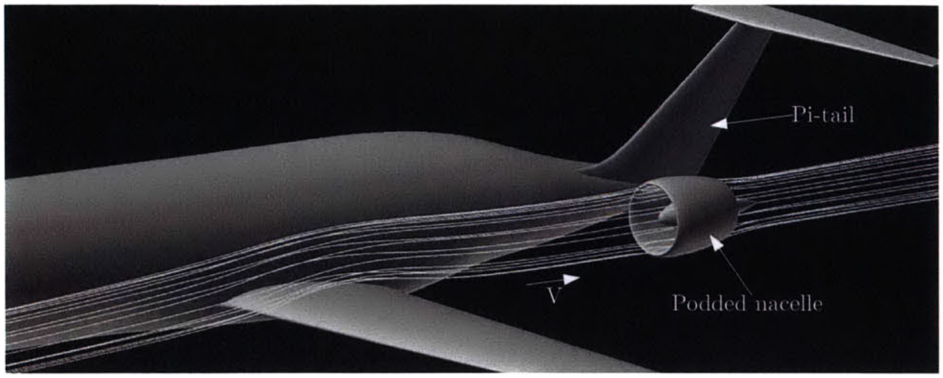

Figure 5-3: Side view of streamlines across the left propulsor from numerical simulations, at 70 mph, non-BLI configuration, plug 1, 2° angle of attack, $C_X = 0$. Credit: Jensen and Pandya, NASA Ames.

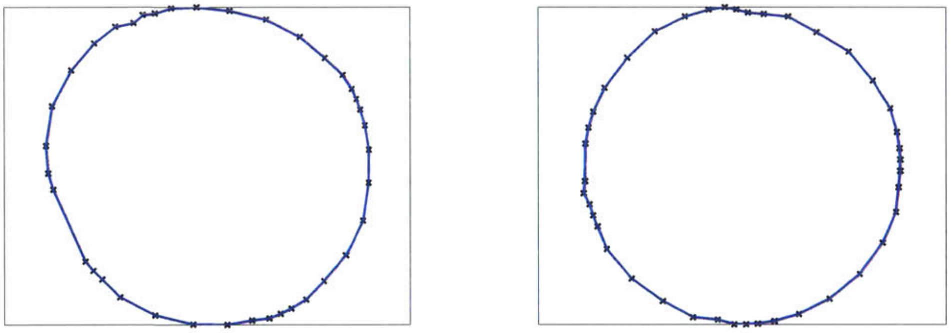

(a) BLI streamtube

(b) non-BLI streamtube

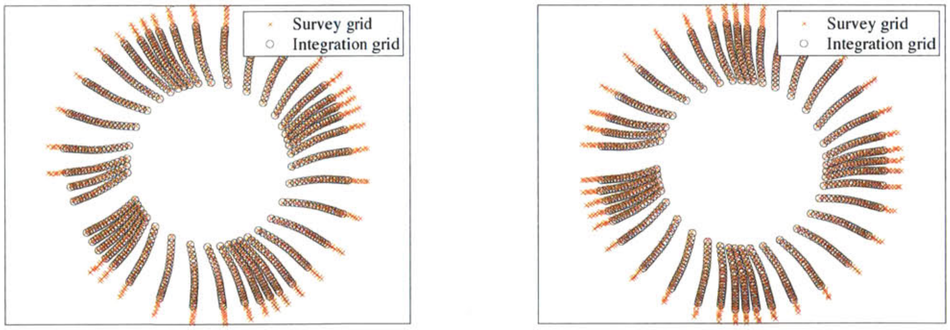

(c) BLI grids

(d) non-BLI grids

Figure 5-4: Edge of exit streamtube, and exit survey (red crosses) and integration (black circles) grids for the right propulsor at 70 mph for (a)-(c) the BLI, and (b)-(d) the non-BLI configurations summing quantities over the cells. The quantities are given in terms of volume flux as in Equation (5.1) where ξ represents the variable of integration. The double integral is discretized using mid-point integration, as in the right-hand term in Equation (5.1).

$$\Xi = \oiint \xi \mathbf{V} \cdot \hat{n} dS = \sum_{CV surfaces} \xi_{\mathrm{i}} V_{x\mathrm{i}} S_{\mathrm{i}} \tag{5.1}$$

5.3 Sensitivity Analysis

Analysis of the sensitivity of the results to the number of radial and circumferential points was done to assess the integration grid. Table 5.1 summarizes the different integration grids examined and gives the survey grid number of points for comparison. For the survey grid, the approximation symbol refers to the fact that the survey grid changed (by ±5 grid points) at Langley because of day-to-day alignment issues so the mean number of grid points is given.

Figure 5-5 shows the measured mechanical flow power at the survey plane, $C_{\tilde{P}_{\mathrm{K}}}$, and the non-dimensionalized mass flow, $\dot{m}/\rho_\infty V_\infty A_{\mathrm{fan}}$, for the right propulsor of the BLI inlet, BLI exit, and non-BLI exit with plug 3, as a function of the number of total points ($N_{tot} = N_r N_\theta$) for the corresponding integration grid. The different symbols correspond to the different integration grids. The dashed lines indicate the region of ±0.5% of the value obtained with the finest grid $(2N_{r,ref}, 2N_{\theta,ref})$. The red vertical line indicates the number of points of the survey grid. For all configurations in Figure 5-5, the cyan cross represents the integration grid which is closest in number of points to the survey grid, and which was shown in Figures 5-2 and 5-4. The cross is always within the 0.5% interval. The results show a denser grid is not needed, and the integration grid thus uses $(N_{r,ref}, N_{\theta,ref})$ points (Table 5.1).

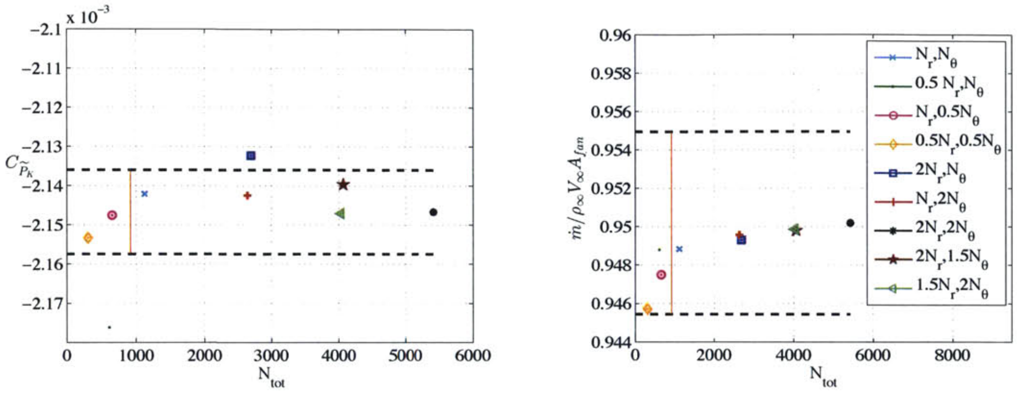

(a) $C_{\widetilde{P}_K}$ at right BLI inlet

(b) $\dot{m}/\rho_\infty V_\infty A_{\text{fan}}$ through right BLI inlet

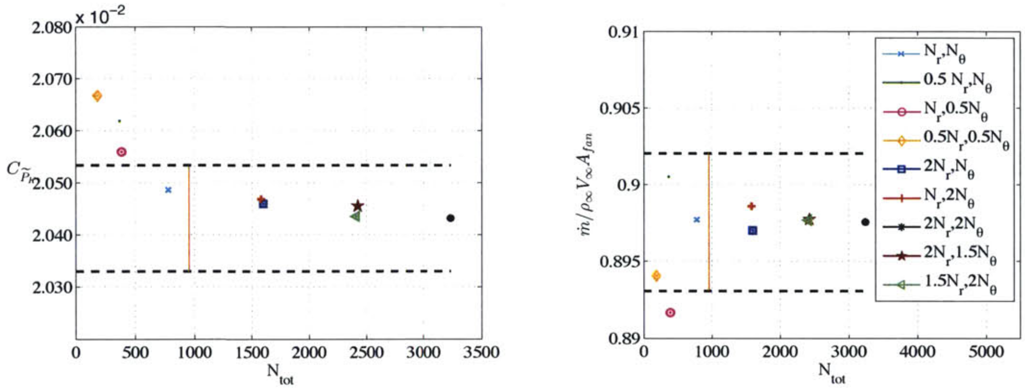

(c) $C_{\widetilde{P}_K}$ at right BLI exit

(d) $\dot{m}/\rho_\infty V_\infty A_{\text{fan}}$ through right BLI exit

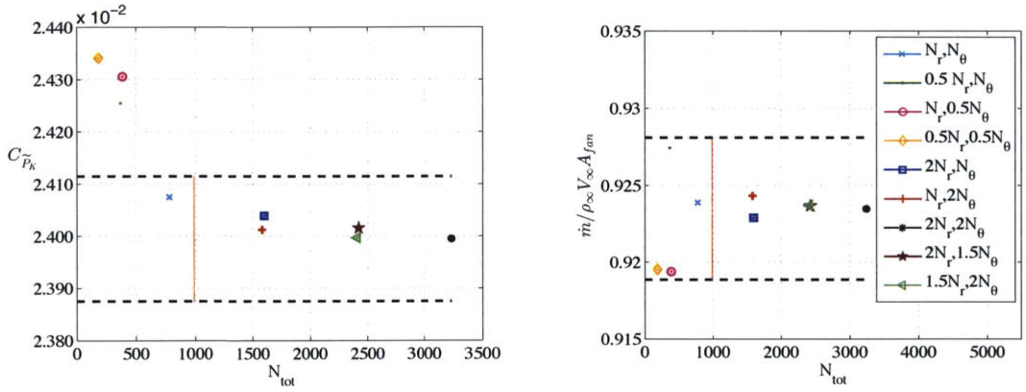

(e) $C_{\widetilde{P}_K}$ at right non-BLI exit

(f) $\dot{m}/\rho_\infty V_\infty A_{\text{fan}}$ through right non-BLI exit

Figure 5-5: Mechanical flow power coefficient and non-dimensionalized mass flow versus number of points of the integration grid for the right (a)-(b) BLI inlet, (c)-(d) BLI exit, and (e)-(f) non-BLI exit at 70 mph

Table 5.1: Number of radial, circumferential, and total points for the different integration grids

	BLI inlet			BLI exit			non-BLI inlet		
	N_r	N_θ	N_{tot}	N_r	N_θ	N_{tot}	N_r	N_θ	N_{tot}
Survey grid	-	-	910	-	-	≈945	-	-	≈980
Integration grid $(N_{r,ref}, N_{\theta,ref})$	15	75	1125	19	41	779	19	41	779
Integration grid $(\frac{1}{2}N_{r,ref}, N_{\theta,ref})$	7	75	525	9	41	369	9	41	369
Integration grid $(N_{r,ref}, \frac{1}{2}N_{\theta,ref})$	15	37	555	19	20	380	19	20	380
Integration grid $(\frac{1}{2}N_{r,ref}, \frac{1}{2}N_{\theta,ref})$	7	37	259	9	20	180	9	20	180
Integration grid $(2N_{r,ref}, N_{\theta,ref})$	31	75	2325	39	41	1599	39	41	1599
Integration grid $(2N_{r,ref}, \frac{3}{2}N_{\theta,ref})$	31	133	4123	39	62	2418	39	62	2418
Integration grid $(N_{r,ref}, 2N_{\theta})$	15	151	2265	19	83	1577	19	83	1577
Integration grid $(\frac{3}{2}N_{r,ref}, 2N_{\theta,ref})$	23	151	3473	29	83	2407	29	83	2407
Integration grid $(2N_{r,ref}, 2N_{\theta,ref})$	31	151	4681	39	83	3237	39	83	3237

5.4 Direct Method Assessment of BLI Benefit Results

5.4.1 Mechanical Flow Power and Mass Flow

The Langley FHP surveys were used to determine the aerodynamic BLI benefit at 70 mph and 84 mph. Appendix D shows that some surveys were carried out twice, and for these, the mean was used for each quantity. The mechanical flow power coefficient and mass flow non-dimensionalized by $\rho_\infty V_\infty A_{\text{fan}}$ are plotted in Figure 5-6. The dashed bars represent left quantities, and the solid bars represent right quantities. BLI inlet data are in black, BLI exit data are in red, and non-BLI data are in blue. As a reminder, it was assumed that the inflow is uniform (freestream), and the mechanical flow power for the non-BLI inlet was taken as zero.

The mechanical flow power coefficient for the non-BLI exit is higher than for the BLI exit configuration. The left to right difference in mechanical flow power for the non-BLI exit is small (1.6% at 70 mph, and 1.4% at 84 mph). There is a larger difference for the BLI exit case (5.9% at 70 mph and 1.2% at 84 mph) due to the asymmetry of the flow, as explained in Chapter 2. The larger difference at 70 mph compare to 84 mph may be associated with the fact that at 70 mph only one survey was taken for both sides whereas at 84 mph two surveys were taken for the left side and one for the right side (see Appendix D). The mechanical flow power at the BLI inlet is different from left to right by 7.0% at 70 mph and 2.8% at 84 mph. Some of this difference may be explained by the fact that at 70 mph there was only one survey per side whereas at 84 mph there were two surveys for each side (see Appendix D). The left to right difference in non-dimensionalized propulsor mass flow is within 2% for all configurations. The difference between BLI inlet and exit is 4% for the right side at 70 mph, and 2.6% for the right side at 84 mph, and within 2% for the left side at 70 and 84 mph. These results agree with the mass flows obtained from CFD [19] which indicate a BLI mass flow lower by about 2% compared to the non-BLI mass flow.

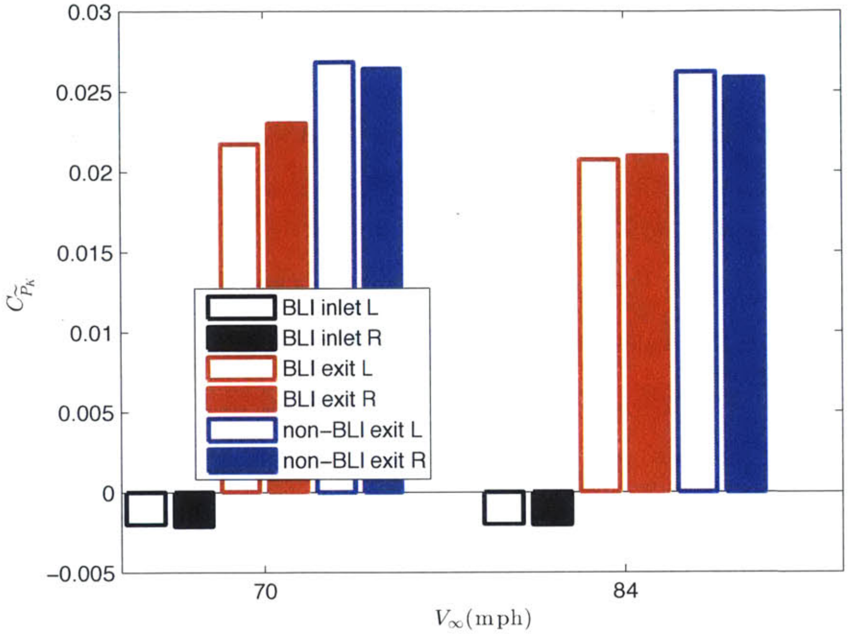

(a) $C_{\widetilde{P}_{\mathrm{K}}}$

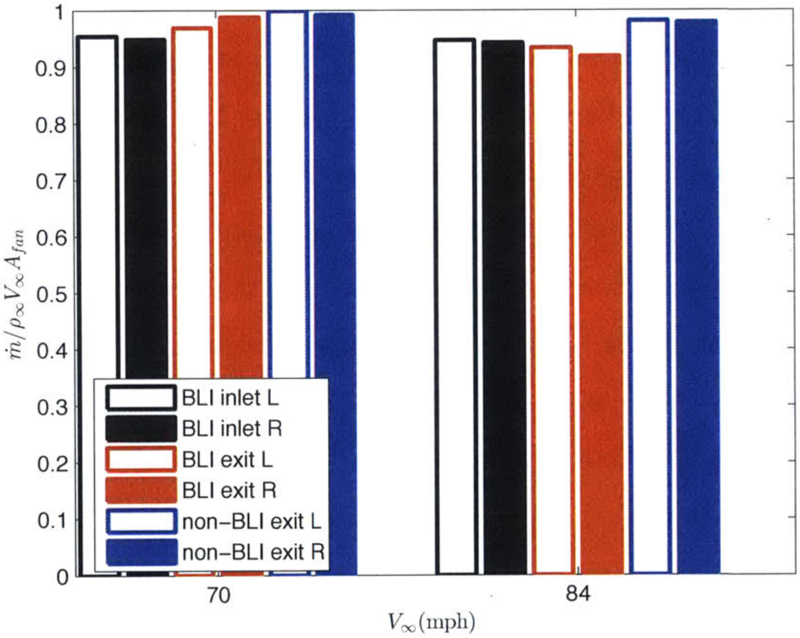

(b) $\dot{m}/\rho_\infty V_\infty A_{\mathrm{fan}}$

Figure 5-6: (a) Mechanical flow power coefficient, and (b) non-dimensionalized mass flow integrated in the survey plane at 70 mph and 84 mph for the BLI inlet, BLI exit, and non-BLI exit. 'L' means left side, and 'R' means right side.

Table 5.2 summarizes the mechanical flow power for each condition with plug 3 at 70 and 84 mph.

5.4.2 BLI Benefit Results

The BLI benefit from comparison of non-BLI and BLI mechanical flow power (Equation 1.2) is 8.1% at 70 mph and 12.2% at 84 mph, without the contribution of the plug flow. It was mentioned in Chapter 3 that the mechanical flow power from the plug is less than 1% of the total mechanical flow power. Integrals of mechanical flow power at the exit planes were computed including the contribution of the plug, and the BLI benefit was found as 8.2% at 70 mph and 12.2% at 84 mph. These changes in benefit are negligible, and the plug mechanical flow power was not taken into account in quoting the results.

5.5 Boundary Layer Ingestion Benefit Uncertainty for the Direct Method

The mechanical flow power was obtained for the direct method via the volume flux of stagnation pressure. The mechanical flow power uncertainty is thus a function of the uncertainty in stagnation pressure difference, $U_{\Delta_{p_0}}$, and the velocity uncertainty, U_V as illustrated in the bottom of Figure 3-15. To find the mechanical flow power at Langley, the FHP as used to compute the mechanical flow power in the GTL was used. For most of the runs, only one run was carried out for FHP survey because

Table 5.2: Mechanical flow power for BLI inlet, BLI exit, and non-BLI exit with plug 3 at 70 and 84 mph. 'L' refers to the quantity for the left side, 'R' refers to the quantity for the right side, and 'Tot' refers to the total quantity including left and right sides.

	BLI inlet			BLI exit			non-BLI exit		
$C_{P_K}(10^{-3})$	L	R	Tot	L	R	Tot	L	R	Tot
70 mph	-2.00	-2.14	-4.15	21.70	23.02	44.72	26.81	26.39	53.19
84 mph	-1.99	-2.04	-4.03	20.71	20.96	41.67	26.19	25.84	52.02

of time limit so the uncertainty is the same as that indicated in [18] for $NGTL$=1. The uncertainty in mechanical flow power coefficient is obtained by combining the uncertainty in C_{P_K} and qV_∞ computed in [18]:

$$\frac{U_{C_{P_\mathrm{K}}}}{C_{P_\mathrm{K}}} = \left[\left(\frac{U_{P_\mathrm{K}}}{P_\mathrm{K}}\right)^2 + \left(\frac{U_{qV_\infty}}{qV_\infty}\right)^2\right]^{1/2}. \tag{5.2}$$

Given the uncertainty in Table 5.3, the mechanical flow power coefficient uncertainty is 2.2%.

There is uncertainty in setting the simulated cruise point, as in Equation (5.3),

$$\frac{U_{C_{P_\mathrm{K}|C_\mathrm{X}=0}}}{C_{P_\mathrm{K}|C_\mathrm{X}=0}} = \left[\left(\frac{U_{C_{P_\mathrm{K}}}}{C_{P_\mathrm{K}}}\right)^2 + \left(\frac{2U_{F_\mathrm{X}}}{qS_\mathrm{ref}C_{P_\mathrm{E}}}\right)^2\right]^{1/2} \tag{5.3}$$

The BLI benefit uncertainty is evaluated by combining the uncertainties for the non-BLI and BLI mechanical flow power coefficients. The uncertainty in BLI benefit for the direct method is 3.3% points at 70 and 3.4% points at 84 mph.

Data repeatability was not assessed here as there are not enough repeat runs.

Table 5.3: Uncertainty for the mechanical flow power coefficient for the indirect method

Variable	Instrument precision (abs)		Instrument precision (%)	
V	1 m/s		2%	
Δ_{pt0}	5 Pa		0.65%	
	70 mph	84 mph	70 mph	84 mph
qV_∞	144 kg/s^3	244 kg/s^3	0.81%	0.80%

5.6 Summary

The mechanical flow power coefficient for the BLI exit is smaller than the non-BLI exit by 17.3% at 70 mph and 22.1% at 84 mph. The aerodynamic BLI benefit is 8.1%±3.3% at 70 mph and 12.2%±3.4% at 84 mph.

Chapter 6

Comparison of BLI Benefit Results

The BLI benefit was experimentally measured in two different ways. It was also calculated from numerical simulations of the powered model. In this chapter, assessment of the pros and cons of each method and comparison of the results are explained.

6.1 BLI Benefit Evaluation by Indirect Measurements

The supporting experiments used to evaluate the BLI benefit with the indirect measurement method necessitated characterizing the fan performance and the response to inlet distortion. One difficulty was matching different experiments (at MIT and at Langley) as the conditions and instrumentations were different. It was not possible to recreate the inlet swirl flow seen in the Langley wind tunnel in the MIT wind tunnel. The overall aerodynamic BLI benefit results are summarized in Table 6.1.

6.2 BLI Benefit Evaluation by Direct Measurements

The advantage of the direct method is that the FHP directly provides stagnation and static pressures, flow angles and thus velocity components. It is then possible to determine changes in the quantities of interest over the survey area, such as inflow and inlet distortion characterizations. An inherent problem of the FHP is the inability of the probe to read pressure near a surface ($< 2D_{FHP}$) or in a strongly non-uniform flow. Another issue is determining the propulsor flowstream: this is easier at the exit than the inlet because the jet and wake are well-defined.

6.3 BLI Benefit Evaluation by CFD

Using CFD it is possible to obtain results for conditions not experimentally accessible. CFD also enables computing BLI benefit for the full-scale aircraft, although it was not done for this project. However, it is difficult to assess the uncertainty in the results. The CFD information in Table 6.1 was provided by Shishir Pandya from NASA Ames.

6.4 Comparison of BLI Benefit

As in Table 6.1 the direct method and indirect method give good agreement as they share a common 95% confidence interval. The CFD underestimates the behavior. As mentioned in Chapter 1, Lieu [11] estimated the aerodynamic BLI benefit from rake surveys during Entry 1 and reported a value of 8.2%±0.8%.

Table 6.1: Aerodynamic BLI benefit for the two experimental methods and CFD

	BLI benefit (%)		Uncertainty (%)	
	70 mph	84 mph	70 mph	84 mph
Direct method	8.1	12.2	±3.3	±3.4
Indirect method	7.9	8.5	±1.5	±1.5
CFD	4.5	-	-	-

Chapter 7

Summary, Conclusions, and Suggestions for Future Work

7.1 Summary and Conclusions

This thesis describes two different experimental methods to evaluate the D8 aerodynamic BLI benefit using a 1:11 scale powered model in the NASA Langley 14x22-foot Subsonic Wind Tunnel. One method, referred to as the indirect method, used the measured electrical power plus supporting experiments to determine the fan and motor efficiencies, needed to convert the electrical power results to mechanical power. For this, the measured BLI benefit was 7.9%±1.5% at 70 mph, and 8.5%±1.5% at 84 mph. The second method, referred to as the direct method, used five-hole probe (FHP) surveys. For this method, the measured BLI benefit was 8.1%±3.3% at 70 mph, and 12.2%±3.4% at 84 mph.

For the indirect method a motor calibration rig was designed and built to assess motor efficiency at the points representing simulated cruise or off-design conditions in the Langley experiments. The fan pressure rise and efficiency at those points were obtained through measurements of the propulsor performance in the MIT GTL wind tunnel. In implementing the direct method, the development of appropriate survey grids, FHP calibration, integration area definition, and numerical integration of the desired fluxes are the necessary steps.

7.2 Suggestions for Future Wind Tunnel Testing

It is emphasized that the experiments are considered as a success and the project objectives have been met. However, several suggestions are given for possible changes in future experiments in the Langley wind tunnel.

- It is possible to evaluate the motor efficiency in real time using a torque meter in the propulsors. This was tried earlier but was found difficult to implement. However, if a suitable instrument can be designed, it might be used for direct torque measurements.

- BLI benefit with the indirect method was evaluated with precision only at the simulated cruise condition (angle of attack of 2°) because the fan characterization was performed using screens to model the inlet distortion at this angle only. Screens or other devices to create the appropriate distortion, including inlet swirl distortion, for more severe conditions could also be designed. For instance, a streamvane [20] could be used.

- Additional FHP surveys could be done for the cruise point with plug 1 and 5 to compute BLI benefit over a range of mass flows.

- Additional FHP surveys could be done to decrease the uncertainty in BLI benefit.

- Additional FHP surveys for the podded inlet to check the uniform inlet assumption.

- Instead of using the FHP calibration in non-uniform flow, the data could be interrogated differently in regions of high shear using the middle port of the FHP for the stagnation pressure, and obtaining the static pressure, and flow angles from interpolating the calibrated data in non-uniform flow.

- CFD simulation with plug 3 would be useful to compare with the experimental results.

Appendix A

MIT Experiments: Mass Flow Comparisons

A.1 Propulsor Characterization Experiments

A.1.1 Introduction

During the process of assessing the TF8000 fan and duct efficiency, three sets of measurements were carried out; (i) Pitot-static (PS) measurements, (ii) five-hole probe (FHP) measurements at the inlet of the propulsor, and (iii) FHP measurements at the exit of the propulsor.

The goal of the PS measurements was to define a calibration factor, k_C, between measured upstream dynamic pressure, q_C, and the dynamic pressure at station 0, q_0. The PS measurements were undertaken without the propulsor at the center of the screen plane (station 0 in Figure 3-1 reproduced in Figure A-1). Figure 3-1 (or A-1) shows the location of the pressure measurement and the stations. The upstream dynamic pressure, q_C, was given by the upstream Kiel probes and wall statics. The PS probe, located in the center of the tunnel, measured the local static and stagnation pressure to gave a dynamic pressure at the center of station 0. Siu [1] obtained the calibration factor, $k_C = \frac{q_0}{q_C} = 3.86 \pm 0.02$.

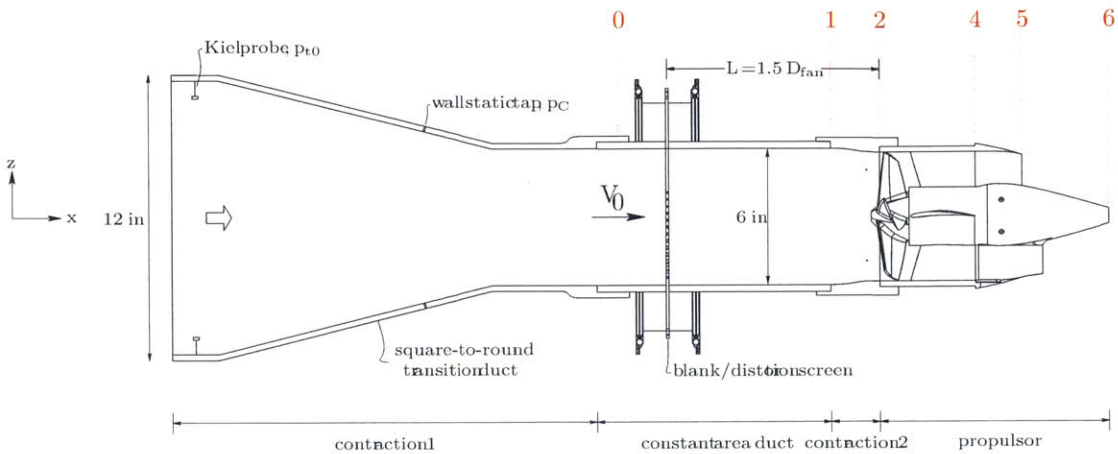

Figure A-1: Setup for the propulsor characterization experiments.
Credit: Siu.

Two sets of measurements were also carried out using a five-hole probe (FHP) to survey the inlet and exit of the propulsor as installed in the MIT GTL 1x1 foot wind tunnel. The discussion here is given in terms of volumetric flow rate, $Q = \frac{\dot{m}}{\rho}$, with the density assumed constant. This assumption about density is discussed in Appendix B. The volumetric flow rate is also convenient for later discussion of power as $P_\mathrm{K} = \frac{\dot{m}}{\rho}\Delta p_\mathrm{t}$. If the changes in density can be neglected and if the small internal plug flow (<1%) is included, the volumetric flow rate should be the same at inlet and exit. The discussion below addresses the experiments without distortion and then the experiments with distortion. The survey grid for the MIT experiments is also described.

A.1.2 Propulsor Characterization Methodology

The volumetric flow rate, Q, can be determined four ways:

- from the measurements at the inlet of the propulsor:
    - The upstream kiel probes and wall statics permanently installed in the contraction after the wind tunnel gave an upstream dynamic pressure which can be converted to the dynamic pressure at station 0 knowing the calibration factor, k_C. These upstream measurements thus imply a reference velocity at the center of station 0 which is denoted as $\widetilde{V}_0 = \sqrt{\frac{2}{\rho} q_\mathrm{C} k_\mathrm{C}}$. As-

    suming the velocity at station 0 is uniform (the wall boundary layer is neglected), an estimation of the volumetric flow rate is $Q_1 = A_{\text{duct}}\tilde{V_0}$. Q_1 is a volumetric flow rate inferred from the upstream dynamic pressure.

  - The volumetric flow rate can also be evaluated from FHP surveys at station 2. The FHP gives the three components of velocity and the stagnation pressure. The assumptions are that the FHP calibration is adequate over the flow region. This is the only actual measurement of volumetric flow rate. The ratio of the measured volumetric flow rate to the inferred volumetric flow rate is needed to know how the measured volumetric flow rate depends on the tunnel operating condition.
  - The volumetric flow rate using the measured velocity at the center of station 2 via the FHP, assuming the flow is uniform, can also be evaluated. This is more a check of the calibration of the FHP, rather than a measurement of flow rate.
- from the measurements at the exit of the propulsor:
  - Volumetric flow rate at the exit of the propulsor was evaluated from FHP measurements at station 5 (Figure 3-1 or A-1) and the pressure measurements inside the plug. The assumptions are that the FHP resolves the flow non-uniformities at the exit station and no mass flow is missed or over-estimated. The jet is defined as region where the stagnation pressure coefficient is positive, $C_{p_0} > 0$, such as in the direct measurement method.

Table A.1 summarizes the different measurements. The various methods of determining volumetric flow rate at the same operating point are compared below.

A.2 Volumetric Flow Rate Results

A.2.1 Comparison of Inlet and Exit Measurements

The measurements at the inlet station are compared in Figure A-2. The y-axis is the ratio of volumetric flow rate to inferred volumetric flow rate, $\frac{Q}{Q_1}$, and the x-axis is

Table A.1: Summary of the volumetric flow rates associated with different instrumentations and different assumptions

Measurement description	Measurement	Instrumentation	Assumption
Inlet measurement 1	$Q_1 = \widetilde{V}_0 A_{\text{duct}}$	upstream kiel probes and wall statics	k_C known and uniform velocity at any station (BL neglected)
Inlet measurement 2	Q-inlet-FHP $= \Sigma V_i A_i$	FHP traverse at station 2	calibration of the FHP
Inlet measurement 3	Q-inlet-FHPcenter $= V_{\text{FHP,center}} A_{\text{FHP}}$	FHP at center of station 2	uniform velocity at any station (BL neglected)
Exit measurement 1	Q-exit-FHP $= \Sigma V_i A_i$	FHP traverse at station 5	calibration of the FHP and non-uniformities resolved by FHP at the exit station, no missed flow

the ratio of inferred velocity to the maximum inferred velocity, $\frac{\widetilde{V}_0}{\widetilde{V}_{0,\max}}$, where $\widetilde{V}_{0,\max}$ is used to non-dimensionalize the wind tunnel speed. The symbols represent the three inlet measurements for different conditions. The curves are a curve fit of the data. The blue line and blue circles correspond to the volumetric flow rate measured using the FHP. The red line corresponds to the volumetric flow rate that was estimated by assuming uniform velocity equal to that measured at the center by the PS probe. The PS volumetric flow rate is used for the non-dimensionalization of the volumetric flow rate. The black squares correspond to the volumetric flow rate obtained from the FHP measurement at the center of the survey and assuming uniform velocity across the inlet plane. Error bars of 1% for the FHP are shown by dashed lines. All measurements lie within the 1% error bars. The FHP overestimates the volumetric flow rate but the difference from the PS estimate is less than 1%.

Inlet and exit measurements can be compared. The latter include data points with no screen and with screens, with left and right propulsors, and at various inflow conditions, and RPMs. Figure A-3 shows the ratio of volumetric flow rate to inferred volumetric flow rate, $\frac{Q}{Q_1}$, as a function of the ratio of inferred velocity to maximum

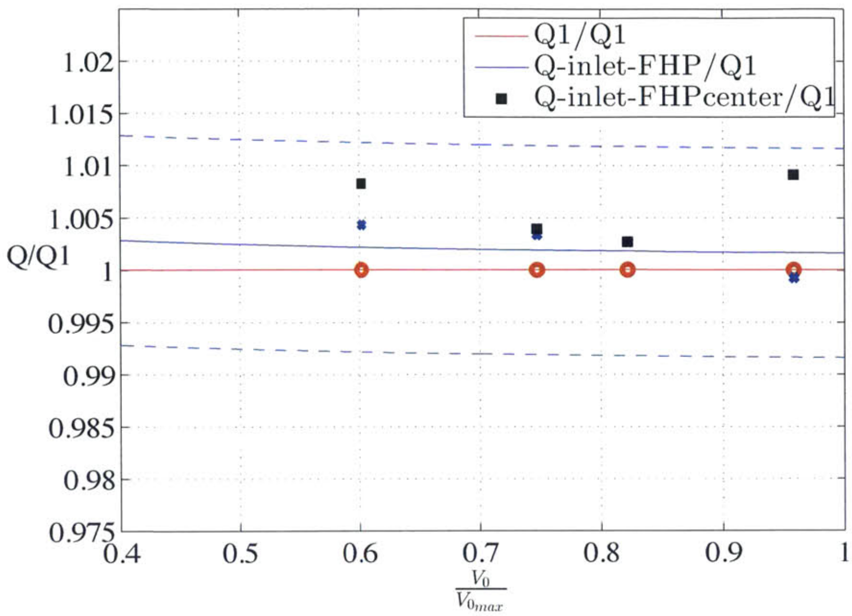

Figure A-2: Non-dimensionalized volumetric flow rate against non-dimensionalized inferred velocity for inlet surveys for the three inlet measurements, no distortion

inferred velocity, $\frac{\widetilde{V_0}}{\widetilde{V_{0,\max}}}$. The red and blue lines are the same as before, volumetric flow rate from PS and FHP respectively from the inlet measurements. The green circles represent the FHP exit data, and the green curve is the average volumetric flow rate from FHP measurements at the exit of the propulsor.

The volumetric flow rate from the FHP includes also the contribution of the plug. The plug volumetric flow rate represents less than 0.6% of the total volumetric flow rate and less than 1% of the mechanical flow power [1]. 1% error bars associated with the exit experiments are also plotted. The blue and green curves represent the inlet and exit FHP measurements, and the exit FHP data differ from the inlet FHP data by a maximum of 2.1%. From continuity, the mass flow determined at the inlet and exit are the same, assuming no leakage (to the best of our knowledge, there were no measurable leaks).

Figure A-4 shows the ratio of volumetric flow rate to inferred volumetric flow rate, $\frac{Q}{Q_1}$, versus the ratio of inferred velocity to the maximum inferred velocity, $\frac{\widetilde{V_0}}{\widetilde{V_{0,\max}}}$, with distortion. The PS volumetric flow rate and the FHP volumetric flow rate at inlet are within 1%. The difference can be seen in Figure A-4(a). The volumetric

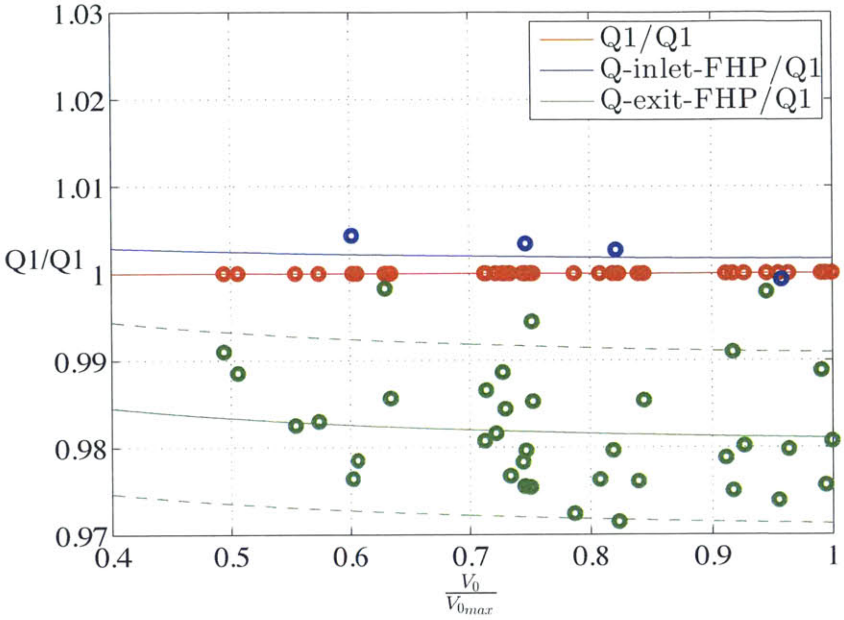

Figure A-3: Non-dimensionalized volumetric flow rate from FHP against non dimensionalized inferred velocity for inlet and exit surveys, no distortion

flow rate evaluated from the FHP center point is not used because the hypothesis of uniform mass flow is not valid with distortion. Inlet and exit measurements are compared in Figure A-4(b). The maximum difference is 2.6%.

For both situations, with or without distortion, the measured volumetric flow rate at the exit is lower than the volumetric flow rate at the inlet.

A.2.2 Survey Grid

The edges of the FHP survey grid area designed by Siu [1] match the bifurcation coordinate, and the assumption is that no mass flow is 'missing' from the measurements. Figure A-5 shows the grid of the exit survey as black dots. The thin black lines separate the area of integration into 37 circumferential areas and match the thick blue lines (on both side of the 270° angle) that represent the bifurcation. The inner magenta circle represents the contour of plug 1 and the outer magenta circle represents the nacelle trailing edge.

A circumferential grid resolution analysis by Siu showed the measured mechanical flow power only varied by 0.1% [1] for the same number of radial points and twice the

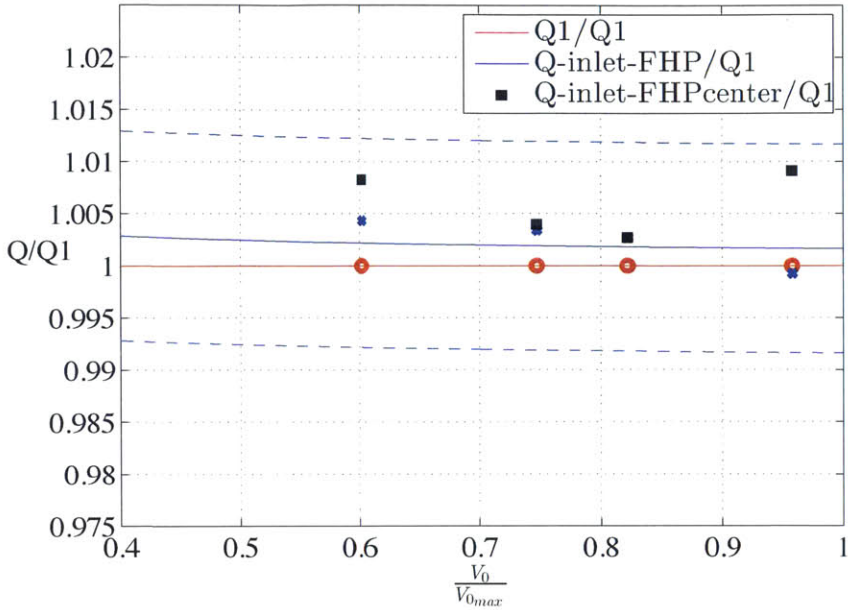

(a) Inlet survey

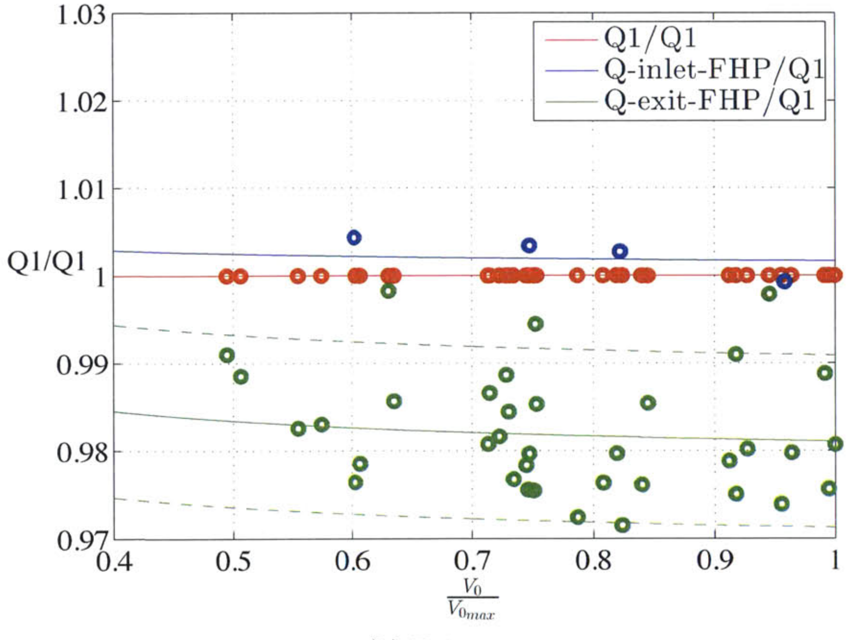

(b) Exit survey

Figure A-4: Non-dimensionalized volumetric flow rate against non-dimensionalized inferred velocity for a) inlet surveys and b) exit surveys with distortion

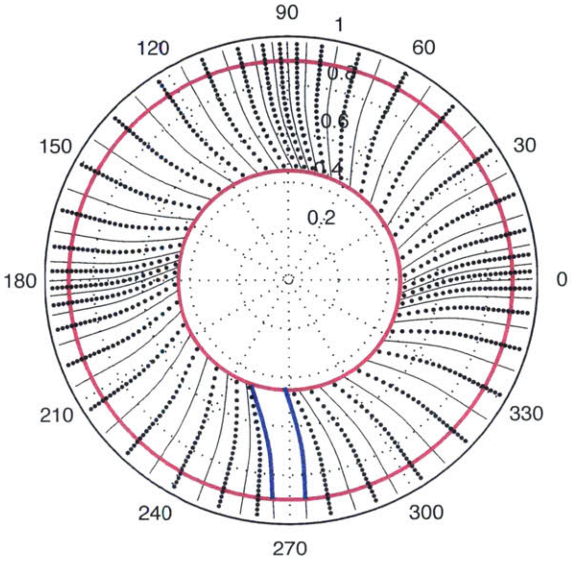

Figure A-5: Exit survey grid in black dots. Black lines represent the separation of the survey in the circumferential direction. Magenta circles represent the plug 1 geometry and the propulsor nacelle. Blue lines represent the geometry of the bifurcation.

number of circumferential points indicating that the mass flow difference from inlet and exit is not because of the grid resolution.

A.3 Summary

The volumetric flow rate measurements indicate a disagreement of mass flow of 2.1% for the case without distortion and 2.6% for the case with distortion between inlet and exit assuming constant density. Appendix B shows that the density changes between inlet and exit are within 0.5% signaling that the primary reason is the assumption that the FHP calibration is adequate everywhere in the surveyed flow. Work is on-going to define root cause for roughly 1.5-2% difference that remains.

Appendix B

MIT Experiments: Inlet to Exit Density Changes

From the stagnation pressure rise coefficient, and the mass-average stagnation pressure at the inlet of the propulsor (measured by the FHP), an estimate of the ratio of stagnation pressure from exit to inlet of the propulsor can be computed as in Equation (B.1). The subscript e means at the exit of the propulsor, and i means at the inlet of the propulsor.

$$\pi = \frac{P_{t,e}}{P_{t,i}} \tag{B.1}$$

From the fan efficiency (Equation (B.2)), and the ideal gas law (Equation (B.3)), the stagnation density ratio can be found. The heat capacity ratio, γ, is 1.4 as literature suggests for compressor turbomachinery analysis.

$$\tau = \frac{T_{t,e}}{T_{t,i}} = 1 + \frac{\pi^{\frac{\gamma-1}{\gamma}} - 1}{\eta_{\mathrm{f}}} \tag{B.2}$$

$$\frac{\rho_{t,e}}{\rho_{t,i}} = \frac{\pi}{\tau} \tag{B.3}$$

A mass-average Mach number can be found from the wind tunnel speed for the inlet surveys and from the mass-average velocity measured by the FHP at the exit surveys:

$$\frac{\rho_\mathrm{e}}{\rho_\mathrm{i}} = \frac{\rho_{t,e}}{\rho_{t,i}} \frac{\left(1 + \frac{\gamma-1}{2} M_\mathrm{i}\right)^{\frac{1}{\gamma-1}}}{\left(1 + \frac{\gamma-1}{2} M_\mathrm{e}\right)^{\frac{1}{\gamma-1}}}. \tag{B.4}$$

For all the tested conditions, the ratio of density is plotted in Figure B-1. The y-axis represents the ratio of density, $\frac{\rho_\mathrm{e}}{\rho_\mathrm{i}}$, and one data corresponds to one run. The red crosses are for the case without distortion introduced, and the blue circles are for the case where distortion is introduced.

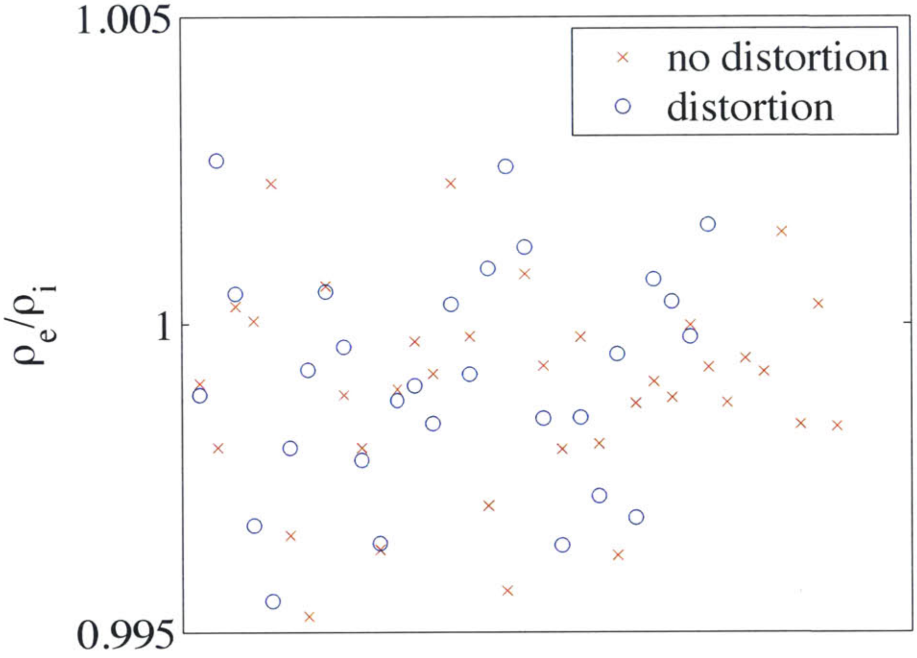

Figure B-1: Ratio of density between exit and inlet of the propulsor with and without distortion introduced for the MIT experiments

It can be seen that the density changes by 0.5% maximum, and the variations in density can be neglected.

Appendix C

Power Sweep Matrix

The operating conditions at which power sweep data were taken are summarized in Table C.1 for Entry 1 and Table C.2 for Entry 2, for BLI (integrated) and non-BLI (podded) configurations. Plug number, wind tunnel speed, and angle of attack are specified. In the boxes, the numbers at each condition specify the run number.

Table C.1: Matrix of power sweep conditions from Entry 1

Entry 1 – Power Sweeps

Last Updated: October 28, 2014

			$\alpha = 2^\circ$	$\alpha = 4^\circ$	$\alpha = 6^\circ$	$\alpha = 8^\circ$
INTEGRATED	PLUG 1	$V_0 = 70$ mph	138 231 247	232	139 233	234
		$V_0 = 56$ mph	141	▨	140	▨
		$V_0 = 42$ mph	142 239	▨	143 240	241
	PLUG 3	$V_0 = 70$ mph	100 108	101	102	103
		$V_0 = 56$ mph	104	▨	107	▨
		$V_0 = 42$ mph	105	▨	106	▨
	PLUG 5	$V_0 = 70$ mph	113 128	114 127	115 126	116 125
		$V_0 = 56$ mph	120	119	118	117
		$V_0 = 42$ mph	121	122	123	124

			$\alpha = 2^\circ$	$\alpha = 4^\circ$	$\alpha = 6^\circ$	$\alpha = 8^\circ$
PODDED	PLUG 1	$V_0 = 70$ mph	041[a] 044[a] 064 264 270 283 284 285 316 318	065 265	067 266 317 319	066 267
		$V_0 = 56$ mph	042[a]	▨	▨	▨
		$V_0 = 42$ mph	043[a] 256	257	258	259
	PLUG 3	$V_0 = 70$ mph	047[a] 051[a] 055 057 083 322 324 326	058 084	048[a] 059 085 323 325 327	052[a] 060 086
		$V_0 = 56$ mph	049[a] 090	089	050[a] 088	087
		$V_0 = 42$ mph	062 091	092	093	061 094
	PLUG 5	$V_0 = 70$ mph	070	071	072	073
		$V_0 = 56$ mph	074	81	080	079
		$V_0 = 42$ mph	075	076	077	078

UNPOWERED	AOA SWEEPS	$V_0 = 70$ mph	032 033 036 334 337 338
		$V_0 = 56$ mph	034 335
		$V_0 = 42$ mph	035 336

[a] bad pressure data

Table C.2: Matrix of power sweep conditions from Entry 2

Entry 2 – Power Sweeps

Note: runs numbered 289 and below were taken without proper temperature compensation on ESPs; pressures may have drifted

Last Updated: October 28, 2014

			$\alpha = 2^\circ$	$\alpha = 4^\circ$	$\alpha = 6^\circ$	$\alpha = 8^\circ$
INTEGRATED	**PLUG 1**	$V_0 = 84$ mph	066 074 076 260 262 266 267 358 361 362	067	068 077	069
		$V_0 = 70$ mph	070 075 078 261 359 360 363	071	072	073
		$V_0 = 56$ mph	079	▨	▨	▨
		$V_0 = 42$ mph	080	▨	▨	▨
	PLUG 3	$V_0 = 84$ mph	037 049 064 098 112 121 235 245 364 365 372	038 099	039 050 100 236 246	040 051 101 237 247
		$V_0 = 70$ mph	041 052 063 102 113 122 238 248 366 373	042 103	043 053 104 239 249	044 054 105 240 250
		$V_0 = 56$ mph	106 114	▨	045 055 061 107 115 241	046 056 062 108 116 242
		$V_0 = 42$ mph	109 117	▨	047 057 059 110 118 243	048 058 060 111 119 244
	PLUG 5	$V_0 = 84$ mph	083 093 095 254 256 263 265 352 355 356 368 371	084	085	086
		$V_0 = 70$ mph	087 094 096 255 264 353 354 357 369 370	088	089	090
		$V_0 = 56$ mph	091	▨	▨	▨
		$V_0 = 42$ mph	092	▨	▨	▨
PODDED	**PLUG 1**	$V_0 = 84$ mph	186 188	▨	▨	▨
		$V_0 = 70$ mph	187 189	▨	▨	▨
	PLUG 3	$V_0 = 84$ mph	131 143 146 147 159 164 182 203 204 221 224 225	132 165	133 148 160	134
		$V_0 = 70$ mph	135 144 145 149 161 166 181	136 167	150 162 168	169
		$V_0 = 56$ mph	137 170	▨	138 171 179	139 172 180
		$V_0 = 42$ mph	140 173	▨	141 174 177 222	142 175 178 223

NEW MOTORS [a]	**INTEGRATED**	**PLUG 1**	$V_0 = 84$ mph	394 398 399
			$V_0 = 70$ mph	395 397 400
		PLUG 3	$V_0 = 84$ mph	384 387 388 401 404
			$V_0 = 70$ mph	385 386 389 402 403

UNPOWERED	**AOA SWEEPS**	$V_0 = 84$ mph	019 020 024
		$V_0 = 70$ mph	018 021 023
		$V_0 = 56$ mph	022

[a] propulsor pressure ports not connected

Appendix D

FHP Flow Survey Matrix

The operating conditions at which five-hole probe (FHP) surveys were conducted during Entry 2 are summarized in Table D.1 for BLI (integrated) and non-BLI (podded) configurations. The number in the left, right, or center column represents the run number. 'Left' means the left propulsor was surveyed, 'right' means the right propulsor was surveyed. The term 'center' applies only for an inlet survey and refers to a survey of the area between the left and right propulsors. The term 'full' applies only for inlet surveys and means that the three surveys (left, center, and right) were performed in a row without modifying the traverser system in between.

Entry 2 – FHP Surveys

Last Updated: October 28, 2014

		CONDITION	PLUG	V_0	α	β	RPM	GRID	LEFT	RIGHT	CENTER	FULL
INTEGRATED	INLET	Cruise	3	70 mph	2°	0°	11 100	fine	272[a, f]	273[a, f]	274[a, f]	
		Cruise	3	84 mph	2°	0°	13 250	fine	268[a] 297[b]	269[a] 298[b]	270[a] 299[b]	
		Cruise	1	84 mph	2°	0°	13 450	fine	290	291	292	
		Cruise	5	84 mph	2°	0°	13 200	fine	294[b]	295[b]	296[b]	
		TOC	3	70 mph	2°	0°	13 500	coarse				308
		Descent	3	70 mph	8°	0°	5 250	medium				280[a]
		Descent	3	70 mph	6°	0°	5 250	coarse				303
		Descent cross-wind	3	70 mph	6°	+15°	5 250	coarse				304
		Descent cross-wind	3	70 mph	6°	-15°	5 450	coarse				305[c]
		SOC	3	42 mph	8°	0°	14 000	medium				283[a]
		SOC cross-wind [g]	3	42 mph	8°	+15°	14 000	coarse				309
		AoA effect	3	70 mph	6°	0°	11 100	coarse				282[a]
		AoA effect	3	70 mph	8°	0°	11 100	coarse				281[a]
	EXIT	Cruise	3	70 mph	2°	0°	11 100	fine	311	312		
		Cruise	3	84 mph	2°	0°	13 250	fine	313 344	343		
		Cruise	1	84 mph	2°	0°	13 450	fine	347	346[h]		
		Cruise	5	84 mph	2°	0°	13 200	fine	348	350[e] 376[i]		
		TOC	3	70 mph	2°	0°	13 500	coarse	314	315		

		CONDITION	PLUG	V_0	α	β	RPM	GRID	LEFT	RIGHT
PODDED	EXIT	Cruise	3	70 mph	2°	0°	11 550	fine	192[a]	197[a]
		Cruise	3	84 mph	2°	0°	13 700	fine	193[a] 200[a]	196[a, d]

[a] ESPs not temperature compensated
[b] noise in RPM and P_E
[c] could not control RPM at 5250
[d] double number of samples (20 instead of 10)
[e] tape left on fuse just upstream of inlets
[f] loose current signal wires from left motor
[g] no survey taken at $\beta = -15^\circ$
[h] bias in θ_1 by one positive step ($+0.45^\circ$)
[i] taken with pitch head driver on
(may cause interference in pressures)

Table D.1: Matrix of FHP survey conditions from Entry 2

References

[1] Siu, N. M., Evaluation of Propulsor Aerodnamic Performance for Powered Aircraft Wind Tunnel Expriments, MS, Massachusetts Institute of Technology, Department of Aeronautics and Astronautics, 2015.

[2] Greitzer, E. M., Bonnefoy, P., De la Rosa Blanco, E., Dorbian, C., Drela, M., Hall, D., Hansman, R., Hileman, J., Liebeck, R., Lord, J., Lovergren, J., Mody, P., Pertuze, J., Sato, S., Spakovszky, Z., Tan, C., Hollman, J., Duda, J., Fitzgerald, N., Houghton, J., Kerrebrock, J., Kiwada, G., Kordonowy, D., Parrish, J., Tylko, J., and Wen, E., "N+3 aircraft concept designs and trade studies, Final Report," NASA CR 2010-216794, 2010.

[3] Shin, J., "NASA AERONAUTICS: Strategic Implementation Plan," Tech. rep., NASA, 2015.

[4] Gentry Jr, G. L., Quinto, P. F., Gatlin, G. M., and Applin, Z. T., "The Langley 14- by 22- Foot Subsonic Wind Tunnel: Description Flow Characteristics, and Guide for Users," Technical Paper 3008, NASA, 1990.

[5] Uranga, A., Drela, M., Greitzer, E. M., Titchener, N. A., Lieu, M. K., Siu, N. M., Huang, A. C., Gatlin, G. M., and Hannon, J. A., "Computational Assessment of the Boundary Layer Ingesting Nacelle Design of the D8 Aircraft," AIAA 2014-0907, AIAA SciTech, 52nd Aerospace Sciences Meeting, 13–17 Jan 2014, National Harbor, MD, 2014.

[6] Drela, M., "Development of the D8 transport configuration," 29th AIAA Applied

Aerodynamics Conference, Honolulu, HI, AIAA Paper 2011-3970, 27-30 June 2011, 2011.

[7] Smith, L., " Wake Ingestion Propulsion Benefit," Journal of Propulsion and Power, Vol. 9, No. 1, January 1993, pp. 74–82.

[8] Sato, S., The Power Balance Method For Aerodynamic Performance Assessment, Ph.D. thesis, Massachusetts Institute of Technology, June 2012.

[9] Drela, M., "Power balance in aerodynamic flows," AIAA Journal, Vol. 47, No. 7, 2009, pp. 1761–1771.

[10] Hall, D. K., Analysis of Civil Aircraft Propulsors with Boundary Layer Ingestion, Ph.D. thesis, Massachusetts Institute of Technology, February 2015.

[11] Lieu, M. K., Quantification of the Boundary Layer Ingestion Benefit for the D8-Series Aircraft Using a Pressure Rake System, MS, Massachusetts Institute of Technology, Department of Aeronautics and Astronautics, 2015.

[12] van Dam, E., Inlet Distortion Characterization of the Boundary Layer Ingestiong D8 Aircraft, MS, Delft University of Technology, Department of Aerodynamics, 2015.

[13] Grasch, A. D., Design of a Model Propulsor for a Boundary Layer Ingesting Aircraft, MS, Massachusetts Institute of Technology, Department of Aeronautics and Astronautics, 2013.

[14] Drela, M., Personal communications.

[15] Coleman, H. W. and Steele, W. G., Experimentation, Validation, and Uncertainty Analysis for Engineers, Wiley, 3rd ed., 2009, pp. 8-12.

[16] Rice, J. A., Mathematial Statistics and Data Analysis, Cengage Learning, 3rd ed., 2007, pp. 184, 195-198.

[17] Shapiro, S. S. and Wilk, M. B., "An Analysis of Variance Test for Normality (Complete Samples)," Biometrika, Vol. 52, 1965, pp. 591–611.

[18] Titchener, N. A., Casses, C. J., Siu, N. M., Huang, A., Hannon, J., and Greitzer, E., "NASA Langley 14x33 Foot Subsonic Wind Tunnel Uncertainty for the D8 Experiments," Internal report.

[19] Pandya, S., Huang, A., Espitia, A., and Uranga, A., "Preliminary Experimental Assessment of the Boundary Layer Ingestion Benefit for the D8 Aircraft," AIAA 2014-0906, AIAA SciTech, 52nd Aerospace Sciences Meeting, 13–17 Jan 2014, National Harbor, MD, 2014.

[20] Kenyon, H., "Distorting airflows on purpose," Aerospace America, March 2015, pp. 10–12.